COMMUNICATIONS IN COMPUTATIONAL PHYSICS
Vol. **2**, No. 3, pp. 367-450

Commun. Comput. Phys.
June 2007

REVIEW ARTICLE

Heterogeneous Multiscale Methods: A Review

Weinan E[1,*], Bjorn Engquist[2], Xiantao Li[3], Weiqing Ren[4] and Eric Vanden-Eijnden[4]

[1]*Department of Mathematics and Program in Applied and Computational Mathematics, Princeton University, Princeton, NJ 08544, USA.*
[2]*Department of Mathematics, The University of Texas at Austin, Austin, TX 78712, USA.*
[3] *Department of Mathematics, Pennsylvania State University, University Park, PA 16802, USA.*
[4] *Department of Mathematics, Courant Institute of Mathematical Sciences, New York University, New York, NY 10012, USA.*

Received 20 August 2006; Accepted 31 August 2006

Available online 5 October 2006

Abstract. This paper gives a systematic introduction to HMM, the heterogeneous multiscale methods, including the fundamental design principles behind the HMM philosophy and the main obstacles that have to be overcome when using HMM for a particular problem. This is illustrated by examples from several application areas, including complex fluids, micro-fluidics, solids, interface problems, stochastic problems, and statistically self-similar problems. Emphasis is given to the technical tools, such as the various constrained molecular dynamics, that have been developed, in order to apply HMM to these problems. Examples of mathematical results on the error analysis of HMM are presented. The review ends with a discussion on some of the problems that have to be solved in order to make HMM a more powerful tool.

AMS subject classifications: 65N30, 74Q05, 74Q20, 39A12

Key words: Multi-scale modeling, heterogeneous multi-scale method, multi-physics models, constrained micro-scale solver, data estimation.

Contents

*Corresponding author. *Email addresses:* weinan@math.princeton.edu (W. E), engquist@math.utexas.edu (B. Engquist), xli@math.psu.edu (X. Li), weiqing@cims.nyu.edu (W. Ren), eve2@cims.nyu.edu (E. Vanden-Eijnden)

1 Introduction

The heterogeneous multiscale method, or HMM, proposed in [56] is a general framework for designing multiscale methods for a wide variety of applications. The name "heterogeneous" was used to emphasize that the models at different scales may be of very different nature, e.g. molecular dynamics at the micro scale and continuum mechanics at the macro scale. Since its inception, there has been substantial progress on multiscale modeling using the philosophy of HMM. The HMM framework has proven to be very useful in guiding the design and analysis of multiscale methods, and in several applications, it helps to transform multiscale modeling from a somewhat ad hoc practice to a systematic technique with a solid foundation. Yet more possibilities are waiting to be explored, particularly in the application areas. Many new questions of physical, numerical or analytical nature have emerged. All these make HMM an extremely fruitful and promising area of research.

The purpose of this article is to give a coherent summary of the status of HMM. It is our hope that this summary will help the reader to understand the design principle behind the HMM philosophy, the main obstacles that one has to overcome when using HMM for a particular problem, and the immediate problems that have to be solved in order to make HMM a more powerful tool.

Just what *is* HMM? After all many multiscale modeling strategies discussed in the applied communities are heterogeneous in nature, i.e. they involve models of different nature at different scales, so what is special about HMM? Through this review we will show that HMM is a general framework for designing multiscale methods that can be applied to a wide variety of applications. In a nutshell, the philosophy is as follows. Assume we are interested in studying the macroscale behavior of a problem for which the macroscale model is only partly known or is valid only on part of the physical domain. In typical situations, we either lack the detailed constitutive relation, or the macroscale model is invalid due to the presence of defects or localized singularities. Assume, on the other hand, that we do have an accurate microscale model at our disposal, but it is too expensive to abandon the macroscale model completely and only use the microscale

model. The HMM philosophy is to start with a carefully selected numerical method for the macroscale model, as if the macroscale model is completely known and valid everywhere, and then focus on the question of how to get the needed data in order to implement the selected macroscale numerical method. In regions where the macroscale model is invalid, or where constitutive relations are missing, we obtain the needed macroscale data by solving the microscale model locally. This is the most important aspect of HMM: *It is a strategy for designing multiscale algorithms that are driven by the data.* Its effectiveness rests upon the fact that it allows us to make maximum use of the knowledge that we have about the particular problem at all scales, macro and micro, as well as the special features that the problem might have, such as scale separation or self-similarity. For instance if the macro and micro time scales are separated, they are automatically decoupled in HMM. In addition, HMM also suggests a unified approach for carrying out error analysis for a large class of multiscale problems.

Despite all that, we will also see from this review that HMM only gives us a starting point, applications of HMM to specific problems can be a highly non-trivial task. Issues of formulation have to be resolved and technical tools have to be developed along the way. The situation is similar to that of finite element methods: On one hand, finite element offers a very attractive framework for designing numerical methods for a wide variety of problems; on the other hand, applying this framework to a specific problem can be quite non-trivial.

1.1 Classical and new multiscale methods

Almost all problems in science and engineering are multiscale in nature. Things are made up of atoms and electrons at the atomic scale, and at the same time are characterized by their natural geometric dimensions which are usually several orders of magnitude larger. In the same way, atomic processes occur at the time scale of femto-seconds (10^{-15} second), but events in our daily lives are happening at a much slower pace. Thus for every specific problem that we encounter, we speak of the macroscopic scale as the particular scale that we are interested in. All smaller scales are referred to as microscopic scales.

For many problems though, this multiscale nature is not that important. Effective models can be obtained with satisfactory accuracy to account for the effects of microscopic processes. In fact most scientific models are of this type. Consider the example of fluid flow. There we are interested in the density and velocity fields of the fluid; the effect of the molecular processes are modeled by the equations of state and the constitutive relations. Most of these effective models are empirical, but there is also a substantial amount of work on analytical derivations of these effective models from microscopic theories [166, 185].

In spite of their tremendous successes, the effective models also have their limitations. One main limitation is accuracy. This is particularly an issue for complex systems, such as complex fluids. When the modeling error is larger than the solution error, the usefulness of the model becomes a concern. A second limitation is the complete neglect

of microscopic mechanisms which are sometimes of interest. Take the example of polymeric fluids. It is often of interest to know the microstructural information such as the conformation of the polymers, not just the macroscopic flow field. The third limitation is associated with the empirical nature of the models – especially for complex systems: These effective models often do not have a solid foundation. For these reasons, one might be tempted to switch completely to a microscopic model that has better accuracy, better physics and better foundation. However this is not an optimal strategy not only because the microscopic models are often too complex to handle, but also because that the data we get are often quite redundant, complicated procedures are required to extract the information of interest. Indeed if we simulate crack propagation in a solid using molecular dynamics, the data we obtain will be overwhelmed by the trajectories of atoms away from the crack tip, which are of very little interest.

This is where multiscale modeling comes in. By coupling macroscopic and microscopic models, we hope to take advantage of both the simplicity and efficiency of the macroscopic models, as well as the accuracy of the microscopic models. Indeed the basic task of multiscale modeling is to design combined macroscopic-microscopic computational methods that are much more efficient than solving the full microscopic model and at the same time gives the information that we need to the desired accuracy.

From the viewpoint of numerical methods, there has already been a long history of using multiscale ideas in methods such as the multi-grid method, fast multipole method and adaptive mesh refinement. Wavelet representation makes explicit use of multiscale decomposition of functions and signals. So what is new in the new breed of multiscale methods, such as the quasi-continuum method and HMM? How are they different from the more traditional multiscale methods such as multi-grid [27,182]?

The difference between traditional multiscale methods such as multi-grid, and the new multiscale methods such as HMM is that traditional multiscale methods are general purpose microscale solvers. Their purpose is to resolve the details of the solutions of the microscale model. The objective of the newly developed multiscale methods is to capture the macroscale behavior of the system with a cost that is much less than the cost of full microscale solvers. Specifically the new multiscale methods are designed to satisfy the requirement

$$\frac{\text{cost of multiscale method}}{\text{cost of microscale solver on the full domain}} \ll 1. \tag{1.1}$$

Of course some compromise has to be made in order to achieve this.

1. We have to ask for less about the solutions of the microscale problem, e.g. we have to be satisfied with getting only the gross behavior of the solutions, and the details on part of the physical domain, not the details everywhere.
2. We must explore possible special features of the microscale problem, such as scale separation, self-similarity, etc. Therefore these methods are less general than traditional microscale solvers.

One main challenge is to recognize such special features in a problem and make use of it. This has been a common theme in current research in multiscale modeling. The disparity

of time scales, for example, has long been a major obstacle in atomistic simulations such as molecular dynamics. But in methods such as HMM, it is used as an asset.

As an example, consider the classical elliptic problem

$$-\nabla\cdot(a(\mathbf{x})\nabla u(\mathbf{x}))=f(\mathbf{x}) \tag{1.2}$$

on a smooth domain Ω with some boundary conditions. We will assume that f as well as the boundary conditions are nice, with no small scales. But for a, let us distinguish three different cases:

- The first is when a is a nice function with no small scale features.
- The second case is when a has multiple scales, but the small scales have some special features such as separation of scales. In this case, we write $a=a^\varepsilon$ where ε signifies the small scale.
- The third case is when a has small scales and the small scales do not have any special features.

The first case is clearly the simplest and the third case the most difficult. But despite that the method for dealing with problems in these two extreme cases are not very different: We just have to use efficient fine scale solvers, such as multi-grid and adaptive mesh refinement methods. Even though in the third case the problems contain multiple scales, it is not very helpful to write $a=a^\varepsilon$ since no values of ε are particularly significant and we just have to think of them as tough problems that require detailed resolution.

Modern multiscale methods are concerned with the second class of problems. In this case, we have the possibility of capturing the large scale features of the solutions, using methods that are much less costly than full fine scale solvers. This is the focus of methods such as HMM.

Table 1: Classical and modern multiscale techniques. Classical multiscale techniques are *general* purpose solvers for the fine scale problem. Recent multiscale modeling focuses on developing *special* purpose technique that aim at further reducing the computational complexity by using special features of the fine scale problem, such as scale separation.

Classical Techniques	Recent Techniques
Multigrid Method [27]	Car - Parrinello Method [30]
Domain Decomposition [143]	Quasi-continuum Method [169]
Wavelet-based Methods [47]	Optimal Prediction [42]
Adaptive Mesh Refinement [9]	Heterogeneous Multiscale Method [56]
Fast Multipole Method [82]	Gap-Tooth Scheme [95]
Conjugate Gradient Method [81]	Adaptive Model Refinement [76]

Of course this division cannot be taken in strict terms. The more recent multiscale techniques can also lead to new ideas for solving the fine scale problems. This will be an important theme for further research: Can these new ideas in multiscale modeling be used to develop techniques that can handle more general problems?

1.2 Classification of multiscale problems

As we have just discussed, the first step in multiscale modeling is to recognize the special features of the problem that one might take advantage of in order to design multiscale methods that satisfy (1.1). For this purpose, it is useful to divide multiscale problems into different categories according to their common features:

Type A: These are problems that contain isolated defects or singularities such as cracks, dislocations, shocks and contact lines. For these problems, the microscopic model is only necessary near defects or singularities. Further away it is adequate to use the macroscopic model. *In this case, the macro-micro coupling is localized.*

Type B: These are problems that require "first-principle-based" constitutive modeling. One example is the homogenization problem for equations of the type (1.2). Under fairly general conditions that amount to scale separation for the coefficient a^ϵ, it can be shown that the effective macroscale model takes the form [18]:

$$-\nabla\cdot(A(\mathbf{x})\nabla U(\mathbf{x}))=f(\mathbf{x}), \tag{1.3}$$

where $A(\mathbf{x})$ is called the homogenized coefficient. Even though the homogenized coefficient can in principle be expressed in terms of the solutions of the underlying microscale model (1.2), they are not explicitly given except for very special problems such as one-dimensional problems. Ad hoc averaging techniques are in general not accurate enough. It is then desirable to use (1.3) but with $A(\mathbf{x})$ obtained directly from the underlying microscale model (1.2). In many cases, this is possible to do with a cost that is much less than solving the full microscale model (1.2) over the entire macroscopic domain.

Type C: These are problems that have features of both type A and type B.

Type D: These are problems that exhibit self-similarity in scales. Examples include critical phenomena in statistical physics, fractals and turbulent transport.

Clearly as research in multiscale modeling continues, more types of problems will be identified. In this paper, we will focus on types A and B problems. We will only discuss type D problems briefly.

1.3 Serial and concurrent coupling

Most current work on multiscale modeling is in the setting of the so-called "concurrent coupling" methods [5], i.e. the microscale and the macroscale models are linked together "on-the-fly" as the computation goes on. More recently, this approach has also been referred to as "solving equations without equations" or "equation-free" [95]. This is in contrast to the "serial coupling" method which determines an effective macroscale model from the microscale model in a pre-processing step and uses the resulted macroscale model in further applications. Serial coupling methods have been largely limited to "parameter passing", and as such it is very widely used in applications, such as constructing empirical atomistic potentials from quantum mechanics simulations, assigning hopping

rates in kinetic Monte Carlo schemes using data from molecular dynamics, computing transport coefficients using microscopic models, etc. But there is no reason why it should be limited to this case. As long as the needed constitutive equation is known to depend on very few variables, serial coupling provides a viable alternative to concurrent coupling techniques. Concurrent coupling methods are preferred when the constitutive relation depends on many variables, and therefore difficult to be extracted by precomputing.

A typical example is in the kinetic Monte Carlo simulation of epitaxial crystal growth. When the set of possible configurations is pre-determined and is small, one typically prefers pre-computing the transition rates using more refined models such as density functional theory, i.e. the coupling is carried out in a serial fashion. However, when consider morphology at a much larger scale and when coupling to continuum model is concerned, the number of independent parameters becomes very large and therefore a concurrent coupling approach is more preferred, as is done [167].

From a numerical viewpoint, the two strategies are very much related. The choice between the two strategies is usually made on the grounds of computational cost. For both serial and concurrent coupling methods, the key issue is to design microscopic simulations that give us the needed macroscopic data. In addition, the results of a concurrent simulation can be used to suggest the functional form for the constitutive relation, which can then be used in a serial coupling method. Therefore the two strategies can be combined to yield optimal efficiency.

The HMM framework can be used both for concurrent and serial coupling methods.

Table 2: Comparison of the frequently used terminologies.

Terminologies adopted here	Other terminologies
Serial coupling [5]	Pre-computing Microscopically-informed modeling Parameter passing Sequential coupling
Concurrent coupling [5]	"On-the-fly" calculation [30] Solving equations without equations "Equation-free" [95] Bridging scales [178]
Compression operator [56]	Projection operator [27] Coarse graining Restriction operator [95]
Reconstruction operator [56, 105] Reinitialization	Prolongation operator [27] Lifting operator [95]
Domain decomposition	Hand-shaking schemes Bridging domains [181] Hybrid schemes

1.4 General strategies

When solving a PDE, the first step is to choose the type of methods that will be used. These methods can be finite difference, finite element, finite volume, spectral or particle methods. For problems with complex geometries, for example, we usually prefer finite element methods. Once the general strategy is chosen, we still need to work on the detailed discretization and the detailed algorithm. Similarly for multiscale modeling, the first step is also to select a general strategy. Existing general strategies include

- Domain decomposition methods. This is particularly popular for type A problems. In this approach, the macro and microscale models are solved on different domains which may or may not overlap, and the two models are matched either over a handshake region or across an interface.
- Adaptive mesh and model refinement. This is also referred to as adaptive algorithm refinement [76], but we think "model refinement" is a better terminology. This is a modification of the adaptive mesh refinement method, except for an added option to switch to a more refined model when it is necessary.
- The heterogeneous multiscale method. This is the focus of the present review and will be discussed in detail later.
- Gap-tooth schemes or patch dynamics. The main idea is to combine results of microscale simulations on small spatial and temporal domains via interpolation and extrapolation to capture the large scale behavior, by exploiting scale separation. This technique is particularly attractive for type B problems. But currently, there are not enough specifics on how the strategy can be used for realistic problems.

Each strategy provides a starting point, and for particular problems they may lead to very similar algorithms. No matter which strategy is used, the heart of the matter is always how the macro and microscale models are coupled together. This issue may exist in different forms: For domain decomposition methods, the issue is how to match the different models in the handshake region or across the interface. For HMM, the issue is how to impose the constraints on the microscale model to ensure consistency with the local macro state, and how to extract the needed macroscale data from the results of the microscale simulation. For gap-tooth schemes, the issue is how to link the different microscale simulations on small boxes in order to mimic microscale simulations over the whole domain. Real progress can only be made after these issues are clearly understood.

2 The HMM framework

2.1 The structure of HMM

We now turn to the framework of HMM. The general setting is as follows. We are given a microscopic system whose state variable is denoted by u, together with a microscale

Figure 1: Schematics of HMM framework.

model, which can be abstractly written as

$$f(u,b)=0, \tag{2.1}$$

where b is the set of auxiliary conditions, such as initial and boundary conditions for the problem. We are not interested in the microscopic details of u, but rather the macroscopic state of the system which we denote by U. It satisfies some abstract macroscopic equation:

$$F(U,D)=0, \tag{2.2}$$

where D stands for the macroscopic data that are necessary in order for the model to be complete.

Denote by Q the compression operator that maps u to U, and R any operator that reconstructs u from U:

$$Qu=U, \qquad RU=u. \tag{2.3}$$

Q and R should satisfy: $QR=I$ where I is the identity operator. Q is called a compression operator instead of a projection operator since it can be more general than projection, e.g. it can be a general coarse-graining operator, as in biomolecular modeling. The terminology of reconstruction operator is adopted from Godunov schemes for nonlinear conservation laws [105] and gas-kinetic schemes [183]. Compression and reconstruction operators are similar to the projection and prolongation operators used in multi-grid methods, or the restriction and lifting operators in [95].

Examples of Q and R were given in [56].

The goal of HMM is to compute U using the abstract form of F and the microscale model. It consists of two main components.

1. Selection of a macroscopic solver. Even though the macroscopic model is not available completely or is invalid on part of the computational domain, one uses whatever knowledge that is available on the form of F to select a suitable macroscale solver.

2. Estimating the missing macroscale data D using the microscale model. This is typically done in two steps:
   (a) Constrained microscale simulation: At each point where some macroscale data is needed, perform a series of constrained microscopic simulations. The microscale solution needs to be constrained so that it is consistent with the local macroscopic state, i.e. $b = b(U)$. In practice, this is often the most important technical step.
   (b) Data processing: Use the microscale data generated from the microscopic simulations to extract the needed macroscale data.

Data estimation can either be performed "on the fly" as in a concurrent coupling method, or in a pre-processing step as in a serial coupling method. The latter is often advantageous if the needed data depends on very few variables.

Before we turn to concrete examples, we should emphasize that HMM is not a specific method, it is a framework for designing methods. For any particular problem, there is usually a considerable amount of work, such as designing the constrained microscopic solvers, that is necessary in order to turn HMM into a specific numerical method.

In the remaining part of this section, we will discuss examples of how HMM can be used for some relatively simple problems.

2.2 Type B examples

2.2.1 ODEs with multiple time scales

We will discuss two simple examples of ODEs with multiple time scales. The first is stiff ODEs with spectrum on the negative real axis, a prototypical example being:

$$\begin{cases} \dot{x} = -\dfrac{1}{\varepsilon}(x - f(y)), \\ \dot{y} = g(x,y). \end{cases} \tag{2.4}$$

The second is ODEs with oscillatory solutions. In this case the spectrum is located close to the imaginary axis. A prototypical example is

$$\begin{cases} \dot{\varphi} = \dfrac{1}{\varepsilon}\omega(I) + f(\varphi,I), \\ \dot{I} = g(\varphi,I), \end{cases} \tag{2.5}$$

in action-angle variables, studied in averaging methods [11]. Here f and g are assumed to be periodic in φ with period 2π and bounded as $\varepsilon \to 0$. In these examples x and φ are the fast variables; y and I are the slow variables, which are also our macroscale variable U.

Analytical and numerical issues for these problems have been studied for a long time. We refer to standard reference books such as [11,86] where limiting equations as $\varepsilon \to 0$ are

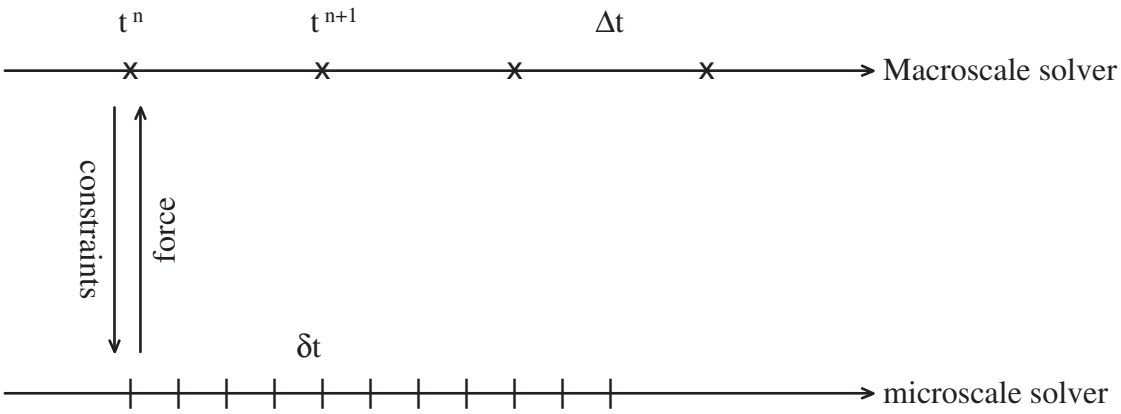

Figure 2: Schematics of HMM for ODEs.

given for both (2.4) and (2.5). For (2.4), the fast variable x is rapidly attracted to the slow manifold where $x=f(y)$ and the effective equation for y is

$$\dot{y}=g(f(y),y)=:G(y). \tag{2.6}$$

For (2.5), the quasi-periodic motion of φ can be averaged out as $\varepsilon\to 0$ and the effective equation for I reads

$$\dot{I}=G(I) \quad \text{where } G(I):=\frac{1}{2\pi}\int_0^{2\pi} g(\varphi,I)d\varphi. \tag{2.7}$$

The idea of HMM is to use the existence of the limiting equations such as (2.6) or (2.7), and some knowledge about their explicit form, to construct numerical schemes for (2.4) or (2.5). These schemes will be useful for more complex situations where the limiting equations are not given explicitly.

Consider (2.4) first. As the macroscale solver, we may select a conventional explicit ODE solver such as a Runge-Kutta scheme or a linear multi-step method. We may also select special purpose solvers such as the symplectic integrators. For illustration, let us assume that we will use forward Euler as the macroscale solver. We can express it as

$$y^{n+1}=y^n+\Delta t\tilde{G}^n(y^n). \tag{2.8}$$

The time step Δt is chosen to resolve the macroscale dynamics of interest, but not the small scales.

The data that need to be estimated from the microscale model are the forces $\tilde{G}^n(y^n)\approx G(y^n)$. To estimate this data, we solve near $t=t^n$ a modified microscale model with the constraint that the slow variables are kept fixed. For the example (2.4), this modified microscale model is simply the equation for x, with y kept fixed, e.g.

$$x^{n,m+1}=x^{n,m}-\frac{\delta t}{\varepsilon}(x^{n,m}-f(y^n)), \quad m=0,1,\cdots,N-1. \tag{2.9}$$

N should be large enough such that $x^{n,m}$ as $m \to N$ has converged to a stationary value with the desired accuracy. We then take

$$\tilde{G}(y^n) = g(x^{n,N}, y^n). \tag{2.10}$$

Notice that N is independent of ε, which indicates that the overall cost of HMM is independent of ε.

The case of (2.5) can be treated similarly. Assuming that we use forward Euler as the macroscale solver, we have

$$I^{n+1} = I^n + \Delta t \tilde{G}^n(I^n), \tag{2.11}$$

where $\tilde{G}^n(I^n) \approx G(I^n)$ must be estimated from the microscale model. For this purpose, we use

$$\varphi^{n,m+1} = \varphi^{n,m} + \frac{\delta t}{\varepsilon}\omega(I^n) + \delta t f(\varphi^{n,m}, I^n).$$

The difference with the previous example is that the estimation of $\tilde{G}^n(I^n)$ must now involve an explicit time-averaging:

$$\tilde{G}^n(I^n) = \frac{1}{N}\sum_{m=1}^{N} K_{m,N} g(\varphi^{n,m}, I^n), \tag{2.12}$$

where the weights $\{K_{m,N}\}$ should satisfy the constraint

$$\frac{1}{N}\sum_{m=1}^{N} K_{m,N} = 1. \tag{2.13}$$

The specific choice of $\{K_{m,N}\}$ will affect the overall accuracy of HMM. (2.12) is called an F-estimator [56]. Extensive analytical and numerical results using this methodology can be found in [69, 160]. In the context of stiff ODEs, HMM can be considered as an improvement of earlier ideas in [71, 77]. HMM has the additional advantage that it also works for a class of oscillatory problems.

The choice of (2.10) can be viewed as a special case of (2.12) when $K_{m,N} = 1$ for $m = N$ and $K_{m,N} = 0$, otherwise. This choice is optimal for dissipative stiff ODEs since the fast variable exhibits a purely relaxational behavior.

The above strategy can be easily extended to more general problems in the form

$$\dot{z} = h(z, \varepsilon), \tag{2.14}$$

provided that one has explicit knowledge of the slow variables in the system, which will be denoted by $y = Y(z)$. Note that $h(z,\varepsilon)$ is in general unbounded as $\varepsilon \to 0$ due to the existence of fast dynamics. Again, let us use the forward Euler as the macro solver for illustration:

$$y^{n+1} = y^n + \Delta t \tilde{F}^n(y^n). \tag{2.15}$$

To estimate the force $\tilde{F}^n(y^n)$, we solve the microscale problem (2.14) with the constraint that $Y(z^{n,m}) = y^n$. As before, we used m as index for the time steps in the micro solver. Using the relation

$$\frac{dy}{dt} = \nabla_z Y(z) \cdot h(z,\varepsilon),$$

we obtain an estimate of the effective force in the limiting equation for y by time averaging:

$$\tilde{F}^n = \frac{1}{N} \sum_{m=0}^{N-1} K_{m,N} \nabla_z Y(z^{n,m}) \cdot h(z^{n,m},\varepsilon), \tag{2.16}$$

where the weights $\{K_{m,N}\}$ must satisfy (2.13).

2.2.2 Elliptic equation with multiscale coefficients

Our last example was in the time domain. We next discuss an example in the spatial domain. Consider the classical elliptic problem

$$\begin{cases} -\operatorname{div}\left(a^\varepsilon(\mathbf{x})\nabla u^\varepsilon(\mathbf{x})\right) = f(\mathbf{x}), & \mathbf{x} \in D \subset \mathbb{R}^d, \\ u^\varepsilon(\mathbf{x}) = 0, & \mathbf{x} \in \partial D. \end{cases} \tag{2.17}$$

Here ε is a small parameter that signifies explicitly the multiscale nature of the coefficient $a^\varepsilon(\mathbf{x})$: It is the ratio between the scale of the coefficient and the scale of the computational domain D. In the next section we will discuss finite element methods for problems of this kind. Here we discuss an approach based on the finite volume method. This is a simplified version of the methods presented in [3]. Similar ideas can also be found in [51].

As the macroscale solver, we choose a finite volume method on a macroscale grid, and we will denote by $\Delta x, \Delta y$ the grid size. The grid points are at the center of the cells, the fluxes are defined at the boundaries of the cells. The macroscale scheme is simply that on each cell, the total fluxes are balanced by the total source or sink terms:

$$-J_{i-\frac{1}{2},j} + J_{i+\frac{1}{2},j} - J_{i,j-\frac{1}{2}} + J_{i,j+\frac{1}{2}} = \int_{K_{i,j}} f(\mathbf{x}) d\mathbf{x}. \tag{2.18}$$

Here $K_{i,j}$ denotes the (i,j)-th cell.

The data that need to be estimated are the fluxes. This is done as follows. At each point where the fluxes are needed, we solve the original microscale model (2.17) on a square domain of size δ, with boundary condition: $u^\varepsilon(\mathbf{x}) - U(\mathbf{x})$ is periodic, where $U(\mathbf{x})$ is a linear function constructed from the macro state at the two neighboring cells, e.g. for computing $J_{i+\frac{1}{2},j}$, we have

$$\begin{aligned} U(x,y) = &\frac{1}{2}(U_{i,j} + U_{i+1,j}) + \frac{U_{i+1,j} - U_{i,j}}{\Delta x}(x - x_{i+\frac{1}{2}}) \\ &+ \frac{1}{2}\frac{U_{i+1,j+1} + U_{i,j+1} - (U_{i+1,j-1} + U_{i,j-1})}{2\Delta y}(y - y_j). \end{aligned} \tag{2.19}$$

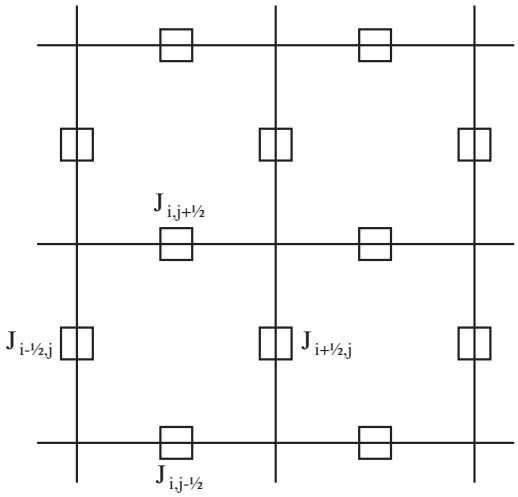

Figure 3: HMM finite volume method.

We then use

$$J_{i+\frac{1}{2},j}=\frac{1}{\delta^2}\int_{I_\delta} j_1^\varepsilon(\mathbf{x})d\mathbf{x},\quad J_{i,j+\frac{1}{2}}=\frac{1}{\delta^2}\int_{I_\delta} j_2^\varepsilon(\mathbf{x})d\mathbf{x}, \tag{2.20}$$

where $\mathbf{j}^\varepsilon(\mathbf{x})=(j_1^\varepsilon(\mathbf{x}),j_2^\varepsilon(\mathbf{x}))=a^\varepsilon(\mathbf{x})\nabla u^\varepsilon(\mathbf{x})$, to compute an approximation to the needed flux.

The periodic boundary condition for the microscale problem is not the only choice. Other boundary conditions might be used. We refer to Section 3 for a discussion in the finite element setting. More thorough discussion is found in [188]. To reduce the influence of the boundary conditions, a weight function can be inserted in (2.20), similar to what is done in the time domain earlier.

To implement this idea, note that the J's are linear functions of $\{U_{i,j}\}$. Therefore to compute the fluxes, we first solve the local problems with U replaced by the nodal basis functions: $\Phi_{k,l}$ is the nodal basis function (vector) associated with the (k,l)-th cell if $\Phi_{k,l}$ is zero everywhere except at the (k,l)-th cell center where it is 1. For each such basis function, there are only a few local problems that need to be solved, since the basis function vanishes on most cells. Since U can be written as a linear combination of these nodal basis functions, the fluxes corresponding to U can also be written as a linear combination of the fluxes correspond to these nodal basis functions. In this way, (2.18) is turned into a system of linear equations for U.

Now how do we choose δ? Clearly the smaller the δ, the less costly the algorithm is. If the original problem (2.17) has scale separation, i.e. the microscale length ε is much smaller than $\mathcal{O}(1)$, then we can choose δ such that $\varepsilon\ll\delta\ll 1$. This results in savings of cost for HMM, compared with solving the original microscale problem on the whole domain D.

2.2.3 Kinetic schemes

Our next example is the derivation of numerical schemes for gas-dynamics that uses only the kinetic model. Such schemes are called kinetic schemes (see for example [49,132,138, 153,183], see also the related work on Lattice Boltzmann methods [32,154]). This example played an important role in developing the HMM framework. However, as will be seen below, our viewpoint is slightly different from that of the original kinetic schemes.

The microscale model in this case is the kinetic equation, such as the Boltzmann equation:

$$\partial_t f + \mathbf{v}\cdot\nabla f = \frac{1}{\varepsilon}C(f). \tag{2.21}$$

Here $f = f(\mathbf{x},\mathbf{v},t)$ is the one-particle phase-space distribution function, which is also our microscale state variable; $C(f)$ is the collision kernel; ε is the mean-free path between collisions in the gas. The macroscale state variables U are the usual hydrodynamic variables of mass, momentum and energy densities, which are related to the microscale state variable f by:

$$\rho = \int f d\mathbf{v}, \quad \rho\mathbf{u} = \int f\mathbf{v}d\mathbf{v}, \quad E = \int f\frac{|\mathbf{v}|^2}{2}d\mathbf{v}. \tag{2.22}$$

(2.22) defines the compression operator Q.

The connection between Euler's equation and the Boltzmann equation is as follows. From the Boltzmann equation, we have:

$$\partial_t \begin{pmatrix} \rho \\ \rho\mathbf{u} \\ E \end{pmatrix} + \nabla\cdot\mathbf{F} = 0, \tag{2.23}$$

where

$$\mathbf{F} = \int_{\mathbb{R}} f \begin{pmatrix} \mathbf{v} \\ \mathbf{v}\otimes\mathbf{v} \\ \frac{1}{2}|\mathbf{v}|^2\mathbf{v} \end{pmatrix} d\mathbf{v}. \tag{2.24}$$

When $\varepsilon \ll 1$, the distribution function f is close to the local equilibrium states, or the local Maxwellians,

$$M(\mathbf{x},\mathbf{v},t) = \frac{\rho(\mathbf{x},t)}{(2\pi\theta(\mathbf{x},t))^{3/2}}\exp\Big(-\frac{(\mathbf{v}-\mathbf{u}(\mathbf{x},t))^2}{2\theta(\mathbf{x},t)}\Big), \tag{2.25}$$

with θ being the absolute temperature.

To design an HMM strategy, we first need to select a macroscale solver. We will focus on the one-dimensional case. Since the macroscale model (2.23) is a set of conservation laws, we will choose as the macroscale solver a finite volume scheme. We first divide the computational domain in the physical space into cells of size Δx. We denote by x_j the center position of the j-th cell, and $x_{j+1/2}$ the boundary between the j-th and $j+1$-th cells. For first-order methods, we represent the solution as piecewise constants, i.e.

$$(\rho,\rho u,E) = (\rho_j,\rho_j u_j,E_j), \quad x \in (x_{j-1/2},x_{j+1/2}].$$

The finite volume scheme takes the form:

$$\begin{cases} \rho_j^{n+1}-\rho_j^n+\dfrac{\Delta t}{\Delta x}\left(F^{(1)}_{j+1/2}-F^{(1)}_{j-1/2}\right)=0, \\ (\rho u)_j^{n+1}-(\rho u)_j^n+\dfrac{\Delta t}{\Delta x}\left(F^{(2)}_{j+1/2}-F^{(2)}_{j-1/2}\right)=0, \\ E_j^{n+1}-E_j^n+\dfrac{\Delta t}{\Delta x}\left(F^{(3)}_{j+1/2}-F^{(3)}_{j-1/2}\right)=0, \end{cases} \tag{2.26}$$

where $\mathbf{F}_{j+1/2}=(F^{(1)}_{j+1/2},F^{(2)}_{j+1/2},F^{(3)}_{j+1/2})^T$ is the numerical flux at the cell boundary $x_{j+1/2}$.

The next step is to compute $\mathbf{F}_{j+1/2}$ by solving locally the kinetic equation. To take into account the wave character of the solutions, we write:

$$\mathbf{F}_{j+1/2}=\mathbf{F}^+_{j+1/2}+\mathbf{F}^-_{j+1/2}, \quad \text{with } \mathbf{F}^{\pm}_{j+1/2}=\int_{\mathbb{R}^{\pm}} f(x^{\mp}_{j+1/2},v,t)\begin{pmatrix} v \\ v^2 \\ \frac{1}{2}v^3 \end{pmatrix} dv. \tag{2.27}$$

Normally one would numerically solve the kinetic model to obtain f. For the present problem, it is much simpler to write down an approximate solution analytically. To leading order, we have:

$$f(x,v,t)\sim M(x-vt,v,t^n). \tag{2.28}$$

Using this in (2.27), we obtain

$$\mathbf{F}^{\pm}=\begin{pmatrix} \rho u A^{\pm}(S)\pm\dfrac{\rho}{2\sqrt{\pi\beta}}B(S) \\ (p+\rho u^2)A^{\pm}(S)\pm\dfrac{\rho u}{2\sqrt{\pi\beta}}B(S) \\ (pu+\rho ue)A^{\pm}(S)\pm\dfrac{1}{2\sqrt{\pi\beta}}(\dfrac{p}{2}+E)B(S) \end{pmatrix}, \tag{2.29}$$

where

$$S=\frac{u}{\sqrt{2\theta}}, \quad p=\rho\theta, \quad A^{\pm}=\frac{1+\mathrm{erf}(S)}{2}, \quad B(S)=e^{-S^2},$$

and $\beta=1/2\theta$. This is the simplest kinetic scheme [49]. The schematic is shown in Fig. 4.

This example illustrates the point that numerically solving the microscale model is not the only way to obtain the needed data. Analytical solution is another possibility. In some cases, one may obtain the needed data through statistical analysis of experimental or other data.

How do we construct higher-order kinetic schemes? The standard practice is to consider both higher-order reconstructions (for the initial value of f in the shaded-region in Fig. 4) and solve the kinetic model to higher-order accuracy. This is the path followed, for example, in [133,183] for constructing second-order kinetic schemes. From the viewpoint of HMM, however, one would simply take a higher-order macroscale solver, such as the ones in [122]. Then it is no longer necessary to use higher-order reconstructions for the initial values of the kinetic model.

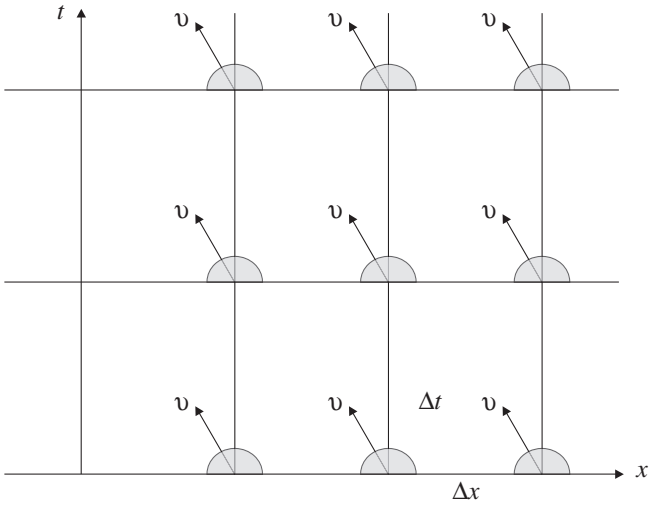

Figure 4: Schematics for the derivation of kinetic scheme: A finite volume method is imposed in the $x-t$ domain, and the kinetic equation is solved (e.g. analytically) over the shaded region to give the fluxes needed in the finite volume method. The v axis indicates the extra velocity variable in the kinetic model, which represents the microstructure for the present problem.

2.2.4 Large scale molecular dynamics (MD) simulation of gas dynamics

In this example we discuss how HMM can be used to carry out macroscale gas-dynamics calculations using only MD. The macroscopic equations are the usual conservation laws of density, momentum and energy. In one dimension, it can be expressed in a generic form:

$$\partial_t \mathbf{u} + \partial_x \mathbf{f} = 0. \tag{2.30}$$

Here $\mathbf{f}$ is the flux. Traditional gas dynamics models assume that $\mathbf{f}$ is a known function of $\mathbf{u}$. Here we do not make that assumption. Instead we will extract $\mathbf{f}$ from an underlying atomistic model, namely, molecular dynamics (MD).

As the macroscale solver, we select a finite volume method. One example is the central scheme of [122] on a staggered grid:

$$\mathbf{u}_{j+1/2}^{n+1} = \frac{\mathbf{u}_j^n + \mathbf{u}_{j+1}^n}{2} - \frac{\Delta t}{\Delta x}\left(\mathbf{f}_{j+1}^n - \mathbf{f}_j^n\right). \tag{2.31}$$

The data that need to be estimated from MD are again the fluxes. This is done by performing a constrained MD simulation locally at the cell boundaries, which are the cell centers for the previous time step. The constraints are that the average density, momentum and energy of the MD system should agree with the local macro state at the current time step n. This is realized by initializing the MD with such constraints and apply the

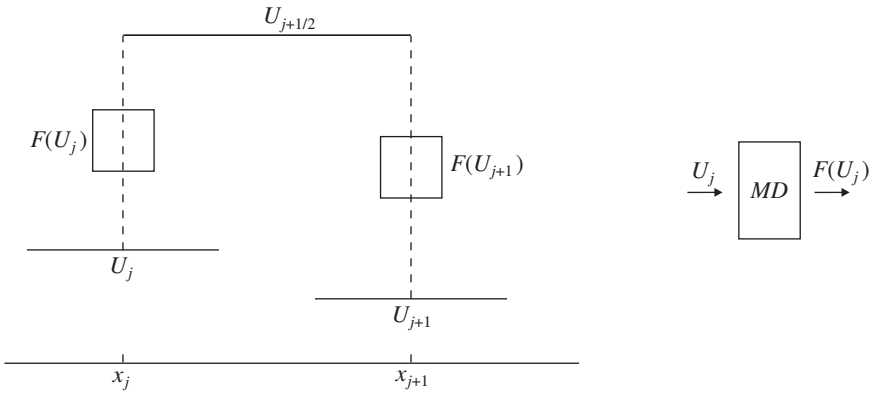

Figure 5: Central scheme: starting with piecewise constant solution, one computes fluxes at x_j and x_{j+1}, and integrates the conservation laws to the next time step, where the grid points are shifted to the midpoints $x_{j+1/2}$. The numerical fluxes are evaluated with the help of MD.

periodic boundary condition afterwards. Using the Irving-Kirkwood formula (see Section 4) which relates the fluxes to the MD data, we can then extract the macroscale fluxes by time averaging the MD data. Ensemble averaging may also be used. We refer to [108] for more details.

One result from such a method is shown in Fig. 6. Here the set-up for the macroscale model is a Riemann problem for one-dimensional wave propagation in solids. The microscale model is two-dimensional MD with Lennard-Jone potential. The result of HMM is compared with that of a direct MD simulation.

2.3 A type A example: Coupled kinetic-hydrodynamic simulation of shock propagation

Our next example is continuum gas dynamics locally corrected near shocks by the kinetic model. This is a type A problem. Problems of this type have been studied for a long time in the kinetic theory community using domain decomposition methods (see for example [22, 104]). The framework of HMM suggests a way of handling this problem that is slightly different from what is done in the literature.

The macroscopic process is gas dynamics, the microscopic process is described by a kinetic model. Therefore, as the macroscale solver, it is natural to choose the kinetic schemes for gas dynamics. Away from shocks, the numerical fluxes are computed using (2.29). At the shocks the numerical fluxes are computed by solving locally the kinetic model using micro time steps. The kinetic model is constrained by the local macroscopic state through the boundary conditions. As shown in Fig. 7, the kinetic equation is solved in the shaded region between x_l and x_r (assume that the shock is at the cell boundary $x_{k+1/2}$). Boundary condition is needed at x_l for $v>0$. For this we choose

$$f(x_l,v,t)=M(x_l,v,t), \quad v>0, \tag{2.32}$$

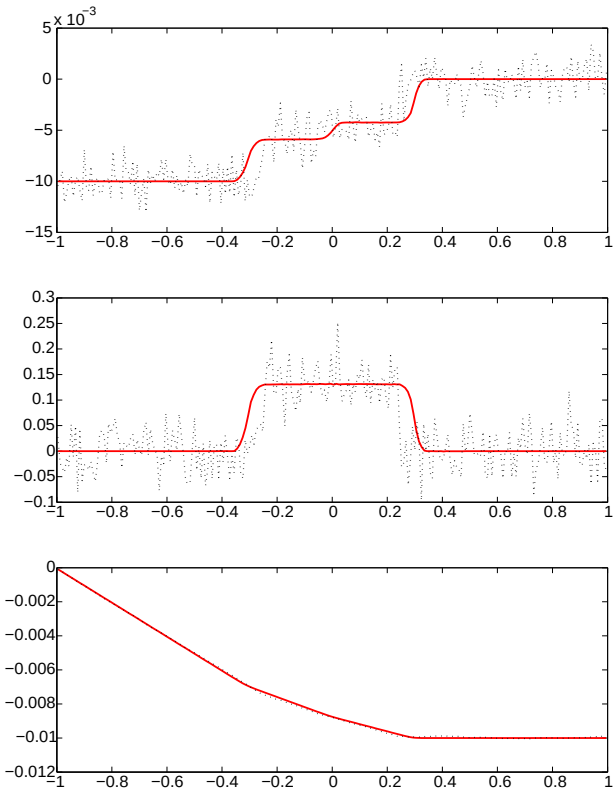

Figure 6: Numerical test on shock formation and propagation in solids. 200 macro-grid points are used and each local MD simulation consists of 40×10 atoms and 10^4 steps of time integration. The solution is displayed after 40 steps of integration over macro time steps. Solid line: computed solution; dashed line: full atom simulation (one realization). Top: strain; middle: velocity; bottom: displacement.

where the right-hand side is the local Maxwellian corresponding to the macroscopic state at x_l, obtained by extrapolating the macro states in the cells to the left of x_l. Boundary condition at x_r can be handled similarly. At $x_{k+1/2}$, we define

$$\mathbf{F}_{k+1/2}=\frac{1}{\tau}\int_{t^n}^{t^n+\tau}dt\Big\{\int_{\mathbb{R}^+}f(x^-_{k+1/2},v,t)\begin{pmatrix}v\\v^2\\\frac{1}{2}v^3\end{pmatrix}dv+\int_{\mathbb{R}^-}f(x^+_{k+1/2},v,t)\begin{pmatrix}v\\v^2\\\frac{1}{2}v^3\end{pmatrix}dv\Big\}, \quad (2.33)$$

for suitably chosen τ.

How do we choose τ? To address this question, we should note that there are potentially two different cases of interest concerning corrections to gas-dynamics models of shocks. The first is when non-equilibrium effects are important. In this case the relaxation time of the gas inside the shock may become comparable to the hydrodynamic time, and we should simply choose $\tau=\Delta t$. Note that in this case there is no time scale separation, and the kinetic model is solved continuously throughout the shock region, with occasional re-initialization as the shock region moves. This is shown schematically in the left

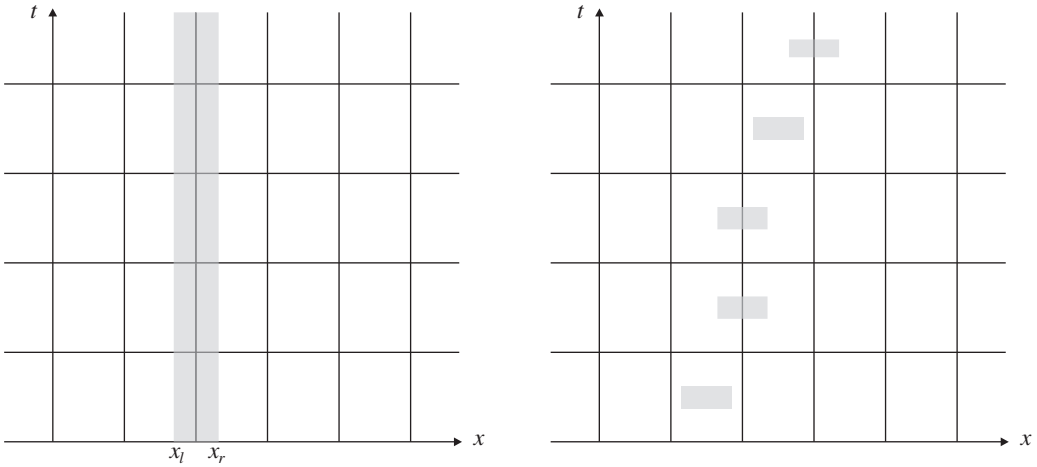

Figure 7: Schematics for the coupled kinetic-gas dynamics simulation: A finite volume method is imposed everywhere in the $x-t$ domain. The numerical fluxes are computed using the kinetic scheme away from the shocks, and directly from the solutions of the kinetic equations at the shocks. The shaded regions indicate where the kinetic equation needs to be solved. The left panel illustrates the case when there is no scale separation between the relaxation time scale inside the shock and the hydrodynamic time scale. The right panel shows the case when there is time scale separation.

panel in Fig. 7. The second is when viscous or other higher order gradient effects are important inside the shocks, but there is still scale separation between the relaxation time of the gas and the hydrodynamic time. In this case we should choose τ to be larger than the relaxation time of the gas, but still smaller than Δt. The specific choice should be made adaptively by observing the numerical fluxes in (2.33) and select its stationary value (as a function of τ). At each macro time step, the kinetic model needs to be re-initialized, as discussed earlier for gas-kinetic schemes. A schematic is shown in the right panel in Fig. 7.

The final component of the method is a criterion for locating the shock position. At the present time, there is little systematic work in this direction.

2.3.1 Comparison with domain decomposition methods

With few exceptions, most existing approaches to type A problems are based on the idea of domain decomposition [5, 6, 22, 23, 73, 84, 85, 91, 104, 123, 125, 130, 139]. The microscale model is solved near the defects or singularities. The macroscale model is solved elsewhere. The two domains may or may not overlap. The results from the two different models are matched to ensure compatibility of the two models. Different possibilities have been exploited according to whether one matches the macroscopic fields or the fluxes.

In contrast, in the HMM approach the macroscale solver is imposed over the whole domain. Near defects or singularities (here the shocks), the data (here the flux) required by the macroscale solver is estimated from a microscale model. Therefore the HMM

methodology is closer to that of **(adaptive) model refinement** [76, 126]: Near defects or singularities, a more refined model is used to supply the data.

For the example discussed above, the model is adaptively refined at the shocks and is replaced by the kinetic model for flux evaluation. The overall algorithm is still that of a finite volume method. The kinetic model is used inside the finite volume scheme to provide part of the data. In addition, HMM provides ways of further limiting the size of the computational domain for the microscopic model, by exploiting time scale separation so that the kinetic equation does not have to be solved for all time, or spatial scale separation so that the kinetic equation is solved only in a very thin strip inside the macro cells. This philosophy is opposite to that of over-lapping – it might be called "under-lapping". See Fig. 7.

2.4 The fiber bundle viewpoint

It is worth pointing out that when extracting the needed data from microscopic models, one can think of the microscale model as been solved on a "virtual domain": It is not necessary to think of this domain as being part of the physical domain we are interested in. The conceptual framework of HMM is very similar to that of fiber bundles: The physical domain is the base manifold, the local microstructures are defined over the fibers. The mapping from the fibers to the base manifold via the compression operator is a local operation. This is a key conceptual difference between HMM and domain decomposition or the adaptive model refinement methods. The latter two approaches make explicit use of the fact that both the macro and micro models are defined on the same domain.

The algorithmic consequence of this concept is that under the framework of HMM, the microscale computations carried out over different macroscopic locations communicate with each other only through the macroscale solver. By thinking of the microstructure as been defined in a virtual space, we are naturally led to numerical algorithms which are free of the limitations associated with filling up the macroscopic space and time by the microscale grid points and time steps, and this is the reason why HMM enables us to design numerical algorithms that are much more efficient than the brute force microscale solvers.

Since HMM relies on a local connection between the microstructures and the macro state, one might suspect that it is not as effective for problems with long range interactions. At the present time, this issue remains to be addressed.

2.5 Recovering information about the microscale process

HMM is designed to capture the macroscale behavior of the underlying system. However, in many cases, particularly for type A problems, we are also interested in some aspects of the microscopic behavior. Possibilities exist within the HMM framework to recover such information. The microscale solutions obtained in the data extraction process do provide samples for the local microstructure.

In this connection, two questions remain to be answered. The first is the accuracy of such microscale information. The second is the sense in which we speak about accuracy. This is a general question in multiscale, multi-physics modeling. In many cases, we can only expect to capture some statistical or qualitative aspects of the microscopic process. At the present time, this problem has not been formulated in precise terms. We will come back to such issues later on when we discuss other applications.

3 The heterogeneous multiscale finite element method

Consider

$$-\nabla\cdot(k^\varepsilon(\mathbf{x})\nabla u^\varepsilon(\mathbf{x}))=f(\mathbf{x}),\qquad \mathbf{x}\in\Omega\subset\mathbb{R}^d. \tag{3.1}$$

Here ε is a small parameter that signifies explicitly the multi-scale nature of the coefficient $k^\varepsilon(\mathbf{x})$, which will be referred to as the conductivity tensor. Problems of this type have been extensively studied in the context of heat or electric conduction in composite materials, mechanical deformation of composites, etc [18]. In particular, the homogenization technique was initially developed for analyzing these problems [12, 13, 18]. However, except for the case when the microstructure is locally periodic, it is difficult to make use of the homogenized equations for numerical purpose. In addition, the homogenized equation lacks information about the micro-scale behavior which is important for analyzing stress distribution in composites, for example.

3.1 The macro-scale solver and the needed data

We will take a finite element approach. For (3.1), the macro-scale solver can be chosen simply as the standard C^0 piecewise linear finite element method over a macroscopic triangulation $\mathcal{T}_H$ of mesh size H. We will denote by X_H the macroscopic finite element space which could be the standard piecewise linear finite elements over T_H.

The data that need to be estimated from the microscale model is the stiffness matrix on $\mathcal{T}_H$: $A=(A_{ij})$, where

$$A_{ij}=\int_\Omega \nabla\Phi_i(\mathbf{x})K_H(\mathbf{x})\nabla\Phi_j(\mathbf{x})d\mathbf{x}. \tag{3.2}$$

Here $K_H(\mathbf{x})$ is the effective conductivity tensor at scale H and $\{\Phi_i(\mathbf{x})\}$ are the basis functions for X_H. Had we known $K_H(\mathbf{x})$, we could have evaluated A_{ij} simply by numerical quadrature: Let $f_{ij}(\mathbf{x})=\nabla\Phi_i(\mathbf{x})K_H(\mathbf{x})\nabla\Phi_j(\mathbf{x})$, then

$$A_{ij}=\int_\Omega f_{ij}(\mathbf{x})d\mathbf{x}\simeq\sum_{T\in\mathcal{T}_H}|T|\sum_{\mathbf{x}_k\in T}\omega_k f_{ij}(\mathbf{x}_k), \tag{3.3}$$

where $\{\mathbf{x}_k\}$ and $\{\omega_k\}$ are the quadrature points and weights respectively, $|T|$ is the volume of the element $|T|$.

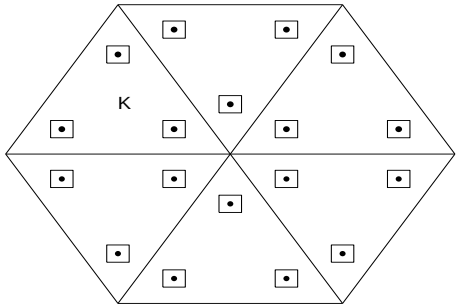

Figure 8: Illustration of HMM for solving (3.1). The dots are the quadrature points in (3.3). The little squares are the microcell $I_\delta(\mathbf{x}_k)$.

In the absence of explicit knowledge of $K_H(\mathbf{x})$, our problem reduces to the approximation of the values of $\{K_H(\mathbf{x}_k)\}$. This will be done by solving the original microscale model locally around each quadrature point $\{\mathbf{x}_k\}$ (See Fig. 8).

Let $I_\delta(\mathbf{x}_k) \ni \mathbf{x}_k$ be a cube of size δ. Consider

$$-\nabla\cdot\left(k^\varepsilon(\mathbf{x})\nabla\phi^\varepsilon\right)=0, \qquad \mathbf{x}\in I_\delta(\mathbf{x}_k). \tag{3.4}$$

The main objective is to probe efficiently the microscale behavior under the constraint that the average (e.g. macroscale) gradient of the solution ϕ^ε is fixed to be a given constant vector. Having solutions to this local problem, we can define the effective conductivity tensor at $\mathbf{x}_k$ by the relation

$$\langle k^\varepsilon(\mathbf{x})\nabla\phi^\varepsilon\rangle_{I_\delta}=K_H(\mathbf{x}_k)\langle\nabla\phi^\varepsilon\rangle_{I_\delta}, \tag{3.5}$$

where $\langle v\rangle_{I_\delta}=(1/|I_\delta|)\int_{I_\delta}v(\mathbf{x})d\mathbf{x}$. The basis of this procedure is the homogenization theorem which has been proved in various contexts; the most general result is found in [129]. The homogenization theorems allow us to define the effective (or homogenized) conductivity tensor, by considering the infinite volume limit of the solutions of the microscale problem subject to the constraint that the average gradient remains fixed. The effective tensor is defined by an average relation of the type (3.5) in the infinite volume limit, i.e.

$$L=\frac{\delta}{\varepsilon}\to\infty.$$

In the special case when the microstructure is periodic, the infinite volume problem reduces to a periodic problem and therefore can be considered on its period.

In practice, one solves (3.4) with the constraint $\langle\nabla\phi^\varepsilon\rangle_{I_\delta}=\mathbf{e}_1,\cdots,\mathbf{e}_d$ respectively, where d is the spatial dimension of the problem. Denote these solutions by ϕ_j^ε, $j=1,\cdots,d$. Then

$$(\langle k^\varepsilon(\mathbf{x})\nabla\phi_1^\varepsilon\rangle_{I_\delta},\cdots,\langle k^\varepsilon(\mathbf{x})\nabla\phi_d^\varepsilon\rangle_{I_\delta})=K_H(\mathbf{x}_k). \tag{3.6}$$

In summary, the overall algorithm consists of the following steps:

- Solve for $\phi_1^\varepsilon,\cdots,\phi_d^\varepsilon$ using the boundary conditions discussed below, at each $\mathbf{x}_k$.
- Obtain the approximate values of $K_H(\mathbf{x}_k)$ by averaging the microscale solutions using (3.6).
- Assemble the effective stiffness matrix using (3.3).
- Solve the macroscale finite element equation using the effective stiffness matrix. If we express the macroscale solution in X_H in the form of $U_H(\mathbf{x})=\sum U_j\Phi_j(\mathbf{x})$, then the macroscale finite element equation takes the standard form:

$$AU=F, \tag{3.7}$$

where $U=(U_1,\cdots,U_N)^T, F=(F_1,\cdots,F_N)^T$, and $F_j=(f(\mathbf{x}),\Phi_j(\mathbf{x}))$.

The numerical solution U_H obtained through this procedure contains information about the average behavior of u^ε itself, but not its gradient. There is potentially an additional important step, which is to obtain information about the gradient of the solution, either through some post-processing techniques or by analyzing the solutions of the microscale problems ϕ^ε. However, the details of this last step remains poorly understood. We will come back to this point later.

3.2 The constrained micro-scale solver

The local microscale problem is constrained by the local macroscopic state through the constraint

$$\langle\nabla\phi^\varepsilon\rangle_{I_\delta}=G \tag{3.8}$$

for some fixed constant vector G. [188] considered three different types of boundary conditions for the local problem.

1. Dirichlet Formulation.

$$\phi^\varepsilon(\mathbf{x})=G\cdot\mathbf{x}, \quad \text{on } \partial I_\delta. \tag{3.9}$$

2. Periodic Formulation.

$$\phi^\varepsilon(\mathbf{x})-G\cdot\mathbf{x} \text{ is periodic with period } I_\delta. \tag{3.10}$$

3. Neumann Formulation.

$$k^\varepsilon(\mathbf{x})\nabla\phi^\varepsilon(\mathbf{x})\cdot\mathbf{n}=\lambda\cdot\mathbf{n}, \quad \text{on } \partial I_\delta, \tag{3.11}$$

where the constant vector $\lambda\in\mathbb{R}^d$ is the Lagrange multiplier for the constraint that

$$\langle\nabla\phi^\varepsilon\rangle=G. \tag{3.12}$$

For example when $d=2$, to solve problem (3.11) with the constraint (3.12), we first solve for u_1 and u_2 from

$$\begin{cases} -\nabla\cdot(k^\varepsilon(\mathbf{x})\nabla u_i)=0, & \text{in } I_\delta,\\ k^\varepsilon(\mathbf{x})\nabla u_i(\mathbf{x})\cdot\mathbf{n}=\mu_i\cdot\mathbf{n}, & \text{on } \partial I_\delta, \end{cases} \tag{3.13}$$

for $i=1,2$, where $\mu_1=(1,0)^T$, $\mu_2=(0,1)^T$. Then given an arbitrary G, the Lagrange multiplier $\lambda=(\lambda_1,\lambda_2)^T$ is determined by the linear equations

$$\lambda_1\langle\nabla u_1\rangle+\lambda_2\langle\nabla u_2\rangle=G \tag{3.14}$$

and the solution of (3.11)-(3.12) is given by $\phi^\varepsilon=\lambda_1 u_1+\lambda_2 u_2$.

One can check easily that $\langle\nabla\phi^\varepsilon(\mathbf{x})\rangle=G$ holds for all three formulations.

The performance of these formulations was carefully studied in [188]. The main conclusions were:

1. Periodic boundary condition performs better than the other two formulations.
2. The variance of the estimated effective tensor behaves as $\sigma^2\sim L^{-d}$ for the random checker-board problem, and $\sigma^2\sim L^{-2}$ for the periodic problem.
3. In general Neumann formulation underestimates the effective tensor and Dirichlet formulation overestimates the effective tensor. In both cases, the effective conductivity tensors converge to the infinite volume limit with first order accuracy $\mathcal{O}(1/L)$, where L is the cell size.

This method is extended in [186] to study the elastic deformation of functionally graded materials.

HMM in this case resembles the idea of representative volume averaging that is commonly used in subsurface flow modeling, with I_δ playing the role of the representative volume. In representative volume averaging, the microstructural information is usually discarded after the effective conductivities are extracted out. This is unsatisfactory since the microstructural information is particularly important in this case – it contains information about stress distribution in composite materials or velocity fields in porous media. The HMM philosophy puts more emphasis on the interaction between the macro and microscale behavior. For example, the solutions of the microscale problem (3.5) do contain useful information about the gradients of the solution u^ε. However, at the present time, very little systematic work has been done on how such information can be extracted, except for the simple case when the microstructure is periodic.

3.3 Other multiscale finite element methods

An alternative proposal for constructing multiscale finite element methods is to modify the basis functions in the finite element space by solving, for each element, the original microscale problem with vanishing right-hand side and suitable boundary conditions [13–16, 88, 112]. The modified basis functions are used to constructive the effective stiffness matrix on the coarse grid. This idea was first introduced by Babuška et al. [14] in the context *generalized finite element methods* for solving elliptic equations with general rough coefficients. For problems with multiscale coefficients, Hou et al. [88] introduced overlapping in order to alleviate the difficulties with local boundary conditions. Some

rudimentary versions of this idea was also suggested in [112] for solving Helmholtz equations by using oscillatory functions as basis functions.

Once the basis functions and the effective stiffness matrix is computed, the modified basis function method works efficiently as a coarse grid method. The main problem, however, is in the overhead for computing the basis functions. This overhead is already comparable with solving the original microscopic problem, if a linear scaling method such as multi-grid is used. As all other upscaling methods, the goal of both HMM-FEM and the modified basis function method is to obtain the effective stiffness matrix at the macroscale. The difference lies in how this goal is achieved. HMM-FEM approximates the stiffness matrix *directly* by performing local simulations of the original microscale model. The size of the local simulation can be chosen according to the special features of the problem. In particular, one may choose the domains of the local problems such that they overlap with each other and their union covers the whole computational domain. This would make HMM-FEM very close to the modified basis function methods, and most likely also defeat the purpose of HMM-FEM. The modified basis function method obtains the effective stiffness matrix by going through an intermediate step, namely modifying the basis functions and as a result, the original finite element space. This limits its flexibility in exploring the multiscale features of the underlying problem. Indeed, with the modified basis function method, solving a problem *with* structure is as hard as solving a problem *without* structure. On the other hand, these techniques might be of some use if the problem (2.17) is solved repeatedly with different right hand side, in which case they can be used as pre-processing techniques, in the same way as LU decomposition, computation of Schur complements [68], and sub-structuring methods [24].

For a more detailed discussion of these methods and their relative performance, we refer to [119]. It was found, among other things, that the accuracies of HMM-FEM and the modified basis function method are generally comparable, despite the difference in cost.

For the special case when the microstructure of a^ϵ is locally periodic, several other methods have been proposed. Some are based on solving the homogenized equations, plus next order terms [44]. One interesting idea, proposed by Schwab et al. [157, 158], uses multiscale test functions. In this case, the finite element space has a tensor product structure, which can be exploited to compensate for the increased dimensionality caused by using the multiscale test functions.

4 Complex fluids and microfluidics

The behavior of liquids is usually very well described by the classical Navier-Stokes equations with the no-slip boundary condition. There are two notable exceptions. The first is non-Newtonian fluids such as polymeric fluids. In this case the constitutive equations are more complex than that of Newtonian fluids, for which the viscous stress is simply a linear function of the rate of strain. The second is micro-fluidics. In this case the

geometry of the flow domain is so small that the no-slip boundary condition is no longer accurate enough.

Three different levels of models are commonly used in the modeling of liquids: molecular dynamics, Brownian dynamics, and hydrodynamics. We will discuss the case when the microscale model is molecular dynamics and the macroscale model is hydrodynamics. But some of the issues that we will discuss are also relevant if the microscale model is Brownian dynamics. For simplicity we will assume that the flow is incompressible. Extending the methodology to compressible flows is quite straightforward. This section is taken mostly from [146].

4.1 The macroscale and microscale models

At the continuum level, the dynamics of incompressible flow has to obey conservation laws of mass and momentum:

$$\begin{cases} \rho\partial_t \mathbf{u} = \nabla\cdot\tau, \\ \nabla\cdot\mathbf{u} = 0, \end{cases} \tag{4.1}$$

where the momentum flux $-\tau = \rho\mathbf{u}\otimes\mathbf{u} - \tau_d$. Here ρ is the density of the fluid which is assumed to be a constant, $\mathbf{u}=(u,v)$ is the velocity field, and τ_d is the stress tensor. We will limit ourselves to the situation when the flow is macroscopically two-dimensional (microscopically it is of course three-dimensional). But extension to macroscopically three-dimensional flows is straightforward. At this stage the system is not closed since the stress tensor is yet to be specified. Traditionally the idea has been to close this system by an empirically postulated constitutive relation, such as

$$\tau_d = -pI + \mu(\nabla\mathbf{u} + \nabla\mathbf{u}^T) \tag{4.2}$$

for simple fluids. In this case, all information about the molecular structure is lumped into one number, the viscosity μ. Here we are interested in the situation when empirical constitutive relations are no longer accurate enough, and more information at the microscopic level is needed.

Another important component in the model is the boundary condition. Almost all macroscopic models assume the no-slip boundary condition

$$\mathbf{u} = \mathbf{u}_0, \tag{4.3}$$

where $\mathbf{u}_0$ is the velocity of the boundary. This is adequate in many situations, but becomes questionable for some problems in micro-fluidics.

For the microscopic model, we will use molecular dynamics (MD). Using standard notations for liquids, we have

$$\begin{cases} m_i\dot{\mathbf{x}}_i(t) = \mathbf{p}_i(t), \\ \dot{\mathbf{p}}_i(t) = \mathbf{F}_i, \end{cases} \tag{4.4}$$

$i=1,2,\cdots,N$. Here m_i is the mass of the i-th particle, $\mathbf{x}_i$ and $\mathbf{p}_i$ are its position and momentum respectively, $\mathbf{F}_i$ is the force acting on the i-th particle. To examine the behavior of the

fluid flow near a solid boundary, we should also model the vibration of the atoms in the solid next to the fluid-solid interface. Therefore one should consider the fluid-solid system as a whole. We will work in the isothermal setting, and the Nosé-Hoover thermostat can be used to control the temperature of the system [75].

The connection between the atomistic and the continuum models is made as follows. Given the microscopic state of the system $\{\mathbf{x}_i(t),\mathbf{p}_i(t)\}_{i=1,2,\cdots,N}$, we define the empirical momentum distribution

$$\mathbf{m}(\mathbf{x},t)=\sum_i \mathbf{p}_i(t)\delta(\mathbf{x}_i(t)-\mathbf{x}), \tag{4.5}$$

where δ is the Delta function. Momentum conservation can then be expressed in terms of the microscopic variables as:

$$\partial_t \mathbf{m}=\nabla\cdot\tau(\mathbf{x},t), \tag{4.6}$$

where the momentum current density $\tau(\mathbf{x},t)$ is given by the following Irving-Kirkwood formula [90]:

$$\begin{aligned}\tau(\mathbf{x},t)=&-\sum_i \frac{1}{m_i}(\mathbf{p}_i(t)\otimes\mathbf{p}_i(t))\delta(\mathbf{x}_i(t)-\mathbf{x})\\ &-\frac{1}{2}\sum_{j\neq i}\big((\mathbf{x}_i(t)-\mathbf{x}_j(t))\otimes\mathbf{F}_{ij}(t)\big)\int_0^1 \delta(\lambda\mathbf{x}_i(t)+(1-\lambda)\mathbf{x}_j(t)-\mathbf{x})\,d\lambda,\end{aligned} \tag{4.7}$$

where $\mathbf{F}_{ij}(t)$ is the force acting on the i-th particle by the j-th particle.

An important issue in molecular dynamics is how to model the atomistic forces accurately. The algorithms that we will discuss are quite insensitive to the details of the atomistic potential. For simplicity we will work with the simplest situation when the interaction between particles is pair-wise and the pair potential is the Lennard-Jones (LJ) potential in a slightly modified form:

$$V^{LJ}(r)=4\varepsilon\left(\left(\frac{\sigma}{r}\right)^{12}-\eta\left(\frac{\sigma}{r}\right)^{6}\right). \tag{4.8}$$

Here r is the distance between the particles, ε and σ are characteristic energy and length scales respectively. The parameter η controls the nature of the interaction between particles. When $\eta=1$, (4.8) defines the usual LJ potential which is attractive at long distance. Repulsion between particles of different species can be modeled using negative values of η.

It proves convenient to use the reduced atomic units. The unit of length is σ. The unit of time is $\sigma\sqrt{m/\varepsilon}$. For temperature it is ε/k_B where k_B is the Boltzmann constant, and for density it is m/σ^3. The unit of viscosity is $(\varepsilon m)^{1/2}/\sigma^2$. The unit of surface tension is ε/σ^2.

4.2 Type B problems: Atomistic-based constitutive modeling

4.2.1 Macroscale solver

As the macroscopic solver, we choose the projection method on a staggered grid [39,40]. The projection method is a fractional step method. At each time step, we first discretize

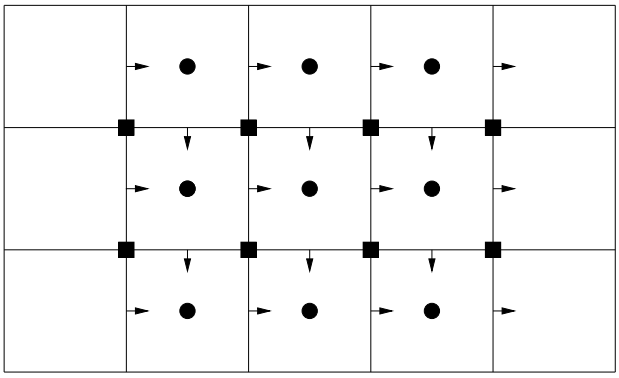

Figure 9: Schematic of the spatial discretization of the continuum equations in (4.1). u is defined at $(x_i,y_{j+\frac{1}{2}})$, v is defined at $(x_{i+\frac{1}{2}},y_j)$, and p is at the cell center $(x_{i+\frac{1}{2}},y_{j+\frac{1}{2}})$. τ_{11} and τ_{22} are calculated at the cell center indicated by circles, and τ_{12} is calculated at the grid points indicated by squares.

the time derivative in the momentum equation by the forward Euler scheme to obtain an intermediate velocity field:

$$\rho\frac{\tilde{\mathbf{u}}^{n+1}-\mathbf{u}^n}{\Delta t}=\nabla\cdot\tau^n, \tag{4.9}$$

where τ^n is the momentum flux. For the moment, pressure as well as the incompressibility condition are neglected. Next the velocity field $\tilde{\mathbf{u}}^{n+1}$ is projected onto the divergence-free subspace:

$$\rho\frac{\mathbf{u}^{n+1}-\tilde{\mathbf{u}}^{n+1}}{\Delta t}+\nabla p^{n+1}=0, \tag{4.10}$$

where p^{n+1} is determined by

$$\Delta p^{n+1}=\frac{\rho}{\Delta t}\nabla\cdot\tilde{\mathbf{u}}^{n+1}, \tag{4.11}$$

usually with Neumann boundary condition.

The spatial discretization is shown in Fig. 9. For integer values of i and j, we define u at $(x_i,y_{j+1/2})$, v at $(x_{i+1/2},y_j)$, and p at the cell center $(x_{i+1/2},y_{j+1/2})$. The diagonals of the flux τ are defined at $(x_{i+1/2},y_{j+1/2})$, and the off-diagonals are defined at (x_i,y_j). The operators ∇ and Δ are discretized by standard central difference and the five-point formula respectively. The use of this grid simplifies the coupling with molecular dynamics.

4.2.2 Estimating the stress

The data that need to be estimated from molecular dynamics are the stresses. Here we will make a constitutive assumption, namely that the stress depends only on the rate of strain. We do not need to know anything about the specific functional form of this dependence.

The key component in estimating the stress is to construct a constant rate-of-strain ensemble for the MD. This is done through a modified periodic boundary condition.

4.2.3 Constrained microscopic solver: Constant rate-of-strain MD

There exists an earlier work due to Lees and Edwards [103] in which the periodic boundary condition is modified to maintain a constant shear in one direction. This is done by shifting the periodic copies of the simulation box above and below in opposite directions according to the given shear profile. This idea was extended to situations with general linear velocity profiles in [146].

Without loss of generality, we will consider the situation when the macroscopic velocity profile is of the form

$$\begin{pmatrix} u \\ v \\ w \end{pmatrix} = \begin{pmatrix} a & b & 0 \\ c & -a & 0 \\ 0 & 0 & 0 \end{pmatrix} \begin{pmatrix} x \\ y \\ z \end{pmatrix} = A\mathbf{x}. \tag{4.12}$$

To initialize the MD calculation, one may simply start with a perfect lattice configuration in a rectangular box. Each particle is given a mean velocity according to (4.12), plus a random component with mean 0 and variance k_BT, where T is the desired temperature and k_B is the Boltzmann constant.

Deforming the simulation box. Periodic boundary condition is imposed on a dynamically deforming simulation box, whose vertices move according to

$$\dot{\mathbf{x}} = A\mathbf{x}, \quad A = \begin{pmatrix} a & b & 0 \\ c & -a & 0 \\ 0 & 0 & 0 \end{pmatrix}. \tag{4.13}$$

Intuitively it is helpful to think of the simulation box as been embedded in the whole space.

The shape of the deformed box at a later time is shown in Fig. 10(b). Suppose at this point a particle crosses the boundary at $P(\mathbf{x})$, with velocity $\mathbf{u}$, it will return to the box at $P'(\mathbf{x}')$ with a modified velocity

$$\mathbf{u}' = \mathbf{u} + A(\mathbf{x}' - \mathbf{x}), \tag{4.14}$$

where P' is the periodic image of P with respect to the deformed box.

It is easy to see that if the velocity field is a pure shear

$$A = \begin{pmatrix} 0 & b & 0 \\ 0 & 0 & 0 \\ 0 & 0 & 0 \end{pmatrix}, \tag{4.15}$$

then this boundary condition becomes simply the Lees-Edwards boundary condition.

Re-initialization. As the simulation proceeds, the simulation box will in general become quite elongated in one direction and narrowed in the other direction (see Fig. 10(c)). If

the box is significantly deformed, we need to re-initialize the configuration. An approximate re-initialization procedure is discussed in [146]. A more accurate re-initialization procedure that makes use of reproducing lattice is discussed in [147].

The MD simulation keeps track of the positions and velocities of all particles as functions of time, from which the instantaneous momentum flux tensor can be calculated using the Irving-Kirkwood formula (4.7).

In practice, (4.7) is averaged over the simulation box. This gives

$$-\tau(t)=\frac{1}{|\Omega|}\sum_{\mathbf{x}_i\in\Omega(t)}\frac{1}{m_i}(\mathbf{p}_i\otimes\mathbf{p}_i)+\frac{1}{2|\Omega|}\sum_{j\neq i}d_{ij}(\mathbf{x}_i-\mathbf{x}_j)\otimes\mathbf{F}_{ij}, \tag{4.16}$$

where in the first term the summation runs over particles inside the box, and in the second term the summation is over all pairs of particles including their images. Here d_{ij} is defined as

$$d_{ij}=\begin{cases}1, & \text{if } \mathbf{x}_i,\mathbf{x}_j\in\Omega,\\ 0, & \text{if } \mathbf{x}_i,\mathbf{x}_j\notin\Omega,\\ c, & \text{if only one of } \mathbf{x}_i,\mathbf{x}_j \text{ is in } \Omega,\end{cases} \tag{4.17}$$

where $0\leq c\leq 1$ is the fraction of $|\mathbf{x}_i-\mathbf{x}_j|$ being cut by the box. Therefore besides contributions from the particles inside the box, particles outside the box also contribute to the stress, as illustrated in Fig. 11.

Eq. (4.16) gives the instantaneous stress at the microscopic time t (see Fig. 12). To extract the macroscopic stress, (4.16) is averaged over time to give an estimate for the macroscale stress:

$$\tau=\frac{1}{T-T_0}\int_{T_0}^{T}\tau(t)dt, \tag{4.18}$$

where T_0 is some relaxation time.

In Fig. 12, we show two numerical examples of the calculated stress. In atomic units the density is $\rho=0.79$ and the temperature is fixed at 1.0 in the first example but not in the second which is not coupled to any thermostats. The stress diverges in this case due to viscous heating.

As a simple validation of this procedure, we show in Fig. 13 the computed shear stress as a function of shear rate for LJ fluids. These data fit quite well to a linear function indicating a linear relation between stress and the rate of strain. The viscosity can be computed by estimating the slope. This gives a value of 2 which agrees well with results in the literature [171].

To summarize, at each macro time step k, the overall algorithm looks as follows:

Step 1 Calculate the needed stresses by constrained local MD simulations;

Step 2 Using the projection method and the computed stresses to get $\mathbf{u}^{k+1}$.

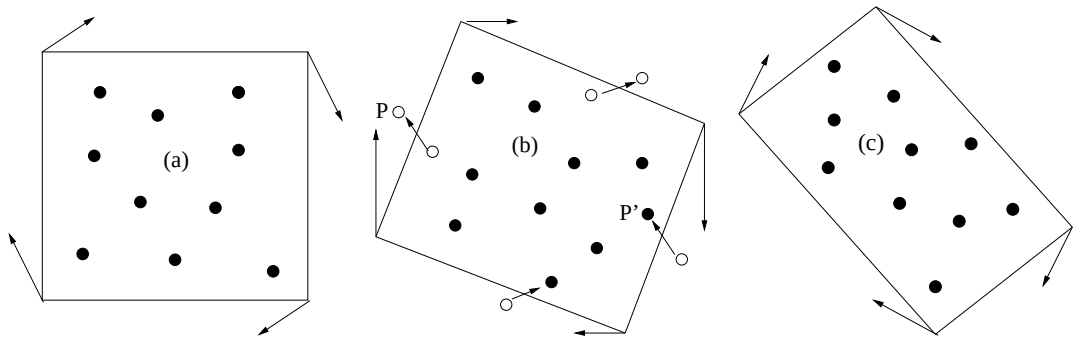

Figure 10: Periodic boundary conditions on a dynamically deforming box.

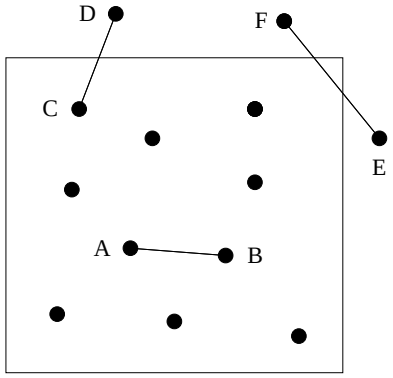

Figure 11: Computing averaged stress: Besides the contributions from the particles inside the box to the averaged stress, the particles outside the box also contribute, such as CD and EF.

4.2.4 Fluid dynamics of chain molecules

This algorithm was validated on a simple example of pressure-driven cavity flow, and applied to a number of other examples, including the driven cavity flow, and a system of dumbbell fluids with FENE potential. Here we briefly report the results for the dynamics of chain molecules that represent flexible polymers. More details are found in [144].

In [144] a bead-spring model of chain molecules is used to represent the flexible polymers, with a total of N beads for each chain. The interaction potential between the beads has two parts. The first is the LJ potential which acts on all beads in the system. The second is the spring force given by the FENE potential:

$$V^{FENE}(r)=\begin{cases} -\frac{1}{2}kr_0^2\ln\left(1-\left(\frac{r}{r_0}\right)^2\right), & r<r_0, \\ \infty, & r\geq r_0. \end{cases} \tag{4.19}$$

The values $k=1$ and $r_0=2.5$ were used. The density of the beads is 0.79. $N=12$. The slip boundary condition suggested in [137] was used. [144] also reports results from com-

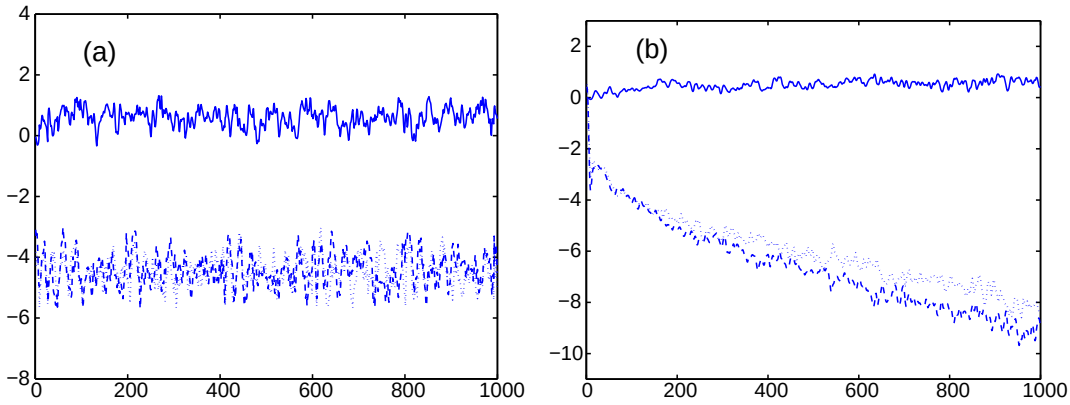

Figure 12: Instantaneous stress as a function of the microscopic time. Solid line: $-\tau_{12}$; dashed line: $-\tau_{11}$; dotted line : $-\tau_{22}$. The temperature is fixed in (a) but not in (b), where the stress diverges due to viscous heating. In both case, $u=0.18y$, $v=0$.

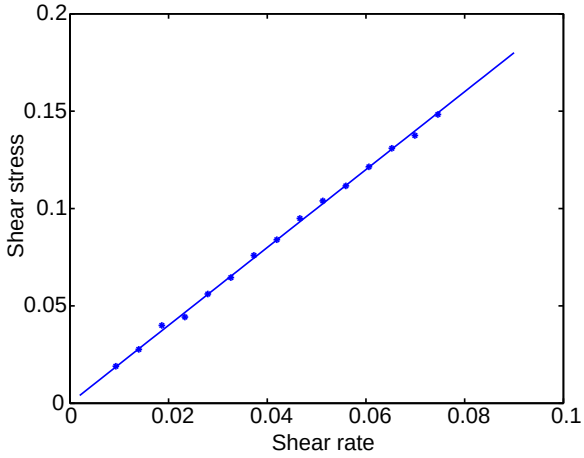

Figure 13: Shear stress as a function of shear rate for simple LJ fluids. The discrete points are obtained from 3d MD simulation, and they fit very well to a linear function with slope 2 which is the viscosity. All the quantities are expressed in the atomic unit.

putations that treat this as a type C problem and extract boundary conditions using the algorithm described next for type A problems. The results are basically the same.

At small driving force, there is only partial slip between the fluid the solid. The velocity profile converges to steady state, as shown in Fig. 14. This steady state profile is compared with the standard Poiseuille profile at the zero-shear-rate viscosity. Besides the partial slip, we also see that the profile for the chain molecules has larger curvature, a characteristic of shear thinning fluids. This is confirmed by the plot of the effective constitutive relation used in the HMM simulation at the steady state.

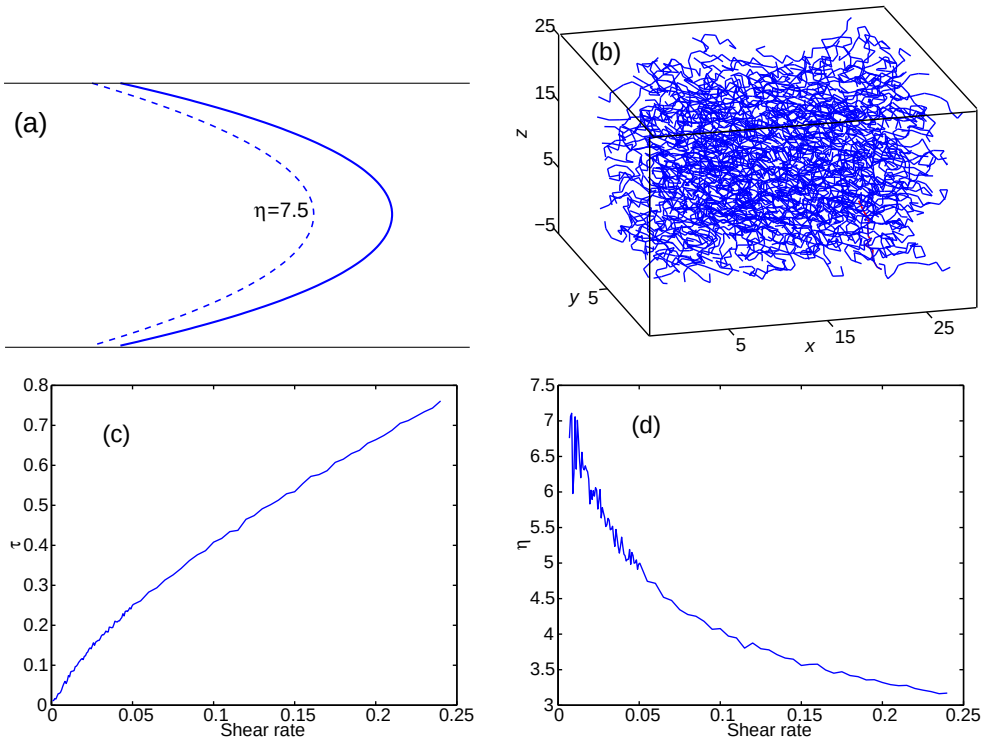

Figure 14: (a): Steady state velocity profile for the polymer fluid made up of chain molecules (solid line), compared with that of the Newtonian fluid (dashed line). We observe partial slip, as well as shear-thinning. (b): A partial sample of the conformation of the chain molecules in a typical MD simulation. (c): Shear stress as a function of shear rate. (d): Viscosity as a function of shear rate. In (c) and (d), to make the results more transparent, we supplemented the results from the HMM calculation by results from pre-computing: The more noisy results at small shear rates are from HMM calculation, the smoother results at higher shear rates are obtained via pre-computing.

4.3 Type A problems: Modeling boundary conditions

In the discussions above we were concerned with the constitutive relations for complex fluids. Here we will discuss boundary conditions for micro-fluidics. One most important aspect of micro-fluidics is the significance of line and surface tension. Therefore as our primary examples, we choose the Marangoni flow and the contact line problem. For these problems, the need for coupling with MD comes from the complex fluid-solid and fluid-fluid interaction near the wall.

4.3.1 Marangoni flows

We will discuss a specific example of the Marangoni flow, namely channel flow driven by complex solid-fluid interactions which are modeled by molecular dynamics.

The HMM procedure goes as follows. The macroscopic solver is the same as before, i.e. a finite-volume projection method on a staggered grid. This simplifies the next step, which is to obtain the boundary condition from MD.

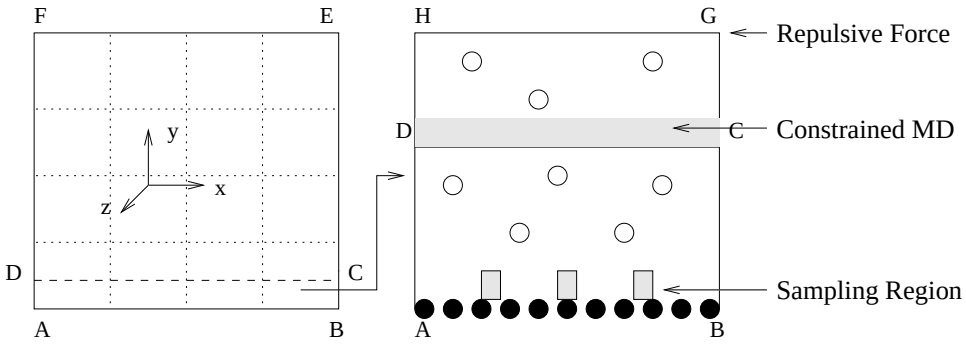

Figure 15: Schematic of the multiscale method for the example of Marangoni flow. In the left panel, the finite volume grid is indicated by the dotted lines. The boundary condition at AB is extracted from molecular dynamics simulations confined in $ABCD$. The set-up of the MD simulation is shown in the right panel. Particles are confined by a repulsive force at GH and the solid wall at AB. The dynamics of the particles in the strip CD are constrained by the continuum velocity field. The boundary conditions are extracted from the small bins at the lower boundary. Black dots represent atoms in the solid.

The needed data in the finite volume projection method are the *tangential* stresses at the boundary.

The schematic of the MD is shown in Fig. 15. Periodic boundary condition is imposed in the x- and z-direction. In the y-direction, the fluid is confined by a solid wall at AB and a repulsive force at GH. One choice of this repulsive potential is the repulsive part of the LJ potential:

$$P(r)=\varepsilon\left(\frac{\sigma}{r}\right)^{12}, \tag{4.20}$$

where r is the distance to GH. Similar techniques for confining particles were used in [84, 85].

The MD is constrained by the macroscale velocity field. This is done as follows. Each particle in the strip CD is assigned the velocity: $\mathbf{u}(\mathbf{x})=\mathbf{u}^c(\mathbf{x})+\tilde{\mathbf{u}}$, where $\mathbf{u}^c(\mathbf{x})$ is the velocity from the continuum calculation and $\tilde{\mathbf{u}}$ is the thermal velocity that obeys the Maxwellian distribution at some temperature T. Therefore the strip plays a two-fold role here: As a momentum reservoir it maintains the non-equilibrium dynamics at the steady state; as a thermal reservoir it releases heat generated by viscous flow from the system.

The solid wall also needs to be explicitly modeled, here as a crystal lattice. Geometric as well as chemical heterogeneities can be modeled by choosing appropriate atomistic potentials (see [140, 146]).

After a relatively short equilibration time, the stresses are estimated using the Irving-Kirkwood formula, as was done before.

Fig. 16 shows some results of the effective boundary conditions extracted from the molecular dynamics simulation. For more numerical results, we refer to [146].

The overall algorithm for a typical macro time step k is as follows:

Step 1 Calculate the stress at the boundary AB by local MD simulation. The MD is constrained by $\mathbf{u}^k$;

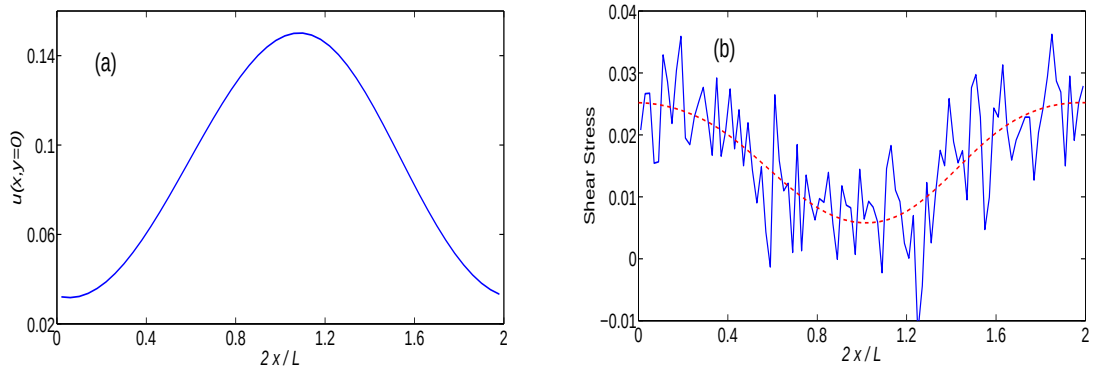

Figure 16: (a): the velocity at the lower boundary; (b): the stress extracted from MD (solid curve) and fitted by fourth-order B-splines (dashed curve).

Step 2 Solve the continuum equations to get $\mathbf{u}^{k+1}$.

4.3.2 Contact line dynamics

We next consider the motion of two immiscible fluids on a solid surface. Continuum hydrodynamics breaks down in the vicinity of the contact line, where the fluid-fluid interface meets the solid surface. Specifically the usual no-slip boundary condition used in macroscopic fluid dynamics leads to an unphysical divergent shear stress and dissipation rate [52]. Molecular dynamics simulations of Couette or Poiseuille flow show relative slip between the fluid and the wall around the contact line [141, 171].

As for the previous example, a HMM procedure is called for in order to obtain boundary conditions from MD. However the present problem is quite a bit more complicated.

Macroscale solver

As the macroscale model, we take

$$\begin{cases} \rho\partial_t \mathbf{u} = \nabla\cdot\tau, \\ \nabla\cdot\mathbf{u} = 0, \\ \dot{\mathbf{x}}_\Gamma = \mathbf{u}, \end{cases} \tag{4.21}$$

where the momentum flux in continuum theory is given by

$$-\tau = \rho\mathbf{u}\otimes\mathbf{u} + pI - \mu(\nabla\mathbf{u}+\nabla\mathbf{u}^T) + \gamma(I-\hat{\mathbf{n}}\otimes\hat{\mathbf{n}})\delta_\Gamma - f_0 xI. \tag{4.22}$$

The last equation in (4.21) says that the fluid-fluid interface $\mathbf{x}_\Gamma(t)$ is advected by the velocity field of the fluid. The first term in the momentum flux is due to convection, the second term is the pressure, the third term is the viscous stress, the fourth term corresponds to the surface tension force which is concentrated at the fluid-fluid interface $\mathbf{x}_\Gamma$

(δ_Γ is the surface delta function), and the last term is the external force. I is the identity matrix, γ is the the surface tension coefficient and $\hat{\mathbf{n}}$ is the unit normal of the interface.

In the numerical calculations, it is standard to replace the surface tension term $\tau_\Gamma = \gamma(I-\hat{\mathbf{n}}\otimes\hat{\mathbf{n}})\delta_\Gamma$ as a body force defined by

$$\tilde{\tau}_\Gamma(\mathbf{x}) = \int_{R^2} D(\mathbf{x}-\mathbf{y})\tau_\Gamma(\mathbf{y})d\mathbf{y}. \tag{4.23}$$

One choice for the kernel D is given by

$$D(\mathbf{x}) = \begin{cases} (2d)^{-2}(1+\cos(\pi x/d))(1+\cos(\pi y/d)), & \text{if } |x|<d, |y|<d; \\ 0, & \text{otherwise.} \end{cases} \tag{4.24}$$

This was first introduced by Peskin [134]. In the examples reported below, d, the width of the smoothing region, is taken to be twice the cell size. After being interpolated from the interface to the grid points by (4.23), the total flux is conserved.

As before we use the projection method for the macroscale equation. The interface is updated by forward Euler method:

$$\frac{(\mathbf{x}_\Gamma)^{n+1}-(\mathbf{x}_\Gamma)^n}{\Delta t} = \mathbf{u}^n. \tag{4.25}$$

The interface is represented by a collection of discrete points $\{(\mathbf{x}_\Gamma)_i, i=0,1,\cdots,N\}$, where the two end points $(\mathbf{x}_\Gamma)_0$ and $(\mathbf{x}_\Gamma)_N$ are the contact points, i.e. the intersections of the interface with the solid walls. Surface tension force is calculated at the middle of each segment. Neumann condition on velocity is used at the in-flow and out-flow boundaries. At the solid wall away from the contact point, no-slip boundary condition is used. Other details of the macroscale solver can be found in [146].

Microscopic solver and estimating boundary conditions

The data that need to be estimated from MD are:

1. shear stress near the contact line (here the contact point);
2. velocity of the contact line.

The schematics of the molecular simulation around the contact line is shown in Fig. 17. Periodic boundary conditions are imposed in the z-direction. In the x-direction, the flow field is not necessarily periodic, so we enlarge the simulation box to $G'H'C'D'$ and impose periodic boundary conditions on $G'D'$ and $H'C'$ instead (see the right panel in Fig. 17). The enlarged part serves as a particle reservoir. In this system we have two species of fluids, fluid I on the left and fluid II on the right. When a fluid particle of species II crosses $H'C'$, it will enter the box through $G'D'$ and become species I, and vice versa.

In the y-direction, the particles are confined by the solid wall at $G'H'$ and a repulsive force at $C'D'$. The repulsive force is modeled by the repulsive part of the LJ potential, as

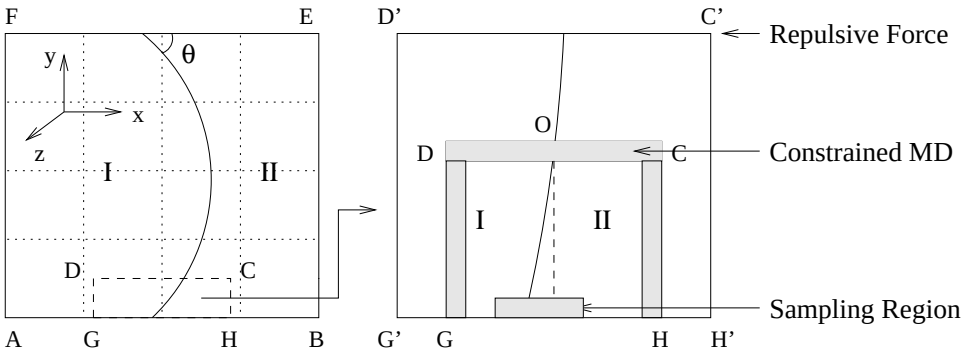

Figure 17: Schematic of the multiscale method for the contact line problem. Macro grid used in the computation is represented by dotted lines in the left panel. MD is carried out in a local region around the contact line. Periodic boundary conditions are imposed on the boundaries of the enlarged box $G'D'$ and $H'C'$. The dynamics in the shaded strips GD, DC and CH are constrained by continuum velocity field. The shear stress and the position of the contact point are computed in the strip along GH.

given in (4.20). The repulsive force is used to keep the particles from escaping the MD domain. More detailed information on the microscale solver is given in [146].

For consistency between the molecular dynamics and the continuum dynamics, a modified Andersen thermostat is used in the strips GD,DC, and CH: At Poisson distributed times with certain frequency ν, a random particle is selected from the strips and its velocity is replaced by $\mathbf{u}(\mathbf{x})=\mathbf{u}^c(\mathbf{x})+\tilde{\mathbf{u}}$, where $\mathbf{u}^c$ is the velocity from continuum dynamics and $\tilde{\mathbf{u}}$ is a random variable with Maxwell-Boltzmann distribution at the specified temperature T.

The shear stress is calculated using the formula (4.7) in the bins which are a few (about 3) atomic lengths above the wall.

To estimate the position of the contact line, we first calculate the particle density function along the fluid-solid interface (remember O is fixed):

$$\rho(x)=\sum_i \rho_i \delta(x_i-x), \tag{4.26}$$

where the sum is over all particles in the strip above the solid wall, x_i is the x coordinate of the i-th particle, ρ_i is 1 for particles of species I and -1 for particles of species II. The position of the contact line is determined by $\rho(x)=0$. [146] suggests taking a strip which is again a few atomic lengths above the wall and partition it into uniform bins in x direction. Then the density is obtained by taking the sum of ρ_i in each bin. The position of the contact line is given by

$$(x_\Gamma)_0=x_0+\int_{x_0}^{x_1}\tilde{\rho}(x)dx, \tag{4.27}$$

where x_0 and x_1 are the positions of the leftmost and the rightmost bins respectively. $\tilde{\rho}(x)$, which is between 0 and 1, is the rescaled density:

$$\tilde{\rho}(x)=\frac{\rho(x)-\min_x\rho(x)}{\max_x\{\rho(x)-\min_x\rho(x)\}}. \tag{4.28}$$

Numerical results

The overall algorithm for a typical macro time step k looks like the following:

Step 1 Carry out a constrained MD simulation near the contact line, from which the shear stress and the position of the contact line are estimated;

Step 2 Solve equations in (4.21) for $\mathbf{u}^{k+1}$ and $(\mathbf{x}_\Gamma)^{k+1}$.

We will discuss two examples from [146]. The first example is a validation study. The second is an example of asymmetric fluid-solid interactions.

Example 4.1. Two immiscible fluids are confined in a channel and driven by an external force $f_0 = 0.02$ in the x direction. The system measures $69.7 \times 22.5 \times 5.16$ and contains 2944 particles of each fluid and 1728 solid particles. The system is periodic in the x and z directions.

To check the validity of the constrained molecular dynamics used in the hybrid method, a local MD simulation is performed around the contact line. The left panel of Fig. 18 shows the time series for the difference of the particle numbers of both species inside $GDCH$ (see Fig. 17). We clearly see a transient time during which the particles of species I flow out of the box and particles of species II flow into the box. The right panel of Fig. 18 is a comparison between the shear stress calculated on the surface of the solid wall in the full MD simulation and in the local constrained MD simulation, and we see good agreements.

The validation study was also carried out for the steady-state solution. The parameters in the continuum model are $\rho = 0.81, \mu = 2.0$ and $\gamma = 3.7$. 70×20 grid points are used in the spatial discretization, and the time step is $\Delta t = 0.05$. A static configuration was used as the initial data and the external force is slowly increased to 0.02. The steady-state velocity field and the interface (dashed line) are shown in Fig. 19. These results agree well with the full MD results.

Example 4.2. In our next example, we consider the case for which the fluid-solid interaction is different for the two fluid phases. Specifically the attraction between fluid I and the solid is decreased by taking $\eta = 0.7$ in the potential (4.8). All other parameters in the potential are kept unchanged from the previous example. The static contact angle θ in this case is 65°.

Again the static configuration is used as the initial state and an external force $f_0(t) = 5.35 \times 10^{-11} t$ in x-direction is applied until it reaches $f_0 = 2.2 \times 10^{-5}$. The force is then decreased at the same rate until it reaches $f_0 = -7.0 \times 10^{-5}$. The fluid-fluid interfaces at different times are shown in Fig. 20(a) . The left-most dashed line is the interface at the static position, and it travels in the stream-wise direction as the external force increases. The right-most dashed line corresponds to $f_0 = 2.2 \times 10^{-5}$. The solid lines from the right to the left show the shapes of the interfaces as the external force decreases. Fig. 20(b) shows the dynamic contact angle as a function of the applied force. Again, the dashed curve corresponds to the dynamics as the force increases, and the solid curve corresponds to the dynamics as the force decreases.

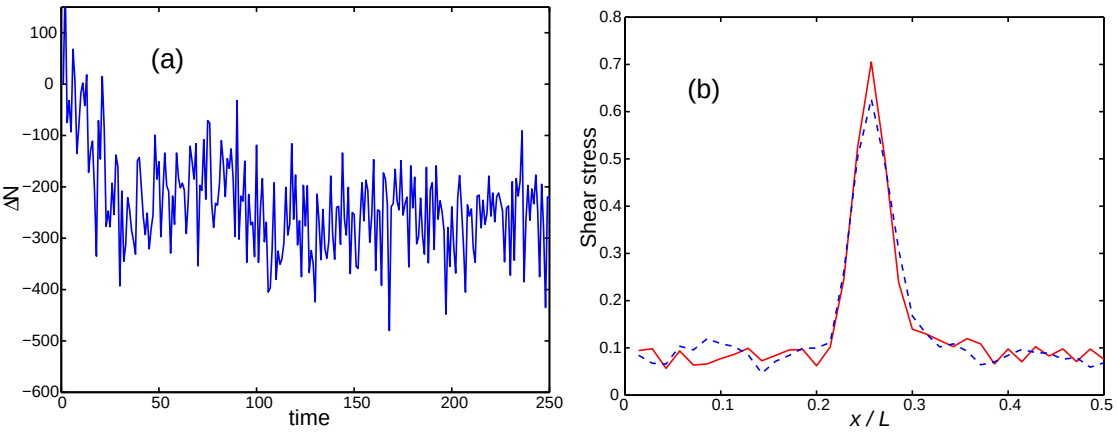

Figure 18: Results of the constrained MD simulation. (a): The time series of $\Delta N = N_I(t) - N_{II}(t)$, where $N_I(t)$ and $N_{II}(t)$ are the particle numbers of the two species in the box $GDCH$ (see Fig. 17) respectively; (b): The shear stress measured at the solid wall. The solid curve is calculated from the full MD simulation and the dashed curve is from the constrained MD simulation.

While the numerical results appear to be quite reasonable and in some cases have been validated by direct MD simulations, the coupling procedures, the way in which constraints are imposed on the MD, are still quite ad hoc. This is a common problem for coupled atomistic-continuum modeling of fluids: So far there has been little systematic study on the accuracy of such coupling procedures. In comparison, more work has been done on this issue for solids.

5 Dynamics of solids at finite temperature

Unlike fluids, the multiscale nature of solids is much more pronounced. On the modeling side, there is no analog of the Navier-Stokes equation as a fundamental macroscopic model. On the physics side, solids often contain a hierarchy of structures and defects at different scales [136]. These include point defects such as vacancies and impurities, dislocations and structures formed by dislocations, grain boundaries, and even cracks. As a result, multiscale modeling has received more attention in solids than in fluids.

We will again focus our discussion on the situation when the macroscopic model is continuum mechanics and the microscopic model is molecular dynamics. For the analysis of static properties of solids at zero temperature, in which case the mathematical models reduce to minimization problems, the quasi-continuum method has had a great deal of success [169]. Here we will discuss multiscale methods that handle the dynamics of solids at finite temperature. This part of the presentation follows mainly [108].

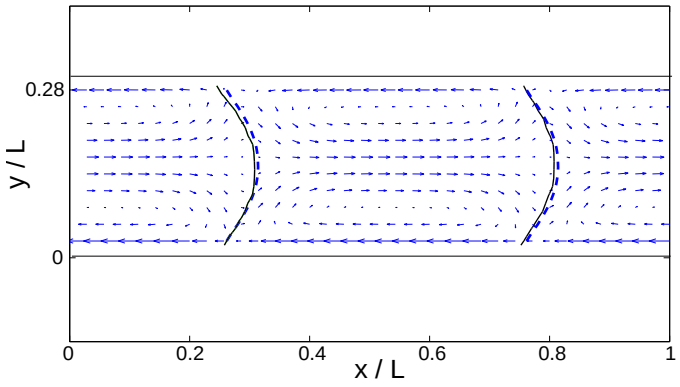

Figure 19: The steady-state solution of Example 4.1 by the hybrid method and comparison with the results of full MD. The interface is shown in dashed curve. The solid curve shows the interface obtained by full MD simulation.

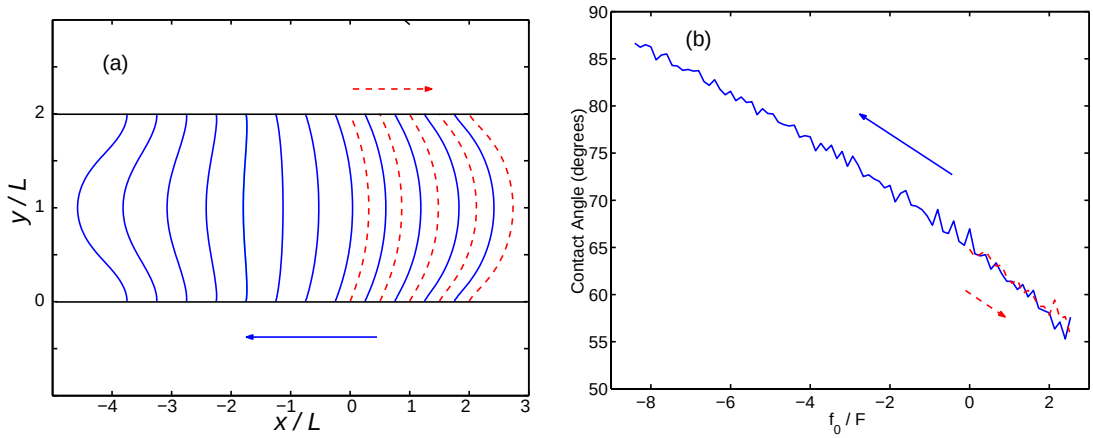

Figure 20: Dynamics of the contact line problem with asymmetric fluid-solid interactions. (a): Fluid-fluid interfaces at different times. For dashed curves from left to right, the external force increases from 0 to 2.2×10^{-5}; For solid curves from right to left, the external force decreases from 2.2×10^{-5} to -7.0×10^{-5}; (b): Dynamic contact angle as a function of external force. The external force is rescaled by $F=8.1\times10^{-6}$.

5.1 Macroscopic and microscopic models

Again the continuum model is expressed in terms of the conservation laws. For solids it is more convenient to work with Lagrangian coordinates. Denote by $\mathbf{x}^0$ the reference coordinate for the solid and $\mathbf{x}=\mathbf{x}^0+\mathbf{u}(\mathbf{x}^0,t)$, the position after deformation, with $\mathbf{u}$ being the displacement. Then the conservation laws take the form:

$$\begin{cases} \partial_t \mathbf{A}-\nabla_{\mathbf{x}^0}\mathbf{v}=\mathbf{0}, \\ \partial_t \mathbf{v}-\nabla_{\mathbf{x}^0}\cdot\boldsymbol{\sigma}=0, \\ \rho_0\partial_t e+\nabla_{\mathbf{x}^0}\cdot\mathbf{j}=0. \end{cases} \tag{5.1}$$

Here $\mathbf{A}$,$\mathbf{v}$,e are the deformation gradient, velocity and total energy per particle respectively, ρ_0 is the initial density, σ is the first Piola-Kirchhoff stress tensor and $\mathbf{j}$ is the energy flux. The first equation in (5.1) is a statement of compatibility between the deformation gradient and the velocity. The second and third equations are conservation of momentum and energy respectively. In continuum mechanics [100], these equations are supplemented by the empirical constitutive relations for stress and energy fluxes. Our interest here is to develop multiscale strategies that bypass these empirical constitutive laws when their accuracy is in doubt.

The microscopic model is again MD. The first step is to derive a set of conservation laws similar to (5.1). For this purpose, we define the following empirical distributions [108],

$$\begin{cases} \widetilde{\rho}(\mathbf{x}^0,t)=\sum_i m_i\delta(\mathbf{x}^0-\mathbf{x}_i^0), \\ \widetilde{\mathbf{v}}(\mathbf{x}^0,t)=\sum_i \mathbf{v}_i(t)\delta(\mathbf{x}^0-\mathbf{x}_i^0), \\ \widetilde{\mathbf{q}}(\mathbf{x}^0,t)=\sum_i m_i\mathbf{v}_i(t)\delta(\mathbf{x}^0-\mathbf{x}_i^0), \\ \widetilde{e}(\mathbf{x}^0,t)=\frac{1}{2}\sum_i\Big[m_i\mathbf{v}_i(t)^2+\sum_{j\neq i}\phi\big(\mathbf{x}_i(t)-\mathbf{x}_j(t)\big)\Big]\delta(\mathbf{x}^0-\mathbf{x}_i^0). \end{cases} \tag{5.2}$$

Here as before we denote by $\mathbf{x}_i^0$ the position of the i-th atom in the undeformed configuration, $\mathbf{x}_i(t)$ and $\mathbf{v}_i(t)$ are respectively the position and velocity of the i-th atom at time t. Let

$$\begin{cases} \widetilde{\sigma}_{\alpha\beta}(\mathbf{x}^0,t)=-\frac{1}{2}\sum_{i\neq j}f_\alpha\big(\mathbf{x}_i(t)-\mathbf{x}_j(t)\big)(x_{i\beta}^0-x_{j\beta}^0) \\ \qquad\qquad \times\int_0^1\delta\big(\mathbf{x}^0-(\mathbf{x}_j^0+\lambda(\mathbf{x}_i^0-\mathbf{x}_j^0))\big)d\lambda, \\ \widetilde{\mathbf{j}}(\mathbf{x}^0,t)=\frac{1}{4}\sum_{i\neq j}\big(\mathbf{v}_i(t)+\mathbf{v}_j(t)\big)\cdot\mathbf{f}\big(\mathbf{x}_j(t)-\mathbf{x}_i(t)\big)(\mathbf{x}_i^0-\mathbf{x}_j^0) \\ \qquad\qquad \times\int_0^1\delta\big(\mathbf{x}^0-(\mathbf{x}_j^0+\lambda(\mathbf{x}_i^0-\mathbf{x}_j^0))\big)d\lambda, \end{cases} \tag{5.3}$$

where $\mathbf{f}=-\nabla V$ is the force and we have only considered two-body interaction in the atomistic potential – extension to the general case can be found in [108]. We have

$$\begin{cases} \partial_t\widetilde{\mathbf{q}}-\nabla_{\mathbf{x}^0}\cdot\widetilde{\sigma}=0, \\ \rho_0\partial_t\widetilde{e}+\nabla_{\mathbf{x}^0}\cdot\widetilde{\mathbf{j}}=0. \end{cases} \tag{5.4}$$

The expressions in (5.3) are nothing but the generalizations of the classical Irving-Kirkwood formula.

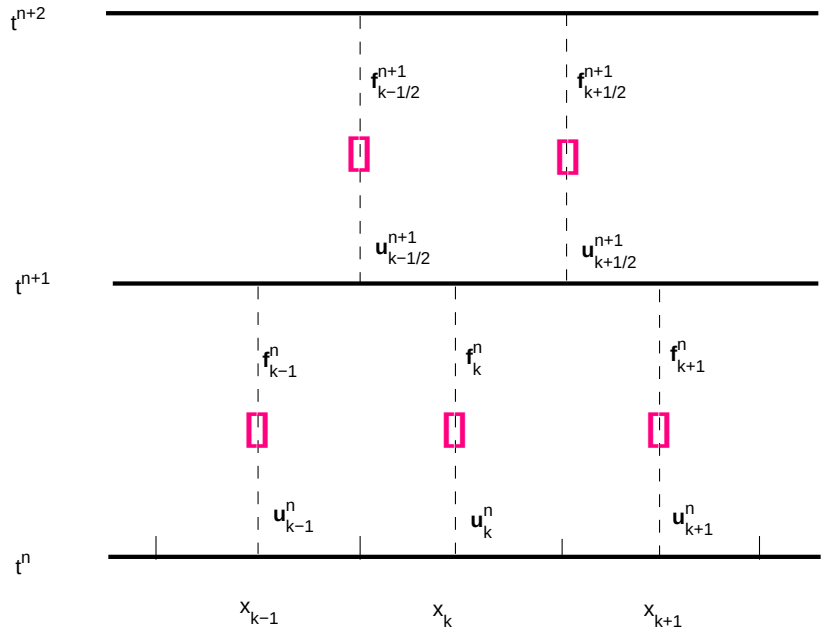

Figure 21: A schematic illustration of the numerical procedure: starting from piece-wise constant solutions $\{\mathbf{w}_k^n\}$, one integrates (5.5) in time and in the cell $[x_k, x_{k+1}]$. To estimate $\mathbf{f}$ at x_k, we perform a MD simulation using $\mathbf{w}_k^n$ as constraints.

5.2 Type B problem: Atomistic-based constitutive modeling

5.2.1 Macroscale solver

Our basic macroscopic model is a set of conservation laws. Therefore, as the macroscale solver, we will choose a finite volume method. Although there are a variety of finite volume methods available for solving conservation laws [80, 105], many of them involve computing the Jacobian of the flux functions, which dramatically increases the computational complexity in a coupled multiscale method when the constitutive relation has to be extracted from atomistic models. An exception is the central scheme of Lax-Friedrichs type, such as the one developed in [122] which is formulated over a staggered-grid. Below we will choose such central schemes as our macroscale solver.

For convenience, we will illustrate the case when the macroscale model is one-dimensional. We rewrite the conservation laws in a generic form,

$$\mathbf{w}_t + \mathbf{f}_x = 0, \tag{5.5}$$

where $\mathbf{w}$ denotes the conserved quantities, and $\mathbf{f}$ is some (unknown) flux function. Fig. 21 shows the overall structure of the method. The first order central scheme represents the solutions by piece-wise constants, which are the average values over each cell:

$$\mathbf{w}_k^n = \frac{1}{\Delta x}\int_{x_{k-1/2}}^{x_{k+1/2}} \mathbf{w}(x, t^n)dx.$$

Here Δx is the size of the cell. Integrating (5.5) over $[x_k, x_{k+1}]\times[t^n, t^{n+1})$ leads to the following:

$$\mathbf{w}_{k+1/2}^{n+1} = \frac{\mathbf{w}_k^n + \mathbf{w}_{k+1}^n}{2} - \frac{\Delta t}{\Delta x}\left(\mathbf{f}_{k+1}^n - \mathbf{f}_k^n\right), \tag{5.6}$$

where

$$\mathbf{f}_k^n = \frac{1}{\Delta t}\int_{t^n}^{t^{n+1}} \mathbf{f}(x_k, t)dt.$$

This is then approximated using numerical quadrature such as the mid-point formula. A simple choice is $\mathbf{f}_k^n \sim \mathbf{f}(x_k, t^n)$.

The overall procedure is as follows. At each macro time step, the scheme (5.6) requires as input the fluxes at the grid points x_k. These flux values are obtained by performing local MD simulations that are constrained by the local macro state variables $\mathbf{A}, \mathbf{v}, e$. After the MD system equilibrates, we estimate the fluxes by time/ensemble averaging.

Higher-order schemes and generalization to high dimensions are discussed in see [108].

5.2.2 Constrained microscale solver

Next we discuss how to set up the MD in order to measure the fluxes. As for the case of fluids, we will make a constitutive assumption that the fluxes depend only on the local function values of the conserved densities. More general constitutive assumptions can be accommodated, but the constrained MD that we discuss below will have to be modified.

First we initialize the MD. The basic requirement is that the initial condition has be to consistent with the local conserved quantities of the macroscopic state, and has the correct crystal structure. Given the values of the local macroscopic state variables $\mathbf{A}$,$\mathbf{v}$,e, we first determine the shape of the MD cell from the deformation gradient tensor A. Consider the situation that the crystal is a simple Bravais lattice and let $\mathbf{E}$ be a basis for the undeformed unit cell. The deformed lattice is generated by the basis vectors $\tilde{\mathbf{E}} = \mathbf{A}\mathbf{E}$. We then place the atoms on the deformed lattice, possibly with small perturbations. The potential energy $\mathcal{U}$ of this trial configuration and the kinetic energy associated with the mean velocity $\mathbf{v}$ is subtracted from the total energy e to give us the thermal energy. If this value is positive, the trial configuration is accepted. Otherwise, it is rejected. From the thermal energy one computes the temperature. The velocities of the atoms are initialized according to the Maxwell-Boltzmann distribution with the mean and variance given by the macroscale velocity $\mathbf{v}$ and the temperature respectively.

Another idea is to use the previously computed microscopic state as the initial configuration for the new MD simulation. Of course the previously computed microscopic state has to be modified in order to be consistent with the current macro state. This can be done as follows.

1. The configuration is deformed linearly so that it is consistent with the current deformation gradient.
2. The average velocity is shifted to the current average velocity.

3. The temperature (and hence the fluctuating part of the velocity) is changed using the same procedure as discussed above to arrive at the required total energy.

The choice of the size of the MD system is affected by two competing factors. On one hand the size of the system has to be large enough in order to minimize the effect of the boundary conditions. On the other hand, as the system size goes up, not only the cost goes up, the relaxation time also goes up.

Boundary conditions have to be imposed on the microscopic system in order to guarantee consistency with the local macroscale variables. In the present case since the system is homogeneous (constant mean velocity, temperature and deformation gradient), the most convenient boundary condition is the periodic boundary condition. The MD is performed in a deformed box as described earlier and periodically extended to the whole space.

The periodic boundary condition excludes the possibility of accounting for inhomogeneous effects such as effects of thermal gradients, strain gradients, etc. Extending the methodology to cover these effects is still on-going work.

From the MD data, we can compute the microscopic fluxes using the formulas in (5.3). The final step is to average the microscopic fluxes to obtain the fluxes needed by the macroscopic scheme. This is very similar to the situation for fluids and therefore we will omit the details. The interested reader can consult [108].

We remark that this procedure allows us to automatically decouple the micro time scales from the macro time scales.

An error analysis of the overall method can be found in [61].

5.2.3 Modeling thermal expansion using MD

As an example, we study the effect of thermal expansion in a crystal. Our atomistic model is a 3D Lennard-Jones solid, on a FCC (face-centered cubic) lattice. We set up the example so that the macroscale behavior is two dimensional. Initially the material is at rest with homogeneous temperature distribution $T \equiv 0.1$. We then increase the temperature in the middle instantaneously to $T = 0.4$. This results in a thermal expansion that propagates outward. The result of HMM is shown in Fig. 22 where we display the computed temperature distribution as well as the velocity field on the macro grid. One clearly observes that the material expands outward as heat is spread out.

5.3 Type A problem: Dealing with isolated defects

We now turn to another class of problems that can be treated using multiscale methods, the problem of isolated defects. Solids often contain a variety of defects. To a large extent, the structure and dynamics of these defects determine the properties of the solid [136].

A common idea for the multiscale modeling of defects is to use atomistic models near defects and continuum models away from defects, e.g. in a domain decomposition framework. MAAD is a good example of such an approach [5,6]. The HMM philosophy, on the other hand, suggests a strategy that is closer to adaptive model refinement. One

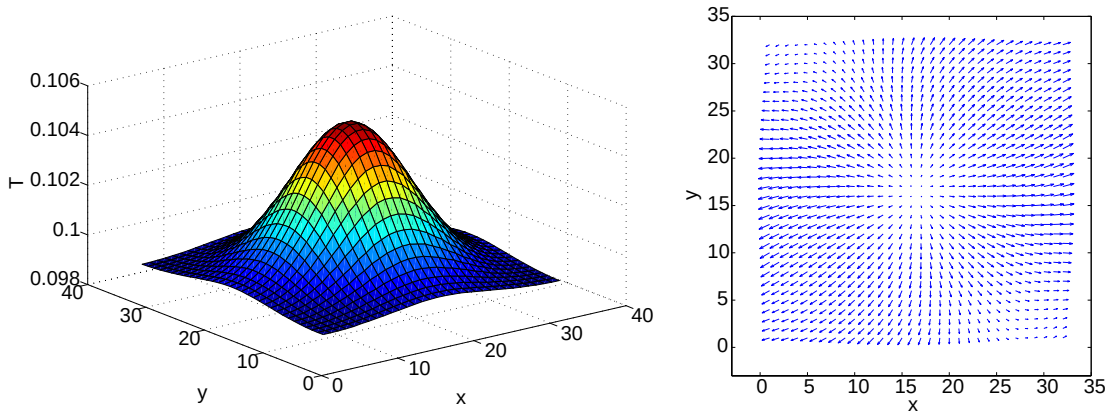

Figure 22: Thermal expansion: temperature distribution (left) and the velocity field (right). The macro mesh consists of 36×36 grid points. Each MD cell contains $36\times36\times3\times4$ atoms, and the MD system is evolved for 10^4 time steps.

starts with a macroscale model on a macro-grid (which might be locally refined) in the entire computational domain and couple with a more refined model locally near the defects. For the present problem, the macroscale model is the same as before, namely the conservation laws. The macroscale solver can also be chosen as before, i.e. central type of finite volume schemes. But when it comes to computing the fluxes, the cells (more precisely, the cell boundaries where flux evaluation is carried out) are divided into two types: cells that contain defects and cells that do not contain defects. In cells that do not contain defects we evaluate the fluxes using either empirical constitutive relations or the method discussed in the previous section. In cells that do contain defects we compute the fluxes using MD.

5.3.1 The relevant time scales

To formulate the procedure of coupling MD with the continuum models near defects, we distinguish two different situations depending on relative magnitude between the time scale for defect motion and the time scale for the local relaxation of the defect structure. We denote the former by T_d and the latter by T_r.

If T_d is much larger than T_r, we can extend the macroscale model to include the velocity of the defect. The macroscale scheme then contains two components: a solver for the conservation laws (a central type finite volume scheme or discontinuous Galerkin method) and defect tracking. The data to be measured from MD include the fluxes, the defect velocity and the local environment variables of the defect. This procedure naturally decouples the two time scales T_r and T_d. The defect tracking procedure has been demonstrated in [108] for co-dimension one defects, such as twin and grain boundaries. Extending this procedure to dealing with high co-dimensional defects such as point defects and dislocations still remains open.

If T_d is comparable to T_r, then the time history of the defect is important for its future

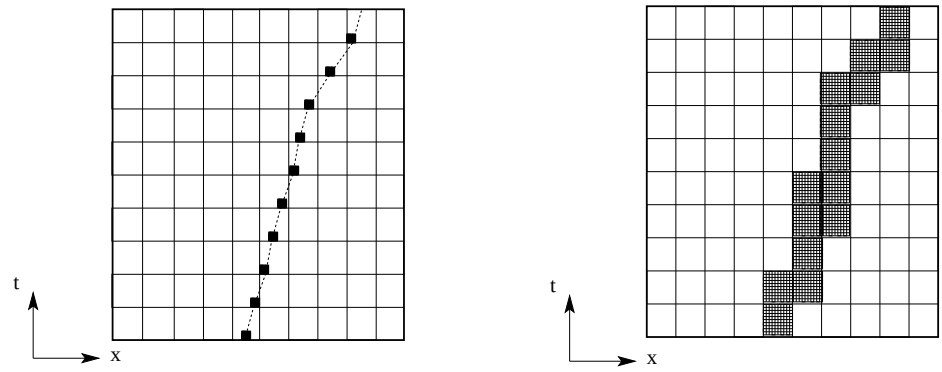

Figure 23: Schematic of the adaptive modeling refinement. The left figure shows the case where $T_r \ll T_d$. The MD simulations are carried out inside the black boxes. The dashed lines represents the interface. The right figure shows the other case where T_r and T_d are comparable. Here one has to keep track the local defect structure for all time by MD simulation.

dynamics. There is no need to decouple the time scales since there is no time scale separation. In this case re-initializing the defect structure at macro time steps, as is commonly done under the framework of HMM, is no longer needed and is in general less accurate. Instead, we should track the entire history of the local atomic structures near the defect. This situation often arises when dealing with small-size materials.

Fig. 23 illustrates the procedure for both cases.

5.3.2 MD boundary conditions

Another difference with the type B problems discussed earlier is that the local MD simulations are no longer homogeneous. It then becomes highly non-trivial to impose the constraints on the MD, which are typically done in the form of boundary conditions. There are two main issues that need to be addressed as far as boundary conditions are concerned. The first is the handling of the phonons. Atomistic and continuum models represent phonons very differently. In atomistic models, phonons are represented in the form of lattice waves. In continuum models, they are represented by the temperature field. Ensuring consistency between these two vastly different representations is a highly non-trivial problem. The second is the handling of defects. For example, dislocations might be emitted during crack propagation, and the MD boundary conditions have to have the ability to allow such dislocations to leave the computational domain smoothly.

There has been relatively little work done on the second problem. The closest related work is that of Shilkrot, Curtin and Miller on CADD (continuum-atomistic dislocation dynamics) [163, 164].

Much work has been done on the first problem, and a fairly complete picture has emerged. We refer to [110, 184] for the details of this discussion.

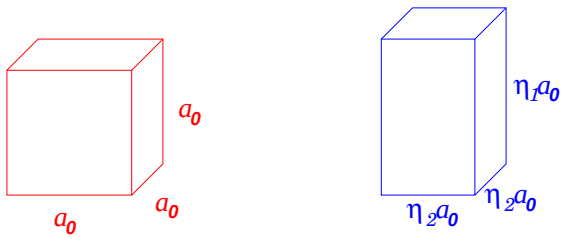

Figure 24: Cubic and tetragonal phases for Ni-Al alloys.

5.3.3 Twin boundary dynamics in Ni-Al alloy

To see how these ideas can be applied to a realistic problem, we summarize the results of [108] for the example of twin boundary dynamics in a $Ni_{62.5}Al_{37.5}$ alloy. The atomistic model uses the EAM potential developed by Voter and Chen [176], which is specifically designed for Ni-Al alloys. At this percentage twin boundaries have been observed both experimentally [31] and in atomistic simulations (with this EAM potential) [17]. In particular the EAM potential has predicted a tetragonal structure with three variants. The corresponding strain matrices can be written as,

$$U_1=\begin{pmatrix}\eta_1 & 0 & 0\\ 0 & \eta_2 & 0\\ 0 & 0 & \eta_2\end{pmatrix},\quad U_2=\begin{pmatrix}\eta_2 & 0 & 0\\ 0 & \eta_1 & 0\\ 0 & 0 & \eta_2\end{pmatrix},\quad U_3=\begin{pmatrix}\eta_2 & 0 & 0\\ 0 & \eta_2 & 0\\ 0 & 0 & \eta_1\end{pmatrix}. \tag{5.7}$$

The cubic structure with lattice constant $a_0=2.871$ Åis chosen as the reference configuration. The parameters η_1 and η_2 can be thought of as being the stretch along the principal axis illustrated in Fig. 24. The values of these parameters are obtained from MD simulation: $\eta_1=1.2263$ and $\eta_2=0.9061$.

For convenience the material is arranged so that the twin plane coincides with the y-z plane. The deformation corresponding to the undeformed variant I and variant II are:

$$\mathbf{A}_1=\begin{pmatrix}\frac{\sqrt{2}\eta_1\eta_2}{\sqrt{\eta_1^2+\eta_2^2}} & 0 & 0\\ \frac{\eta_1^2-\eta_2^2}{\sqrt{2(\eta_1^2+\eta_2^2)}} & \frac{\sqrt{\eta_1^2+\eta_2^2}}{\sqrt{2}} & 0\\ 0 & 0 & \eta_2\end{pmatrix},\quad \mathbf{A}_2=\begin{pmatrix}\frac{\sqrt{2}\eta_1\eta_2}{\sqrt{\eta_1^2+\eta_2^2}} & 0 & 0\\ \frac{\eta_2^2-\eta_1^2}{\sqrt{2(\eta_1^2+\eta_2^2)}} & \frac{\sqrt{\eta_1^2+\eta_2^2}}{\sqrt{2}} & 0\\ 0 & 0 & \eta_2\end{pmatrix}. \tag{5.8}$$

The dynamics of the twin boundary is driven by a shear that is applied at the left boundary. Away from the twin boundary, local MD simulations are performed to estimate the stress as was done for type B problems. Each such simulation involves $20\times20\times5$ atomic units and 2000 steps of time integration. Near the twin boundary the defect tracking technique is applied to estimate the moving speed of the twin boundary and the local strain and stress. Each such MD calculation is carried over a system with $120\times20\times8$ atomic units for 1200 time steps. In all the MD simulations the time step is taken to be δt=0.003 ps. Since the twin boundary simply moves in the x direction, and the continuum

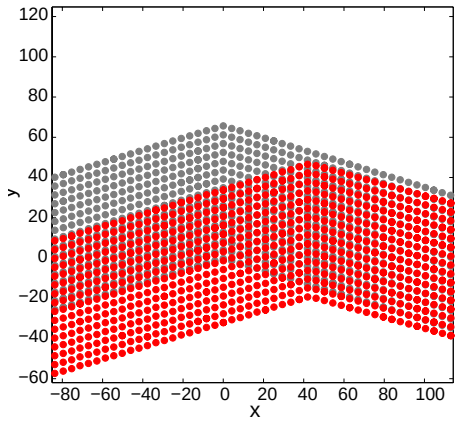

Figure 25: Propagation of twin boundary under stress: shear stress is applied at the left boundary of the sample. The initial positions of the atoms are plotted in light color. The positions after 1.2 ps are plotted in dark color.

quantities do not have appreciable change in the y direction, the continuum equations can be simplified to

$$\begin{cases} \partial_t A_{11} - \partial_x v_1 = 0, \\ \partial_t A_{21} - \partial_x v_2 = 0, \\ \partial_t v_1 + \partial_x \sigma_{11} = 0, \\ \partial_t v_2 + \partial_x \sigma_{21} = 0. \end{cases} \tag{5.9}$$

For simplicity the energy equation is neglected in this problem, and is replaced by constraining the system at constant temperature. Other components of $\mathbf{A}$ are assumed not to change in time.

Fig. 27 shows the numerical results at the macroscale level after some macro time steps. As the twin boundary propagates, two elastic waves are generated and move away from the twin boundary.

To better understand the mechanism of twin boundary propagation, we plot in Fig. 25 some results from the local MD simulation at the twin boundary. We first select an arbitrary plane of atoms and examine their positions at the initial and final times of the MD. Different variants of the twin are easily identified as rectangular lattices with different orientation. We see that at the end of the MD, the twin boundary has clearly moved forward (in a layer by layer fashion).

Next we examine what happens on the twin plane as it propagates forward. For that purpose we plot the atomic positions of the atoms on the twin plane. Fig. 26 clearly suggests that the twin plane moves by a nucleation and propagation mechanism, very much similar to the mechanism of epitaxial growth of crystals. New variants are first nucleated and form islands on the twin plane. The edges of the islands then propagate out and induce the transformation on the whole plane.

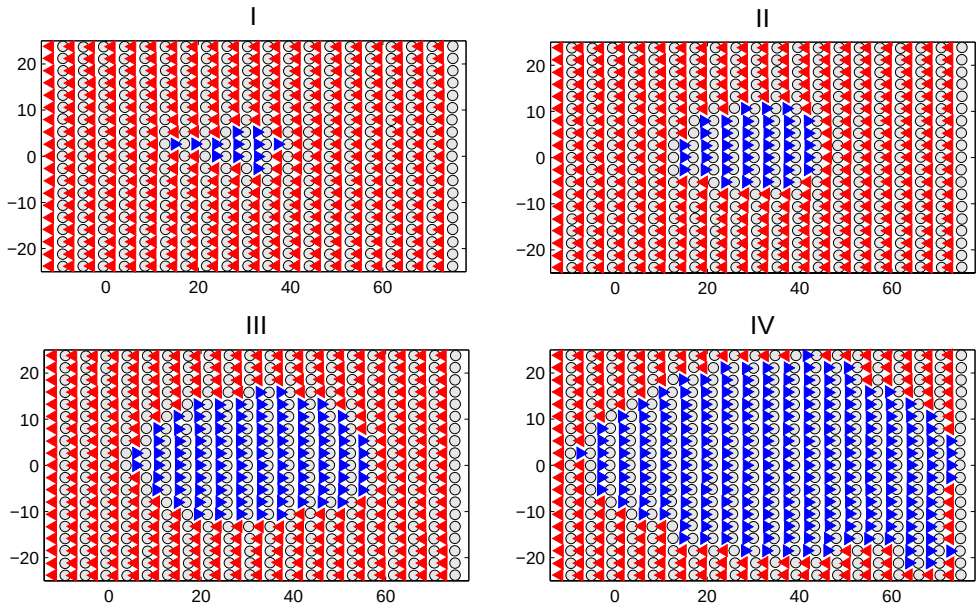

Figure 26: Nucleation and propagation of new variant: '◁': atoms in the twin plane that are still in the original variant. '▷': atoms that have transformed to the new variant. Circle atoms belong to the layer next to the twin plane which are still in the original variant. They are used as reference atoms. Transformed atoms are closer to circle atoms at the right, whereas untransformed atoms are close to circle atoms at the left.

6 Interface problems

In this section we discuss how the HMM philosophy can be applied to the study of interface motion in a multi-scale setting. This discussion follows that of [35]. Our main interest is to capture the macroscale dynamics of the interface in cases where the macroscale velocity of the interface is not explicitly specified. Instead, it has to be extracted from an underlying microscale model. Examples of such microscale models include:

1. Microscale interface dynamics with interfacial velocity of the form

$$V_n(x) = c^\epsilon(x,\gamma), \tag{6.1}$$

where γ denotes the microscale interface. A simple example of $c^\varepsilon(x,\gamma)$ is

$$c^\varepsilon(x) = c\left(x,\frac{x}{\epsilon},\gamma\right). \tag{6.2}$$

Such models arise in the study of interface propagation in strongly heterogeneous media such as composite materials, polycrystals, materials with impurities, and porous media, to name a few. (6.2) is a homogenization problem. In the case when the microstructure is periodic, homogenized equations have been derived in [111].

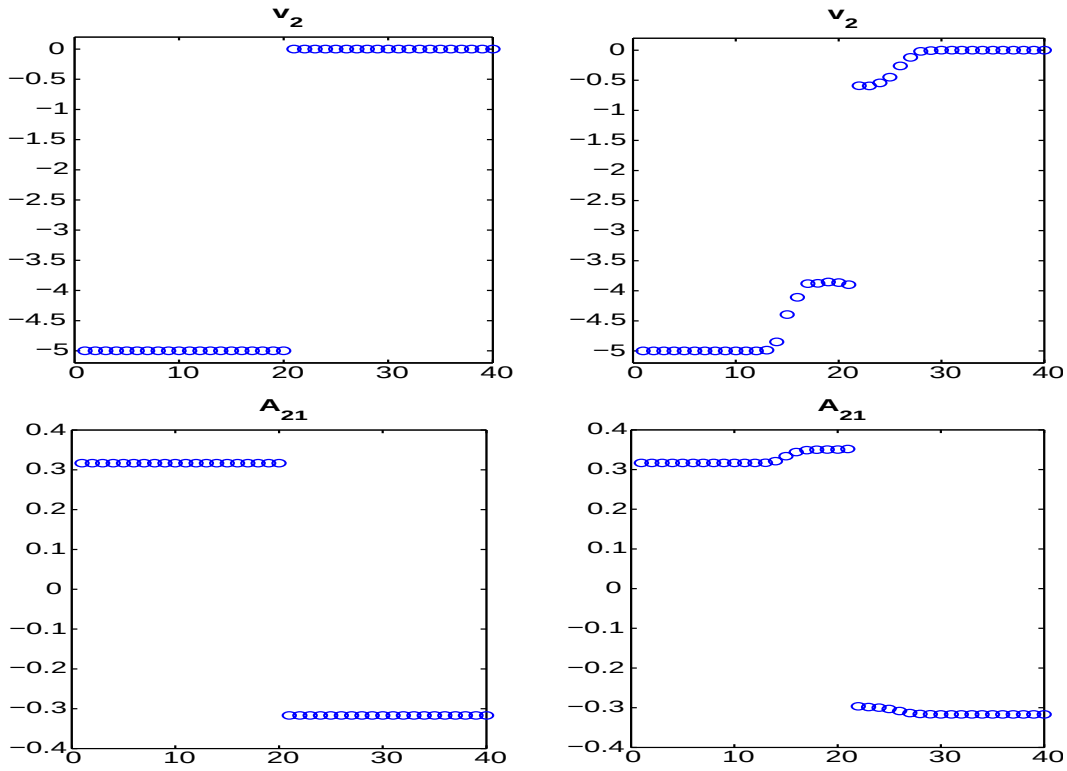

Figure 27: Left: the initial data for $A_{2,1}$ and v_2 (100 m/s); Right: the numerical results in 15 macro time steps.

2. Front propagation in phase-field models. Consider, for example, the Allen-Cahn equation

$$u_t = \epsilon \Delta u + \frac{1}{\epsilon} u(1-u^2). \tag{6.3}$$

It is well-known that for small ϵ, (6.3) describes the propagation of a front whose inward normal velocity is the mean curvature of the front. In this case, we simply have to solve the mean curvature flow equation (instead of the microscale model (6.3)) in order to capture the large scale dynamics of the front. However, if the phase field model takes a more complex form or if non-trivial chemical reactions occur at the front, analytically deriving the effective dynamic laws for the front becomes a difficult task. Therefore it is of interest to develop numerical methods that capture the large scale dynamics of the interface, and use only microscale models of the type (6.3). Such ideas have been explored in the work of R. Klein et. al [155].

3. Discrete microscale models such as kinetic Monte Carlo algorithms or molecular dynamics. Examples include the dynamics of step edges on the surface of an epitaxially grown crystal, grain boundaries in solids, and many more.

6.1 Macroscale solver: The level set method

As the macroscale solver we may use any of the conventional methods for interface dynamics such as the level set method [127], front tracking [79], or the segment projection method [173]. Here we will follow [35] and focus on the level set method. Alternative approaches can be found in [168].

In the framework of the level set method, an interface is described as the zero level set of a globally defined function, ϕ, called a level set function. All operations, in particular, the evolution, are then performed on this function in place of the interface of interest. The level set function ϕ satisfies the PDE:

$$\phi_t + V \cdot \nabla \phi = 0,$$

where V is a globally defined velocity field. On the interface, this is equivalent to

$$\phi_t \pm V_n |\nabla \phi| = 0, \tag{6.4}$$

which involves the normal velocity only. In many problems, though, the velocity is only naturally specified at the interface. Many techniques are available to extend the velocity to the whole ambient space [7, 8, 87, 159].

6.2 Estimating the macroscale interface velocity

The data that need to be estimated from the microscale models are the normal velocities of the macroscale interface at each macroscale grid point. The first step is to locally reconstruct the interface. If the normal velocity of the macroscale interface is known to only depend on the orientation of the local tangent plane of the interface, then we may approximate the interface locally by a hyperplane. On the other hand, if the normal velocity is also known to depend on the local curvature, a quadratic approximation is needed.

As an illustration, we first consider the homogenization problem. The level set representation of the microscale model in this case takes the form

$$\phi_t + c\left(x, \frac{x}{\epsilon}\right) |\nabla \phi| = 0, \tag{6.5}$$

which describes motion in the normal direction at speed c. In this case, we can use the hyperplane reconstruction. [35] suggests working on a transformed coordinate through a change of variables so that this hyperplane coincides with the $\{x_n = 0\}$-plane. The original microscale model (6.5) is then solved in a domain Δ in the transformed space, rectangular with sides orthogonal to the coordinate axes, that should be larger than the size of the periodic cell or the correlation length of c (see Fig. 28). Periodic boundary conditions are imposed in the $x_1, x_2, \cdots, x_{n-1}$-directions and a periodic jump condition can be imposed in the x_n-direction.

To extract the quantity of interest, at each microscale time step, the microscale Hamiltonian is averaged in the central region $\tilde{\Delta}$ of the domain to reduce spurious effects that

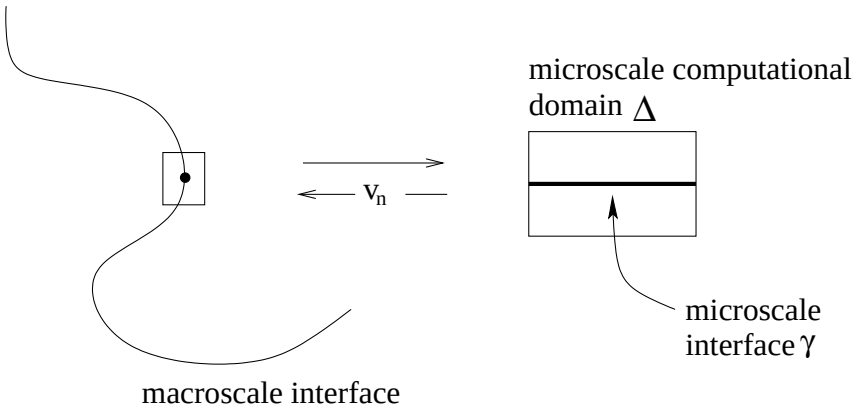

Figure 28: A pictorial description of the HMM setup showing the link between the macroscopic and microscopic levels.

may arise from the boundary and the chosen boundary conditions. Denote this value by $h^\epsilon(t)$

$$h^\varepsilon(t)=\frac{1}{|\tilde{\Delta}|}\int_{\tilde{\Delta}} c^\varepsilon(x)|\nabla\phi(x,t)|dx, \tag{6.6}$$

the velocity of the front at the particular location is obtained from

$$V_n=\frac{1}{|\nabla\phi|}\int_0^{t^*} h^\epsilon(t)K\left(\frac{t}{t^*}\right)\,dt. \tag{6.7}$$

Here K is an averaging kernel, as discussed earlier. Having obtained V_n at all the macroscale grid points at the interface, the interface can be evolved using standard procedures in the level set method.

[35] also considered the case where the microscale model is described by a phase-field equation:

$$u_t=\nabla\cdot\left(b\left(x,\frac{x}{\epsilon}\right)u\right)+\epsilon\nabla\cdot\left(a\left(x,\frac{x}{\epsilon}\right)\nabla u\right)-\frac{1}{\epsilon}\frac{\partial V}{\partial u}(u), \tag{6.8}$$

where $a(x,y)>0$ and $b(x,y)$ are smooth functions that are either periodic in y or stationary random in y with rapidly decaying correlation at large distances and V is a double well potential with minima at $u=\alpha,\beta$. For the details concerning this example, as well as the numerical results, we refer to [35]. More recent results are found in the thesis [167].

7 Stochastic ODEs with multiple time scales

Consider the following generic example of ODEs with two time scales:

$$\begin{cases}\dot{X}_t^\epsilon=f(X_t^\epsilon,Y_t^\epsilon,\epsilon), & X_0^\epsilon=x,\\ \dot{Y}_t^\epsilon=\dfrac{1}{\epsilon}g(X_t^\epsilon,Y_t^\epsilon,\epsilon), & Y_0^\epsilon=y.\end{cases} \tag{7.1}$$

Here $(x,y)\in\mathbb{R}^n\times\mathbb{R}^m$, $f(\cdot)\in\mathbb{R}^n$ and $g(\cdot)\in\mathbb{R}^m$ are (possibly random) functions that are $\mathcal{O}(1)$ in ϵ, and ϵ is a small parameter representing the ratio of the time-scales in the system. We have assumed that the phase space can be decomposed into slow degrees of freedom x and fast ones y. Depending on the problem, we may be interested in the $\mathcal{O}(1)$ (advective) or $\mathcal{O}(\epsilon^{-1})$ (diffusive) time-scales.

There has been numerous analytical work on systems of the type (7.1) [74,98,115,128]. On the advective time-scale, if the dynamics for Y_t^ϵ with $X_t^\epsilon=x$ fixed has an invariant probability measure $\mu_x^\epsilon(dy)$ and the following limit exists:

$$\bar{f}(x)=\lim_{\epsilon\to 0}\int_{\mathbb{R}^m} f(x,y,\epsilon)\mu_x^\epsilon(dy), \tag{7.2}$$

then in the limit as $\epsilon\to 0$, X_t^ϵ converges to the solution of

$$\dot{\bar{X}}_t=\bar{f}(\bar{X}_t),\qquad \bar{X}_0=x. \tag{7.3}$$

Leading order optimal prediction of Chorin et al. applied to this problem gives the same result [41, 42]. On the diffusive time-scale, fluctuations become important. With the rescaled time $s=\epsilon t$, (7.1) becomes:

$$\begin{cases} \dot{X}_s^\epsilon=\dfrac{1}{\epsilon}f(X_s^\epsilon,Y_s^\epsilon,\epsilon), & X_0^\epsilon=x,\\ \dot{Y}_s^\epsilon=\dfrac{1}{\epsilon^2}g(X_s^\epsilon,Y_s^\epsilon,\epsilon), & Y_0^\epsilon=y. \end{cases} \tag{7.4}$$

Under appropriate assumptions on f and g, the effective dynamics for X_s^ϵ in the limit of $\epsilon\to 0$ is a stochastic differential equation,

$$\dot{\bar{X}}_s=\bar{b}(\bar{X}_s)+\bar{\sigma}(\bar{X}_s)\dot{W}_s,\qquad \bar{X}_0=x, \tag{7.5}$$

where W_s is a Wiener process and the coefficients $\bar{b}$ and $\bar{\sigma}$ are expressed in terms of limits of expectations similar to (7.2). Details can be found in [63]. We will only discuss the dynamics over the advective time scale, and refer to [63] for discussions on the diffusive time scale.

In order to facilitate the discussion that we will present later on error analysis, we consider a more special form of stochastic ODEs:

$$\begin{cases} \dot{X}_t^\epsilon=a(X_t^\epsilon,Y_t^\epsilon,\varepsilon), & X_0^\epsilon=x,\\ \dot{Y}_t^\epsilon=\dfrac{1}{\epsilon}b(X_t^\epsilon,Y_t^\epsilon,\varepsilon)+\dfrac{1}{\sqrt{\epsilon}}\sigma(X_t^\epsilon,Y_t^\epsilon,\varepsilon)\dot{W}_t, & Y_0^\epsilon=y, \end{cases} \tag{7.6}$$

where $a\in\mathbb{R}^n$, $b\in\mathbb{R}^m$, $\sigma\in\mathbb{R}^m\times\mathbb{R}^d$ are deterministic functions and W_t is a d-dimensional standard Wiener process.

Based on the assumption that for small ε, the dynamics of X_t^ε is approximated by that of

$$\dot{\bar{X}}_t=\bar{a}(\bar{X}_t),\qquad \bar{X}_0=x, \tag{7.7}$$

an HMM type of strategy was independently proposed in [175]. The basic idea is to solve (7.7) with a macro-solver in which $\bar{a}$ is estimated by solving the micro-scale problem (7.6).

As the macroscale solver we may use any stable explicit ODE solver such as the forward Euler, Runge-Kutta, or a linear multi-step method. In the simplest case when forward Euler is selected as the macro-solver, we have

$$X_{n+1} = X_n + \tilde{a}_n \Delta t, \tag{7.8}$$

where Δt is the macro time step size.

The data that need to be estimated is $\tilde{a}_n$ which is an approximation of $\bar{a}(X_n)$. We estimate this data in two steps:

1. We solve the second equation in (7.6) using a micro-solver for stochastic ODEs and denote the solution by $\{Y_{n,m}\}$ where m labels the micro-time-steps. Multiple independent replicas can be used, in which case we denote the solutions by $\{Y_{n,m,j}\}$ where j is the replica number.
2. We then define an approximation of $\bar{a}(X_n)$ by the following time and ensemble average:
$$\tilde{a}_n = \frac{1}{MN} \sum_{j=1}^{M} \sum_{m=n_T}^{n_T+N-1} a(X_n, Y_{n,m,j}, \varepsilon),$$
where M is the number of replicas, N is the number of steps in the time averaging, and n_T is the number of time steps we skip to eliminate transients.

For the micro-solver, for each realization we may use the following first order scheme

$$\begin{aligned} Y^i_{n,m+1} &= Y^i_{n,m} + \frac{1}{\sqrt{\varepsilon}} \sum_j \sigma^{ij}(X_n, Y_{n,m}, \varepsilon) \xi^j_{m+1} \sqrt{\delta t} \\ &\quad + \frac{1}{\varepsilon} b^i(X_n, Y_{n,m}, \varepsilon)\delta t + \frac{1}{\varepsilon} \sum_{jk} A^{ijk}(X_n, Y_{n,m}, \varepsilon) s^{kj}_{m+1} \delta t, \end{aligned} \tag{7.9}$$

where δt is the micro-time-step size (note that it only appears in term of the ratio $\delta t/\varepsilon =: \Delta\tau$), and

$$A^{ijk} = \sum_l (\partial^l \sigma^{ij}) \sigma^{lk}. \tag{7.10}$$

Here the derivatives are taken with respect to y. The random variables $\{\xi^j_m\}$ are i.i.d Gaussian with mean zero and variance one, and

$$s^{kj}_m = \begin{cases} \frac{1}{2}\xi^k_m \xi^j_m + z^{kj}_m, & k < j, \\ \frac{1}{2}\xi^k_m \xi^j_m - z^{jk}_m, & k > j, \\ \frac{1}{2}\left((\xi^j_m)^2 - 1\right), & k = j, \end{cases}$$

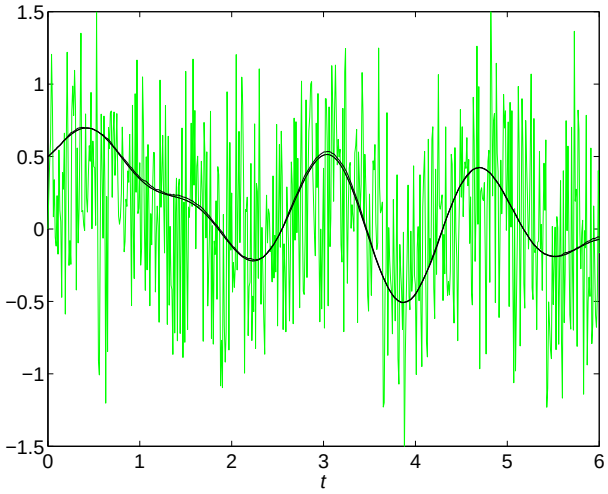

Figure 29: The comparison between $\bar{X}_n$ and X_n produced by the multiscale scheme with $p=4$ (black curves). Also shown is the fast process Y_{n,n_T+N} used in the micro-solver (grey curve).

where $\{z_m^{kj}\}$ are i.i.d with $\mathbb{P}\{z_m^{kj}=1/2\}=\mathbb{P}\{z_m^{kj}=-1/2\}=1/2$. High order schemes are discussed in [63]. For the initial condition, we take $Y_{0,0}=0$ and

$$Y_{n,0}=Y_{n-1,n_T+N-1}, \tag{7.11}$$

i.e. the initial values for the micro variables at macro-time-step n are chosen to be their final values from macro-time-step $n-1$. This choice of initial condition is not necessary for the convergence of the scheme, e.g.

$$Y_{n,0}=0 \tag{7.12}$$

would work as well, but it improves the convergence properties, as we will discuss in Section 9.2.3.

As an illustration, consider the following example with $(x,y)\in\mathbb{R}^2$:

$$\begin{cases} \dot{X}_t=-Y_t-Y_t^3+\cos(\pi t)+\sin(\sqrt{2}\pi t), & X_0=x, \\ \dot{Y}_t=-\dfrac{1}{\epsilon}(Y_t+Y_t^3-X_t)+\dfrac{1}{\sqrt{\epsilon}}\dot{W}_t, & Y_0=y. \end{cases} \tag{7.13}$$

From (7.7) the effective equation for $\bar{X}_t$ is

$$\dot{\bar{X}}_t=-\bar{X}_t+\cos(\pi t)+\sin(\sqrt{2}\pi t), \qquad \bar{X}_0=x. \tag{7.14}$$

We choose the following numerical parameters:

$$(T_0,\Delta t,\delta t/\varepsilon,n_T,M,N)=(6,\ 0.01,\ 0.01\times 2^{-p},\ 100,\ 1,\ 10\times 2^{3p}). \tag{7.15}$$

The results for $p=2$ is shown in Fig. 29, and compared with the solution of the effective equation for $\bar{X}_t$.

8 Exploring statistical self-similarity: An example without scale separation

8.1 General strategy for data estimation

In the problems discussed above, scale separation was very important for the efficiency of HMM: It allows us to choose small microscale simulation domain and still retain sufficient accuracy for the estimated data. It is important to realize that this is not the only situation for which HMM works efficiently. The underlying philosophy is more general and it works as follows. Suppose that the size of the macroscale mesh is H. We need to estimate some effective data such as transport coefficients at that scale, which is a function of H. Let us denote by $f=f(L)$ the value of that data at the scale L. If there is scale separation in the system, then $f(L)$ is essentially independent of L:

$$f(L)\approx \text{Const} \tag{8.1}$$

as long as L is much larger than some characteristic scale of the microscopic model, which might just be the correlation length. This allows us to take advantage of the scale separation by choosing the size of the microscale simulation domain, δ, to be much larger than the microscopic scale, but still much smaller than H. However, so long as the scale dependence of $f=f(L)$ is of a simple form with only few parameters, we can make use of this simple relationship by performing a few (not just one as was done for problems with scale separation) small scale simulations and use the results to predict the needed quantities at a much larger scale. One example of such a situation is when the system exhibits local self-similarity. In this case the dependence in (8.1) is of the form

$$f(L)=C_0L^{\beta}$$

with only two parameters. Therefore we can use results of microscopic simulations at two different scales to predict the result at a much larger scale, namely H.

This is a poor-man's version of the renormalization group method. Other examples of numerical methods that use renormalization ideas are found in [37,38].

8.2 Transport on a percolation network at criticality

This idea was demonstrated in [66] on the example of effective transport on a two-dimensional bond percolation network at the percolation threshold.

In the standard two dimensional bond percolation model with parameter p, $0\leq p\leq 1$, we start with a square lattice, each bond of the lattice is either kept with probability p or deleted with probability $1-p$. Of particular interest is the size of the percolation clusters formed by the remaining bonds in the network (see Fig. 30 for a sample of bond percolation). The critical value for this model is at $p=p^*=0.5$. For an infinite lattice, if $p<p^*$, the probability of having infinite size clusters is zero. For $p>p^*$, the probability

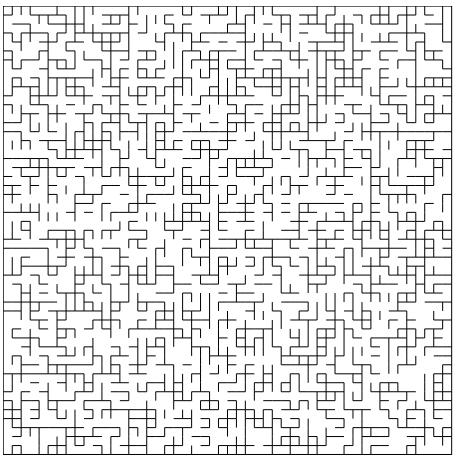

Figure 30: Bond percolation network on a square lattice at $p=0.5$.

of having infinite size clusters is 1. Given the parameter value p, the network has a characteristic length scale – the correlation length, denoted by ξ_p. As $p\to p^*$, ξ_p diverges as

$$\xi_p \sim |p-p^*|^\alpha, \tag{8.2}$$

where $\alpha=-4/3$ (see [152]). At $p=p^*$, $\xi_p=\infty$. In this case, the system has a continuum distribution of scales, i.e. it has clusters of all sizes. In the following we will consider the case when $p=p^*$.

We are interested in macroscopic transport on such a network. To study transport, say of some pollutants whose concentration density will be denoted by c, we embed this percolation model into a domain Ω in R^2. We denote by ε the bond length of the percolation model, and L the length scale for the domain Ω. We will consider the case when ε/L is very small.

The basic microscopic model is that of mass conservation. Denote by $S_{i,j}, i,j=1,\cdots,N$ the (i,j)-th site of the percolation network, and $c_{i,j}$ the concentration at that site. Define the fluxes

$$\begin{aligned}
\text{the flux from right} \quad & f^r_{i,j}=B^x_{i,j}(c_{i+1,j}-c_{i,j}),\\
\text{the flux from left} \quad & f^l_{i,j}=B^x_{i-1,j}(c_{i-1,j}-c_{i,j}),\\
\text{the flux from top} \quad & f^t_{i,j}=B^y_{i,j}(c_{i,j+1}-c_{i,j}),\\
\text{the flux from bottom} \quad & f^b_{i,j}=B^y_{i,j-1}(c_{i,j-1}-c_{i,j}).
\end{aligned}$$

Here the various B's are the bond conductivities for the specified bonds. The bond conductivity is zero if the corresponding bond is deleted, and 1 if the bond is retained. At each site $S_{i,j}$, from mass conservation, we have

$$f^t_{i,j}+f^b_{i,j}+f^r_{i,j}+f^l_{i,j}=0, \tag{8.3}$$

i.e. the total flux to this site is zero. This will be our microscale model.

For the macroscale solver, we choose a finite volume scheme over a macroscale grid Ω_H where H is the size of the finite volume cell (see Fig. 3). The data that need to be estimated from the microscale model, here the percolation model, are the fluxes at the mid-points of cell boundaries. Since the present problem is linear, we only need to estimate the effective conductivity for a network of size H. We note that at $p = p^*$, the effective conductivity is strongly size-dependent. In fact there are strong evidences that the following relation holds [89]:

$$\kappa_L = C_0 L^{\beta}, \tag{8.4}$$

where κ_L is the mean effective conductivity at size L. This is confirmed in Fig. 31 where we show a log-log plot of the effective conductivity as a function of scale.

Our basic strategy is to make use of such a relation to estimate the effective fluxes in the case when $\varepsilon \ll H$. For this purpose, we perform a series of local microscopic simulations on systems of size L_1 and L_2 where $\varepsilon \ll L_1 < L_2 \ll H$. From the results we estimate κ_{L_1} and κ_{L_2}. We then use these results to estimate the parameter values C_0, β in (8.4). Once we have these parameters, we can use (8.4) to predict κ_H.

One interesting question is the effect of statistical fluctuations. To see this we plot in Fig. 32 the actual and predicted (using self-similarity) values of the conductivity on a sub-lattice of size $L = 128$ for a number of realizations of the percolation network. The predicted values are computed using simulated values from sub-lattices with $L = 16$ and $L = 32$. The predicted values have obviously larger fluctuations than the actual values, implying that the fluctuations are amplified in the process of predicting the mean values. Nevertheless the mean values are predicted with reasonable accuracy, considering the relatively small size of the network.

More numerical results, including some results of the multiscale method, can be found in [66].

9 Error analysis

Error analysis for multiscale methods presents a new challenge to numerical analysis, particularly for problems involving multi-physics. Since multiscale methods are relatively new, and their errors typically involve several different contributions, rigorous results on error control are very much desired in order to help understanding basic issues such as stability and accuracy of multiscale methods. Indeed, to be able to develop a general strategy for error analysis was one of the main motivations for developing the HMM framework.

To begin with, what should we take as the exact or reference solution, to be compared with the numerical solution of a multiscale method? In general, we should not take the detailed solution of the microscopic problem as the reference solution, since approximating that would usually require solving the full microscopic problem, and therefore defeat

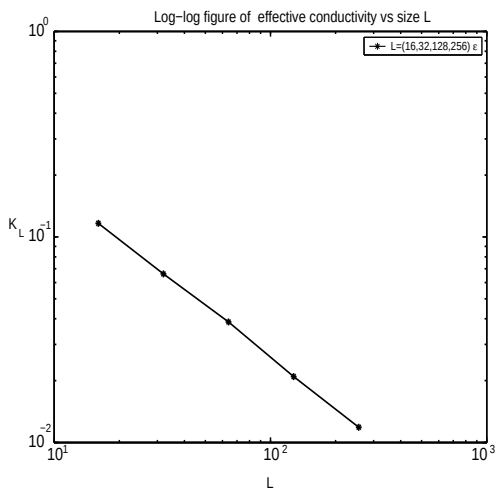

Figure 31: Effective conductivity at different scale $L=(16,32,64,128,256)\varepsilon$ for a realization of the percolation network with $p=p^*=0.5$.

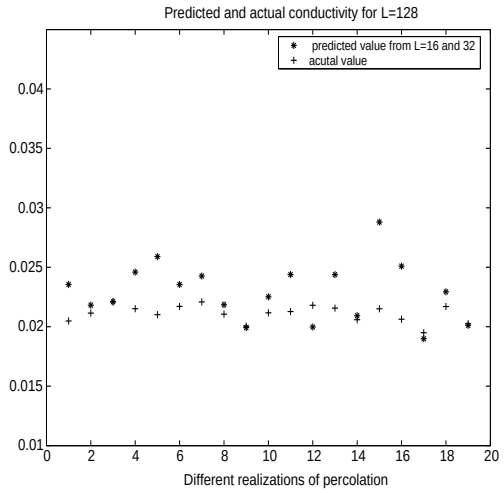

Figure 32: Effect of fluctuations: Actual and predicted effective conductivity at scale $L=128\varepsilon$ for different realizations of the percolation network with $p=0.5$. The predicted values are computed from $L=16\varepsilon$ and 32ε lattices assuming self-similarity.

the whole purpose. For type B problems, we can take the reference solution as the solution to the underlying macroscopic model, which we assume exist. Even though the details of the macroscopic model are not used in the numerical algorithm, the model can still be used for conceptual and analytical purposes. If we denote by u the solution to the microscopic model, U_0 the solution to the effective macroscale model, and Q the compression operator that maps the microscopic state to the macroscopic state, then by definition, U_0-Qu should be small. Therefore we can also take Qu as the reference solution. This is preferred since it comes directly out of the microscopic solution.

These issues have not been discussed much for other types of problems.

Since error analysis is much better understood for type B problems, we will focus our attention to this type of problems. The overall strategy is as follows. We first prove a general statement that if some underlying macroscopic scheme is stable, then the error in the HMM solution is bounded by the sum of two terms: The first is a standard error for the macroscopic solver; the second, sometimes denoted by $e(\mathrm{HMM})$, is a new term due to the errors in estimating the data. We then estimate this new term. The first step is usually quite general. Specific estimates in the second step are only obtained for specific models.

9.1 Error analysis of the HMM-FEM

Our first example is the HMM finite element method discussed earlier. We will always assume that $a^\varepsilon(\mathbf{x})$ is smooth, symmetric and uniformly elliptic:

$$\lambda I \le a^\varepsilon \le \Lambda I \tag{9.1}$$

for some $\lambda,\Lambda>0$ which are independent of ε. We will assume that the quadrature formula used in (3.3) is exact for polynomials of degree $2k-2$ for $k>1$ and k for $k=1$.

We will use standard notions for Sobolev spaces: $\|\cdot\|_1$ and $\|\cdot\|_0$ denote H^1 and L^2 norms respectively, and $\|\cdot\|_{1,\infty}$ denotes the $W^{1,\infty}$ norm.

As the first step, we will compare the HMM solution to the solutions of a macroscale model of the form:

$$\begin{cases} -\operatorname{div}\big(\mathcal{A}(\mathbf{x})\nabla U_0(\mathbf{x})\big) = f(\mathbf{x}), & \mathbf{x}\in D, \\ U_0(\mathbf{x}) = 0, & \mathbf{x}\in \partial D. \end{cases} \tag{9.2}$$

The following results are proved in [65].

Theorem 9.1. *Denote by U_0 and U_{HMM} the solution of* (9.2) *and the* HMM *solution, respectively. Let*

$$e(\mathrm{HMM}) = \max_{\substack{\mathbf{x}_\ell\in K \\ K\in\mathcal{T}_H}} \|\mathcal{A}(\mathbf{x}_\ell) - \mathcal{A}_H(\mathbf{x}_\ell)\|,$$

where $\|\cdot\|$ is the Euclidean norm. If U_0 is sufficiently smooth, then there exists a constant C independent of ε,δ and H, such that

$$\|U_0 - U_{\mathrm{HMM}}\|_1 \le C\big(H^k + e(\mathrm{HMM})\big), \tag{9.3}$$

$$\|U_0 - U_{\mathrm{HMM}}\|_0 \le C\big(H^{k+1} + e(\mathrm{HMM})\big). \tag{9.4}$$

In addition, there exit constants C_0 and H_0 such that if $e(\mathrm{HMM})|\ln H|<C_0$, then for all $H\le H_0$,

$$\|U_0 - U_{\mathrm{HMM}}\|_{1,\infty} \le C\big(H^k + e(\mathrm{HMM})\big)|\ln H|. \tag{9.5}$$

So far no assumption on the form of $a^\varepsilon(\mathbf{x})$ or $\mathcal{A}(\mathbf{x})$ is necessary. U_0 can be the solution of an arbitrary macroscopic equation with the same right-hand side as in (2.17). Of course for U_{HMM} to converge to U_0, i.e., $e(\mathrm{HMM})\to 0$, U_0 must be chosen as the solution of the homogenized equation, which we now assume exists. To obtain quantitative estimates on $e(\mathrm{HMM})$, we must restrict ourselves to more specific situations.

The simplest example of such a specific problem is when

$$a^\varepsilon(\mathbf{x}) = a\Big(\mathbf{x}, \frac{\mathbf{x}}{\varepsilon}\Big), \tag{9.6}$$

where $a(\mathbf{x},\mathbf{y})$ is either periodic in $\mathbf{y}$, in which case we assume the period to be $I=[-1/2,1/2]^d$, or random but stationary under shifts in $\mathbf{y}$, for each fixed $\mathbf{x}\in D$. In both cases, it has been shown that [18,129]

$$\|u^\varepsilon(\mathbf{x}) - U_0(\mathbf{x})\|_0 \to 0, \tag{9.7}$$

where $U_0(\mathbf{x})$ is the solution of the homogenized equation. The homogenized equation takes the form of (9.2) with coefficients computed from solving the cell problems [18,129].

For the following results we assume that the periodic boundary condition is used for the microscale problems in HMM.

Theorem 9.2. *For the periodic homogenization problem, we have*

$$e(\mathrm{HMM}) \leq \begin{cases} C\varepsilon, & \text{if } I_\delta(\mathbf{x}_\ell) = \mathbf{x}_\ell + \varepsilon I, \\ C\left(\frac{\varepsilon}{\delta} + \delta\right), & \text{otherwise.} \end{cases}$$

The difference between the two results lies in the choice of $I_\delta(\mathbf{x}_\ell)$. For the second result we do not need to assume that the period of $a(\mathbf{x},\cdot)$ is a cube: In fact it can be of arbitrary shape as long as its translations tile up the whole space.

Another important case for which specific estimates on $e(\mathrm{HMM})$ have been obtained is the random homogenization problem. However the results for this case are less satisfactory. The following result was proved in [65] following the work of [189]. Here we assume for simplicity that the coefficient $a(\mathbf{x},\mathbf{y},\omega)$ is independent of $\mathbf{x}$.

Theorem 9.3. *For the random homogenization problem, assuming that a mixing condition holds. We have*

$$\mathbb{E}e(\mathrm{HMM}) \leq \begin{cases} C(\kappa)\left(\frac{\varepsilon}{\delta}\right)^{\kappa}, & d=3, \\ \textit{remains open}, & d=2, \\ C\left(\frac{\varepsilon}{\delta}\right)^{1/2}, & d=1, \end{cases}$$

where

$$\kappa = \frac{6-12\gamma}{25-8\gamma},$$

for any $0<\gamma<1/2$. *By choosing* γ *small,* κ *can be arbitrarily close to* $6/25$. *Here* $\mathbb{E}$ *denotes expectation with respect to the probability space for the random coefficients.*

The proper probabilistic set-up is discussed in [129]. The mixing condition is stated in [65]. Roughly speaking it says that the correlation of the random coefficients $a(\mathbf{y},\omega)$ decays exponentially fast at large distances.

U_{HMM} by itself does not give any information on the gradients of u^ε which is important for many applications since it is related to physically important quantities such as stress in the elastic problem and velocity in the porous medium problem. This information can be recovered using a simple post-processing technique. For the general case, having U_{HMM}, one can obtain locally the microstructural information using an idea in [126]. Assume that we are interested in recovering u^ε and ∇u^ε only in the subdomain $\Omega \subset D$. Consider the following auxiliary problem:

$$\begin{cases} -\mathrm{div}\left(a^\varepsilon(\mathbf{x})\nabla\tilde{u}^\varepsilon(\mathbf{x})\right) = f(\mathbf{x}), & \mathbf{x}\in\Omega_\eta, \\ \tilde{u}^\varepsilon(\mathbf{x}) = U_{\mathrm{HMM}}(\mathbf{x}), & \mathbf{x}\in\partial\Omega_\eta, \end{cases} \tag{9.8}$$

where Ω_η satisfies $\Omega \subset \Omega_\eta \subset D$ and $\text{dist}(\partial\Omega, \partial\Omega_\eta) = \eta$. We then have: There exists a constant C such that

$$\left(\int\!\!\!\!\!\!- _{\Omega} |\nabla(u^\varepsilon - \tilde{u}^\varepsilon)|^2 \mathbf{x} \right)^{1/2} \leq \frac{C}{\eta} \|u^\varepsilon - U_{\text{HMM}}\|_{L^\infty(\Omega_\eta)}. \tag{9.9}$$

There is a much simpler procedure for the periodic homogenization problem [55]. Consider the case when $k=1$ and choose $I_\delta = \mathbf{x}_K + \varepsilon I$, where $\mathbf{x}_K$ is the barycenter of K. We also assume that the quadrature point in the element K is at $\mathbf{x}_K$. Define $\tilde{u}^\varepsilon$ by:

1. $\tilde{u}^\varepsilon|_{I_\delta} = v_K^\varepsilon$, where v_K^ε is the solution of (3.4) with the boundary condition that $v_K^\varepsilon - U_{\text{HMM}}$ is periodic with period εI and $\int_{I_\delta} (\tilde{u}^\varepsilon - U_{\text{HMM}})(\mathbf{x}) d\mathbf{x} = 0$.
2. $(\tilde{u}^\varepsilon - U_{\text{HMM}})|_K$ is periodic with period εI.

We then have [65]

Theorem 9.4. *Let $\tilde{u}^\varepsilon$ be defined as above. Then*

$$\left(\sum_{K \in \mathcal{T}_H} \|\nabla(u^\varepsilon - \tilde{u}^\varepsilon)\|_{0,K}^2 \right)^{1/2} \leq C\left(\sqrt{\varepsilon} + H\right). \tag{9.10}$$

Similar results are also proved for nonlinear elliptic problems. For details, see [65].

[188] presents systematic numerical studies on the effect of the boundary conditions for the microscale problems as well as the microscale cell size.

9.2 Dynamic problems

The main strategy proposed in [56] is to compare the HMM solution with that of an underlying macroscale solver, or an effective macroscale method. The basic result, proved in [56], is that if this effective macroscale method is stable and k-th order accurate, then

$$||U_{\text{HMM}} - U_0|| \leq ||U_{\text{HMM}} - \bar{U}_H|| + ||\bar{U}_H - U_0|| \leq C(e(\text{HMM}) + (\Delta t)^k), \tag{9.11}$$

where U_0 is the solution of the macroscale model, $e(\text{HMM})$ is the error in the estimated effective force. In proving (9.11), it is assumed that both HMM and the effective macroscale method are expressed in the form:

$$U^{n+1} = U^n + \Delta t F^\varepsilon(U), \tag{9.12}$$

$$\bar{U}^{n+1} = \bar{U}^n + \Delta t \bar{F}(\bar{U}), \tag{9.13}$$

and $e(\text{HMM})$ is defined as

$$e(\text{HMM}) = \max_U \|\bar{F}(U) - F^\varepsilon(U)\|. \tag{9.14}$$

We also have:

$$||Qu^\varepsilon - U_{\rm HMM}|| \le ||Qu^\varepsilon - U_0|| + ||\bar{U}_H - U_0|| + ||U_{\rm HMM} - \bar{U}_H||. \tag{9.15}$$

Here the first term on the right-hand side is due to the error in the effective model; the second term is due to the error in the macroscale solver; the third term is the HMM error. Denote by ε the parameter that characterizes the small scale in the problem. (9.15) suggests an estimate of the type:

$$||Qu^\varepsilon - U_0|| \le C(\varepsilon^\alpha + (\Delta t)^k + e(\text{HMM})). \tag{9.16}$$

We now apply this general result to some concrete examples.

9.2.1 ODEs with multiple time scales

The problems and algorithms were discussed in Section 2.2.1. If we apply the general principles discussed above, we get:

Theorem 9.5. *HMM is stable if the macroscale solver is stable. Moreover for any given constant T there exists a constant C such that*

$$|E^n| \le C((\Delta t)^k + e(HMM))$$

if $n\Delta t \le T$, where E^n is the error between the HMM solution and the slow component of the exact solution (a precise definition is given below), k is the order of the macroscale solver, $e(HMM)$ is the error in the estimation of the macroscale data.

Next we estimate $e(\text{HMM})$. This depends on a number of important factors in HMM, in particular the filter K. We first discuss the case of dissipative systems and consider for simplicity the example in (2.4). We will further assume that f and g are smooth and bounded, and that $\{Z^{n,0}\}$ is bounded.

In the limit as $\varepsilon \to 0$, one expects that x will be close to $f(y)$, and hence the effective dynamics for the slow variable y is given by

$$\dot{\bar{y}} = g(f(\bar{y}), \bar{y}) = G(\bar{y}). \tag{9.17}$$

In fact, we can easily prove the following: If we denote by $(x_\varepsilon, y_\varepsilon)$ the solution of (2.4) and if $y_\varepsilon(0) = \bar{y}(0)$, then

$$|y_\varepsilon(t) - y_0(t)| \le C_1 \exp\left(-\frac{t}{\varepsilon}\right) + C_2\varepsilon.$$

Let us first consider the case when the macroscale solver is forward Euler. In this case we can express HMM as:

$$y^{n+1} = y^n + \Delta t \tilde{g}(y^n).$$

Let $E^n = y^n - y_0(t^n)$, where $t^n = n\Delta t$, for $n\Delta t \le T$. We have

$$\begin{aligned}\frac{E^{n+1}-E^n}{\Delta t} &= \tilde{g}(y^n) - G(y_0(t^n)) + \mathcal{O}(\Delta t)\\ &= G(y^n) - G(y_0(t^n)) + \tilde{g}(y^n) - G(y^n) + \mathcal{O}(\Delta t)\\ &= G'(y_0(t^n) + \theta E^n)E^n + \tilde{g}(y^n) - G(y^n) + \mathcal{O}(\Delta t).\end{aligned}$$

If we let $L = \max|G'(y)|$, then we get

$$|E^n| \le e^{Lt}(C\Delta t + \max_{n\Delta t \le T}|\tilde{g}(y^n) - G(y^n)|),$$

where $C = \max_{t\le T}|y_0''(t)|$. Here the first term on the right-hand side is the standard truncation error at the macroscale. The second term $|\tilde{g}(y^n) - G(y^n)|$ is what we usually call $e(\mathrm{HMM})$. With (2.10), it is a simple matter to prove [53]:

$$e(\mathrm{HMM}) \le C\left(\Delta t + |1 - \delta t/\varepsilon|^N\right). \tag{9.18}$$

In the general case when k-th order stable macroscale solvers are used, we have [53]:

Theorem 9.6. *Assume that the macroscale solver is k-th order accurate and stable, i.e. for linear multi-step methods the root condition is satisfied. Let $A(\lambda\delta t)$ be the amplification factor of the microscale solver for the ODE $\dot{y} = -\lambda y$. Then there exists a constant C, independent of $\Delta t, \varepsilon, \delta t$ and N, such that, for $n\Delta t \le T$,*

$$|E^n| \le C\left(\Delta t^k + |A(\delta t/\varepsilon)|^N\right).$$

Next we consider the oscillatory case. As before we will discuss a simple and yet canonical example, namely (2.5). The dynamics for the slow variable I obeys the equation

$$\dot{\bar{I}} = \frac{1}{2\pi}\int_0^{2\pi} g(\varphi, \bar{I})d\varphi = G(\bar{I}). \tag{9.19}$$

See for example [11]. We will assume that $\omega(I)$ never vanishes:

$$\omega(I) \ge \omega_0 > 0. \tag{9.20}$$

We will restrict ourselves to the situation when the weights $\{K_{m,N}\}$ are of the form

$$K_{m,N} = K_0\left(1 - \frac{m}{N}\right) \tag{9.21}$$

for $m = 0, 1, \ldots, N$, where K_0 is a filtering kernel.

A crucial component in the analysis in this case is the effect of the kernel K_0. This is examined in detail in [69]. Consider an example for which the microscopic data takes the form:

$$f^\varepsilon(t) = f_0(t) + f_1\left(\frac{t}{\varepsilon}\right),$$

where $f_1(\tau)$ is periodic in τ with period 1. The macroscale component of $\{f^\varepsilon(t)\}$ is

$$F(t)=f_0(t)+\int_0^1 f_1(\tau)d\tau.$$

The macroscale data of interest is $F_0=F(0)$. Assume that the F-estimator has the form

$$\tilde{F}_0=\frac{1}{T}\int_0^T K_0\left(1-\frac{\tau}{T}\right)f^\varepsilon(\tau)d\tau.$$

Then we have:

Lemma 9.1. *Assume that K_0 satisfies the following conditions*

1. (A1). *Moment condition*

$$\int_0^1 K_0(\tau)d\tau=1,\quad \int_0^1(1-\tau)^\alpha K_0(\tau)d\tau=0$$

for $\alpha=1,2,\ldots\ell-1$.

2. (A2). *Regularity condition*

$$K_0^{(\alpha)}(0)=K_0^{(\alpha)}(1)=0$$

for $\alpha=0,1,\ldots,q-1$ and

$$\int_0^1|K_0^{(\alpha)}(\tau)|\alpha\tau<+\infty$$

for $\alpha=0,1,\ldots,q$.

Then

$$|F_0-\tilde{F}_0|\le C\left(T^\ell+\left(\frac{\varepsilon}{T}\right)^q\right).$$

Using this result, we obtain:

Theorem 9.7. *Under the same assumption as before, we have*

$$|E^n|\le C\left((\Delta t)^k+\left(\frac{\delta t}{\varepsilon}\right)^r+\left(\frac{\varepsilon}{N\delta t}\right)^q\right),$$

where $r=\min(l,p)$ and p is the order of the microscale solver.

As expected, the size of δt should be chosen to resolve the small time scale ε, and N should be large enough so that $N\delta t$ is larger than ε in order to sample adequately the dynamics at the small scale.

9.2.2 The effect of the fast variable reinitialization

The error estimates given in the last subsection were for the general case when the initialization of the fast variables in the microscale solver is quite arbitrary. Suitable reinitialization of the fast variables at each macro-time-step may result in significant gain in efficiency. Precise estimates are given below for the case of stochastic ODEs, but it is useful to first illustrate the influence of fast variables initialization on a simple example (2.4).

Suppose that the initial condition for (2.9) is taken to be $x^{n,0}=0$. Then N must be taken large enough so that (2.9) has converged to sufficient accuracy, i.e. $x^{n,N}\approx f(y^n)$, and the error estimate for $e(\text{HMM})$ is given in (9.18).

Suppose on the contrary that we take $x^{n,0}=x^{n-1,N}$. Then it can be shown that the error estimate improves to

$$e(\text{HMM})\leq C\left(\Delta t+\frac{\varepsilon\Delta t}{N\delta t}+\Delta t\left|1-\frac{\delta t}{\varepsilon}\right|^N\right), \tag{9.22}$$

which indicates, in particular, that the scheme converges as $\Delta t,\delta t\to 0$ provided that $\varepsilon\Delta t/N\delta t\to 0$. Notice that this can happen even if $N=1$. Notice also that accuracy requires that

$$\varepsilon\Delta t/N\delta t\ll 1,$$

whereas gaining in efficiency in the sense of (1.1) requires

$$\Delta t/N\delta t\gg 1.$$

For small ε both constraints can be satisfied at the same time.

The simplest way to justify (9.22) is to re-write (2.9) as

$$x^{n,m+1}=x^{n,m}-\frac{1}{\gamma}\frac{\Delta t}{N}(x^{n,m}-f(y^n)), \tag{9.23}$$

where

$$\gamma=\frac{\varepsilon\Delta t}{N\delta t}. \tag{9.24}$$

It is easy to see that in the limit as δt, $\Delta t\to 0$ with γ kept fixed, HMM is consistent with the modified equation

$$\begin{cases}\dot{x}=-\dfrac{1}{\gamma}(x-f(y)),\\ \dot{y}=g(x,y).\end{cases} \tag{9.25}$$

If $\gamma\gg\varepsilon$, this equation is less stiff than (2.4) and correspondingly HMM gains in efficiency over a direct scheme for (2.4). On the other hand, for $\varepsilon\ll 1$ it is possible to also satisfy $1\gg\gamma\gg\varepsilon$. In this case, the y component of the solutions of (2.4) and (9.25) remains close because of the existence of a limiting dynamics. But the choice of γ is now dictated by the error tolerance and not by the value of ε in the original equation.

9.2.3 Stochastic ODEs with multiple time scales

Here we discuss some of the results proved in [63] for stochastic ODEs. The algorithms were described in Section 7. Again we will focus on the case of advective time scale. Diffusion time scale was considered in [63].

We will make the following assumptions:

1. The coefficients a, b and σ, viewed as functions of (x,y,ε), are in $\mathbb{C}_b^\infty$, a and σ are bounded. Here $\mathbb{C}_b^\infty$ is the space of smooth functions with bounded derivatives of any order.
2. There exists an $\alpha>0$ such that $\forall\ (x,y,\varepsilon)$,
$$|\sigma^T(x,y,\varepsilon)y|^2\geq\alpha|y|^2.$$
3. There exists a $\beta>0$ such that $\forall\ (x,y_1,y_2,\varepsilon)$,
$$\langle(y_1-y_2),(b(x,y_1,\varepsilon)-b(x,y_2,\varepsilon))\rangle+\|\sigma(x,y_1,\varepsilon)-\sigma(x,y_2,\varepsilon)\|^2\leq-\beta|y_1-y_2|^2,$$
where $\|\cdot\|$ denotes the Frobenius norm.

Under these assumptions, we have:

Theorem 9.8. *Assume that the macro solver is stable and k-th order accurate for* (7.7)*. Then for any $T_0>0$, there exists a constant $C>0$, independent of $(\epsilon,\ \Delta t,\ \delta t,\ n_T,\ M,\ N)$, such that*

$$\sup_{n\leq T_0/\Delta t}\mathbb{E}|X^\epsilon_{t_n}-X_n|\leq C\left(\sqrt{\epsilon}+(\Delta t)^k+e_D\right), \tag{9.26}$$

where $t_n=n\Delta t$, and

$$e_D=(\delta t/\varepsilon)^\ell+\frac{e^{-\frac{1}{2}\beta n_T(\delta t/\varepsilon)}}{\sqrt{N(\delta t/\varepsilon)+1}}(R+\sqrt{R})+\frac{\sqrt{\Delta t}}{\sqrt{M(N(\delta t/\varepsilon)+1)}}. \tag{9.27}$$

Here ℓ is the weak order of the micro solver,

$$R=\frac{\Delta t}{1-e^{-\frac{1}{2}\beta(n_T+N-1)(\delta t/\varepsilon)}}, \tag{9.28}$$

if the fast variable is initialized as in (7.11) *and $R=1$ if the fast variable is initialized as in* (7.12)*.*

The basic idea for proving this result is as follows. The error $|X^\epsilon_{t_n}-X_n|$ in (9.26) is decomposed into three parts:

1. $|X^\epsilon_t-\bar{X}_t|$, where $\bar{X}_t$ is the solution of the effective equation (7.7).
2. $|\bar{X}_{t_n}-\bar{X}_n|$, where $\bar{X}_n$ is the approximation of $\bar{X}_{t_n}$ given by the selected macro solver assuming that $\bar{a}(x)$ is known.
3. $|\bar{X}_n-X_n|$.

The first part is the error in the averaging principle itself. As shown in [63], we have

$$\sup_{0\le t\le T_0} \mathbb{E}|X_t^\epsilon - \bar{X}_t| \le C\sqrt{\epsilon}.$$

This is the first term in (9.26). The second part is a standard ODE estimate:

$$\sup_{n\le T_0/\Delta t} |\bar{X}_{t_n} - \bar{X}_n| \le C(\Delta t)^k. \tag{9.29}$$

This is the second term in (9.26). The third part, e_D, accounts for the error caused by using $\tilde{a}_n$ instead of $\bar{a}(X_n)$ in the macro solver. Here the term $(\delta t/\varepsilon)^\ell$ is due to the micro-time discretization which induces a difference between the invariant measures of the continuous and discrete dynamical systems. The term

$$\frac{e^{-\frac{1}{2}\beta n_T(\delta t/\varepsilon)}}{\sqrt{N(\delta t/\varepsilon)+1}}(R+\sqrt{R})$$

accounts for the errors caused by relaxation of the fast variables. The factor R reflects the influence of the particular initialization procedure used for the fast variables at each macro time step. Different initialization leads to similar estimates but with different values of R. For example if we use $Y_{n,0}=0$, then $R=1$. Finally, the term

$$\frac{\sqrt{\Delta t}}{\sqrt{M(N(\delta t/\varepsilon)+1)}}$$

accounts for the sampling errors after the fast variable reaches local equilibrium. This is a central limit theorem type of estimate.

The estimate (9.26) suggests a somewhat surprising fact, namely that the HMM scheme converges as $\Delta t\to 0$, $\delta t\to 0$ on any sequence such that $R\to 0$, even if we take only one realization and one micro time step per macro time step, $M=1$, $n_T=1$, $N=1$. In this case $R=\Delta t/(\delta t/\varepsilon)$ to leading order. This is the consequence of the particular re-initialization procedure that we have adopted (see (7.11)), and it is a manifestation of the point made in the last subsection.

We now discuss how these results play out in actual computations. We will adopt the more accurate initialization procedure for the fast variable. When

$$N_m(\delta t/\varepsilon) = (n_T+N-1)(\delta t/\varepsilon) > 1,$$

we have $R=\Delta t$ plus higher order terms, and

$$\sup_{n\le T_0/\Delta t} \mathbb{E}|X_n - \bar{X}_n| \le C\left((\delta t/\varepsilon)^\ell + \frac{e^{-\frac{1}{2}\beta n_T(\delta t/\varepsilon)}\sqrt{\Delta t}}{\sqrt{N(\delta t/\varepsilon)+1}} + \frac{\sqrt{\Delta t}}{\sqrt{M(N(\delta t/\varepsilon)+1)}}\right). \tag{9.30}$$

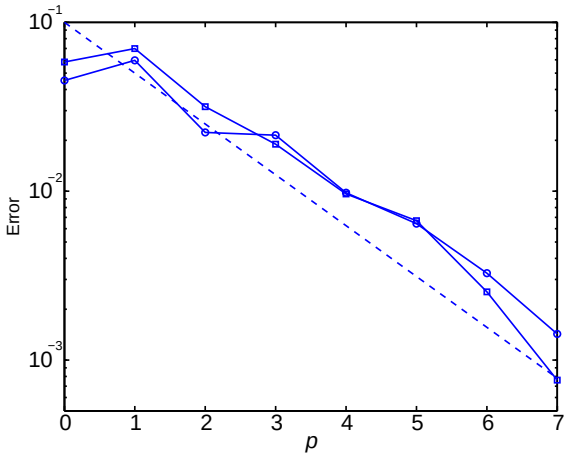

Figure 33: The error $E_p^\ell = (\Delta t/T_0)\sum_{n\le\lfloor T_0/\Delta t\rfloor}|\tilde{X}_n - \bar{X}_n|$ as a function of p when $\ell=1$ (circles) and $\ell=2$ (squares). Also shown is the predicted estimated, 0.1×2^{-p} (dashed line).

Table 3: The computed values for the error E_p^ℓ.

	$p=0$	$p=1$	$p=2$	$p=3$	$p=4$	$p=5$	$p=6$	$p=7$
$\ell=1$	.058	.070	.032	.019	.0096	.0067	.0025	.00076
$\ell=2$	.045	.059	.022	.021	.0098	.0064	.0033	.0014

Here Δt is taken as a fixed parameter. Suppose that we want to bound the error by $\mathcal{O}(2^{-p})$ for $p=0,1,\ldots$ and assume that $M=1$. Then as in [63], we find that the optimal parameters are

$$\delta t/\varepsilon = \mathcal{O}(2^{-p/\ell}), \qquad n_T = \mathcal{O}(1), \qquad N = \mathcal{O}(2^{p(2+1/\ell)}),$$

which gives

$$\text{cost} = \frac{n_T+N-1}{\Delta t} = \mathcal{O}(2^{p(2+1/\ell)})$$

independent of ε. The magnitudes of the errors for various p and $\ell=1,2$ are listed in the following table and shown in Fig. 33. As predicted, we the error scales as $E\ell_p = \mathcal{O}(2^{-\ell p})$.

9.2.4 Other examples

We briefly mention a few other examples that have been analyzed. The parabolic homogenization problem has been analyzed in [3, 55, 120]. The structure of the analysis is very similar to the examples discussed here. In particular, [120] gives results that are similar to the ones discussed here for the elliptic homogenization problem. Error analysis and careful numerical studies for the hyperbolic homogenization problem were presented in [33, 34].

Examples with discrete microscale models were considered in [61]. The discrete models can be molecular dynamics or kinetic Monte Carlo methods. The macroscale model

considered in [61] was gas dynamics or general nonlinear conservation laws. It is proven in [61] that the $e(\mathrm{HMM})$ error consists of three parts: the relaxation error, the error due to the finite size of the simulation domain for the micro model, and the sampling error. Clearly as the system size increases, the finite size effect decreases but the relaxation error increases. Therefore this result gives some suggestions on how to choose the size of the microscale simulation domain. Unfortunately there are very few explicit results on the dependence of these errors on the domain size. All known results are proved for lattice models. We refer to [61] for a discussion on this issue.

10 Limitations of HMM

As was discussed in [56], there are problems for which HMM does not work well. One class of such problems are problems for which the time history of the detailed microstructural behavior has to be parametrized in order to determine the macroscale properties. One such example is the homogenization problem for the Carleman model, discussed in [56]. Consider the Carlman equation with multiscale initial data:

$$\begin{aligned}
&\frac{\partial u}{\partial t}+\frac{\partial u}{\partial x}=v^2-u^2,\\
&\frac{\partial v}{\partial t}-\frac{\partial v}{\partial x}=u^2-v^2,\\
&u(x,0)=a(x,x/\varepsilon),\\
&v(x,0)=b(x,x/\varepsilon),
\end{aligned} \tag{10.1}$$

where $a(x,y),b(x,y)$ are assumed to be smooth and 1-periodic in y. The homogenized equation for this problem is given by [170]:

$$\begin{aligned}
&\frac{\partial \tilde{u}}{\partial t}+\frac{\partial \tilde{u}}{\partial x}=\int_0^1 \tilde{v}(x,y,t)^2dy-\tilde{u}^2,\\
&\frac{\partial \tilde{v}}{\partial t}-\frac{\partial \tilde{v}}{\partial x}=\int_0^1 \tilde{u}(x,y,t)^2dy-\tilde{v}^2,\\
&\tilde{u}(x,y,0)=a(x,y),\\
&\tilde{v}(x,y,0)=b(x,y).
\end{aligned} \tag{10.2}$$

Tartar proved [170]:

$$\lim_{\varepsilon\to 0}\left(\left|u(x,t)-\tilde{u}\left(x,\frac{x-t}{\varepsilon},t\right)\right|+\left|v(x,t)-\tilde{v}\left(x,\frac{x+t}{\varepsilon},t\right)\right|\right)=0.$$

Here the natural macroscale variables U are the weak limits of the full microscale solutions:

$$U(x,t)=\int_0^1 \tilde{u}(x,y,t)dy=\lim_{\delta\to 0}\left(\lim_{\varepsilon\to 0}\int K_\delta(x-z)u(z,t)dz\right),$$
$$V(x,t)=\int_0^1 \tilde{v}(x,y,t)dy=\lim_{\delta\to 0}\left(\lim_{\varepsilon\to 0}\int K_\delta(x-z)v(z,t)dz\right),$$

where K_δ is some kernel compactly supported in $(-\delta,\delta)$ with,

$$\int_{-\delta}^{\delta} K_\delta(x)dx=1.$$

However for this problem, there is no time scale separation between the dynamics of (U,V) and the remaining components of (u,v), such as higher order moments. In fact, to obtain information on (U,V), one has to keep track of the dynamics of the microstructure. Therefore a blind application of HMM will give wrong results.

As was shown in [67], this particular problem can be effectively treated using a combination of the particle method and a proper sampling procedure for the microstructure.

A second example with a very similar feature is the transport equation with oscillatory velocity fields

$$\partial_t u+\partial_{x_1}\left(a\left(\frac{x_2}{\varepsilon}\right)u\right)=0. \tag{10.3}$$

The homogenized equation for this problem is [170]

$$\partial_t U+\bar{a}\partial_{x_1}U=\partial_{x_1}^2\int_{-\alpha}^{\alpha} d\omega(\gamma)\int_0^t dsU(x_1+\gamma(t-s),x_2,s) \tag{10.4}$$

and it shows memory dependence. Here ω is some kernel that depends on a, $\bar{a}$ is the average of a over its period. We refer to [55] for discussions of this example.

Both examples can be treated by the fiber bundle idea discussed earlier. For the example of Carleman equation, we can view the *y-space* as being the fiber. Same can be said about the linear transport equation. One can then design numerical methods based on the idea of evolving the microstructure over the fiber. An application of this idea is presented in [187] for the transport equation.

Another limitation of HMM concerns with the a priori assumption on the constitutive relation, which is reflected in the constraints on the microscale solver. A crucial advantage of HMM is that it does not need the full knowledge of the macroscale model. But some knowledge about the macroscale model *is important*, as we now illustrate.

Consider the problem

$$\partial_t u+\nabla\cdot\left(b\left(\frac{x}{\varepsilon}\right)u\right)=\nabla\cdot\left(a\left(\frac{x}{\varepsilon}\right)\nabla u\right), \tag{10.5}$$

where b and a are smooth periodic functions with period 1. The homogenized equation for (10.5) is given by

$$\partial_t U+\nabla\cdot(\bar{b}U)=\nabla\cdot(A\nabla U), \tag{10.6}$$

where A is the homogenized coefficient for the case when $b = 0$, $\bar{b}$ is the average of b over its period. Without knowing that the effective macroscale flux should depend on the derivative of the macroscale variable U, we might use HMM as in Section 2.2.2, and impose as constraints over the microscale solver only that the average of u be the same as the local value of the macroscale variable U. This results in an $\mathcal{O}(1)$ error for the macroscale quantities since it completely neglects the diffusive flux.

The failure in this case is due to the fact that in constructing the constrained microscale solver, we implicitly made the wrong constitutive assumption that the macroscale flux depends only on U, not the higher order derivatives of U. This is easily fixed by the methods described in Section 2.2.2. But it shows that some knowledge about the macroscale model is crucial for designing the right HMM.

11 Conclusions and new directions

11.1 General procedures and main features of HMM

In summary, the main steps in developing an HMM style of multiscale method are as follows:

1. Identify the macroscale variables, and the macroscale structure of the problem, such as variational structure, conservation laws, diffusion processes, etc.
2. Express the microscale model in the form that is consistent with the identified macroscale structure. In our examples for fluids and solids, this step involves deriving the conservation laws from MD, and expressing the fluxes, such as stress, in atomistic variables. This is the basis for connecting the macroscale and microscale models.
3. Select the macroscale solver, and identify the data that need to be estimated from the microscale solver.
4. Design the constrained microscale solver that gives the needed data. Technically this is often the most difficult step, and is subject to continuous improvement. One should exploit as much as possible any special features that the problem has, in order to maximize efficiency.
5. Process the data from the microscale solver in order to extract the macroscale data needed in the macroscale solver.

HMM is a top-down framework: It is based on the macroscopic solver and uses the microscale model as a supplement. Its two-component procedure offers a number of interesting features, including:

1. The ability to make maximum use of our knowledge on all scales. For example, when choosing the macroscale solver, we may take advantage of what is known at the macroscale, such as conservation form, variational structure, etc, as well as the nature of the physical process such as shock formation, phase transformation.

2. The ability to make maximum use of the special features of the problem. This is already demonstrated by the examples discussed above. The disparity between macro and micro time scales, for example, is made use of by the fact that satisfactory approximation for the needed macro data can be obtained by carrying out the microscale solver on relatively short time intervals.

We have seen that the framework of HMM provides useful guidance for systematically designing multiscale methods in a wide variety of applications. It also provides a natural setting for carrying out mathematical analysis of multiscale algorithms.

Despite its success, there are still many more interesting possibilities that have yet to be explored. We will end this review with a discussion of some of the directions for further work.

11.2 Algorithm development

From the viewpoint of algorithms, the two most important aspects are:

1. Adaptivity.
2. Data processing techniques.

Adaptivity is important for many applications, and HMM offers new possibilities for adaptive algorithm. The two most obvious places where adaptive algorithms are needed are: (1). Adaptively decide whether the empirical macroscale model is accurate enough or whether the microscale model is needed to supply the data. This is crucial to any adaptive model refinement algorithms. What is needed is some local error indicators such as the error estimators in adaptive finite element method. Some work in this direction has been done recently by Tinsley Oden and coworkers. (2). Adaptively decide the duration and size of the domain over which the microscale simulation is carried out in order to estimate the data.

There is also the possibilities to incorporate the ideas of learning into HMM, or any other current coupling schemes: As the simulation proceeds, the accumulated data from the microscale simulations can be used to build a database, the database can then be used to reduce the complexity of further computation. An example of using such a strategy, which was called "semi-empirical methods", was given in [56] for the linear parabolic homogenization problem. There it is known that the averaged fluxes are linear functions of the macroscopic gradient. Therefore one only has to determine the coefficients of these linear relations using a few data points obtained from the HMM procedure. This procedure should be explored in more general situations.

A more ambitious adaptive procedure is to determine adaptively the correct macroscale variable and the form of the macroscale model from carefully designed microscopic experiments. This is an attractive possibility and there are obvious ideas to try, but so far there are little concrete results in this direction.

The second important aspect of algorithmic development is data processing. Efficient data processing techniques can increase the accuracy of HMM and reduce the complexity

by reducing the size of the computational domain which over which microscale models are solved. One key factor that directly influences the efficiency of the HMM procedure is the signal to noise ratio in the microscale simulation. The high order accurate kernels that satisfy the high order moment and regularity conditions discussed in Section 9.2.1 seem to be most useful for data that have specific structure such as periodicity. Most data obtained from microscopic simulations are quite stochastic and lack such structure. It is important to develop more advanced techniques for analyzing such data. The most obvious suggestion is to use wavelets. But even this has not been explored.

11.3 Analytical issues

The most pressing analytical issue at the present time is the analysis of HMM for type A problems. The difficulty is associated with the fact that for type A problems, it often requires fundamental understanding about the properties of the defects in order to carry out some analysis, and currently there are very few examples for which this has been done.

There are still many issues remaining as far as type B problems are concerned. Estimating accurately $e(\mathrm{HMM})$ often requires understanding quantitatively the rate of convergence of various systems in the thermodynamic limit, as well as the behavior of the relaxation times as a function of the microscopic system size. Again there are very few analytical results in this area, particularly for systems described by molecular dynamics and quantum mechanics (see the discussion in [61]). But even for homogenization problems, our understanding of these issues are quite unsatisfactory. Careful numerical studies can help to clarify these issues as well as suggest the right form of analytical results (see for example [61, 145]).

Acknowledgments

In writing this review, we have drawn material from the work of many of our collaborators, including Assyr Abdulle, Li-Tien Cheng, Ibrahim Fatkullin, Tiejun Li, Di Liu, Pingbing Ming, Yi Sun, Richard Tsai, Xingye Yue and Pingwen Zhang. We are very grateful for their effort and their work that made this review possible. We are also grateful to Wing Kam Liu for suggesting Table 2, to Shi Jin for providing a more complete list of references on kinetic schemes, and to Randy LeVeque for providing detailed criticism on a preliminary draft. In addition, we would to thank the office of ONR for supporting a large part of the work discussed here. The of work E is supported in part by ONR grant N00014-01-1-0674 and National Natural Science Foundation of China through a Class B Award for Distinguished Young Scholars 10128102. The work of Engquist is supported in part by NSF grant DMS99-73341. The work of Xiantao Li is supported in part by ONR grant N00014-01-1-0674 and DOE grant DE-FG02-03ER25587. The work of Vanden-Eijnden is supported in part by NSF grants DMS02-09959 and DMS02-39625.

References

[1] A. Abdulle, Fourth order Chebychev methods with recurrence relations, SIAM J. Sci. Comput., 23(6) (2002), 2041-2054.
[2] A. Abdulle, On a-priori error analysis of fully discrete heterogeneous multiscale FEM, preprint, Department Mathematik, Universität Basel, 2004-08, 2004.
[3] A. Abdulle and W. E, Finite difference heterogeneous multi-scale method for homogenization problems, J. Comput. Phys., 191 (2003), 18-39.
[4] A. Abdulle and C. Schwab, Heterogeneous multiscale FEM for diffusion problem on rough surface, SIAM Multiscale Model. Simul., 3 (2005), 195-220.
[5] F. F. Abraham, J. Q. Broughton, N. Bernstein and E. Kaxiras, Concurrent coupling of length scales: Methodology and application, Phys. Rev. B, 60(4) (1999), 2391-2402.
[6] F. F. Abraham, J. Q. Broughton, N. Bernstein and E. Kaxiras, Spanning the continuum to quantum length scales in a dynamic simulation of brittle fracture, Europhys. Lett., 44(6) (1998), 783-787.
[7] D. Adalsteinsson and J. A. Sethian, The fast construction of extension velocities in level set methods, J. Comput. Phys., 148 (1999), 2-22.
[8] D. Adalsteinsson and J. A. Sethian, A fast level set method for propagating interfaces, J. Comput. Phys., 118(2) (1995), 269-277.
[9] M. Ainsworth and J. T. Oden, A Posteriori Error Estimation in Finite Element Analysis, Wiley-Interscience, New York, 2000.
[10] M. P. Allen and D. J. Tildesley, Computer Simulation of Liquids, Oxford University Press, New York, 1987.
[11] V. I. Arnold, Mathematical Methods in Classical Mechanics, 2nd ed., Graduate Texts in Mathematics, vol. 60, Springer-Verlag, 1989.
[12] I. Babuška, Solution of interface by homogenization, I, II, III, SIAM J. Math. Anal., 7 (1976), 603-645; 8 (1977), 923-937.
[13] I. Babuška, Homogenization and its applications, mathematical and computational problems, in: B. Hubbard (Ed.), Numerical Solutions of Partial Differential Equations-III, (SYNSPADE 1975, Maryland, May 1975), Academic Press, New York, 1976, pp. 89-116.
[14] I. Babuška, G. Caloz and J. Osborn, Special finite element methods for a class of second order elliptic problems with rough coefficients, SIAM J. Numer. Anal., 31 (1994), 945-981.
[15] I. Babuška, U. Banerjee and J. Osborn, Survey of meshless and generalized finite element methods, Acta Numerica, 12 (2003), 1-125.
[16] I. Babuška, U. Banerjee and J. Osborn, Generalized finite element methods – main ideas, results and perspective, Int. J. Comput. Meth., 1 (2004), 67-103.
[17] C. S. Becquart, P. C. Clapp and J. A. Rifkin, Molecular-dynamics simulations of tweed structure and the ω phase in Ni-Al, Phys. Rev. B, 48 (1993), 6-13.
[18] A. Bensoussan, J. L. Lions and G. C. Papanicolaou, Asymptotic Analysis for Periodic Structures, North-Holland Pub. Co., Amsterdam, 1978.
[19] R. B. Bird, C. F. Curtiss, R. C. Armstrong and O. Hassager, Dynamics of Polymeric Liquids, Vol. 2: Kinetic Theory, John Wiley, New York, 1987.
[20] D. L. Boley, Krylov space methods on state-space control models, Circ. Syst. Signal Proc., 13(6) (1994), 733-758.
[21] J. F. Bourgat, Numerical experiments of the homogenization method for operators with periodic coefficients, in: Lecture Notes in Math., vol. 707, Springer-Verlag, 1977, pp. 330-356.
[22] J. F. Bourgat, P. Le Tallec, B. Perthame and Y. Qiu, Coupling Boltzmann and Euler equa-

tions without overlapping, in: Domain Decomposition Methods in Science and Engineering (Como 1992), American Mathematics Society, 1994, pp. 377-398.
[23] J. F. Bourgat, P. Le Tallec and M. Tidriri, Coupling Boltzmann and Navier-Stokes equations by friction, J. Comput. Phys., 127(2) (1996), 227-245.
[24] J. H. Bramble, J. E. Pasciak and A. H. Schatz, The construction of preconditioners for elliptic problems by substructuring methods, Math. Comput., 47 (1986), 103-134.
[25] A. Brandt, Multiscale scientific computation: Review 2001, in: T. J. Barth, et.al (Eds.), Multiscale and Multiresolution Methods: Theory and Applications, Yosemite Educational Symposium Conf. Proc., 2000, Lecture Notes in Comp. Sci. and Engrg., vol. 20, Springer-Verlag, 2002, pp. 3-96.
[26] A. Brandt, Multigrid methods in lattice field computations, Nucl. Phys. B (Proc. Suppl.), 26B (1992), 137-180.
[27] A. Brandt, Multi-level adaptive solutions to boundary value problems, Math. Comput., 31(138) (1977), 333-390.
[28] A. Brandt, Multiscale research in molecular dynamics, Gauss Center Report WI/GC-3, 1995.
[29] W. Cai, M. de Koning, V. V. Bulatov and S. Yip, Minimizing boundary reflections in coupled-domain simulations, Phys. Rev. Lett., 85(15) (2000), 3213-3216.
[30] R. Car and M. Parrinello, Unified approach for molecular dynamics and density-functional theory, Phys. Rev. Lett., 55(22) (1985), 2471-2474.
[31] S. Chakravorty, C. M. Wayman, Thermoelastic martensitic transformation in beta' Ni-Al alloys, Metall. Mater. Trans. A, 7(4) (1976), 555-582.
[32] S. Chen and G. D. Doolen, Lattice Boltzmann methods for fluid flows, Ann. Rev. Fluid Mech., 30 (1998), 329-364.
[33] S. Chen, The heterogeneous multi-scale method based on the discontinuous Galerkin and finite volume schemes, thesis, Brown University, 2005.
[34] S. Chen, W. E and C. W. Shu, The heterogeneous multi-scale method based on discontinuous Galerkin method for hyperbolic and parabolic problems, SIAM Multiscale Model. Simul., 3 (2005), 871-894.
[35] L. T. Cheng and W. E, The heterogeneous multiscale method for interface dynamics, in: S. Y. Cheng, C.-W. Shu and T. Tang (Eds), Recent Advances in Scientific Computing and Partial Differential Equations, Contemporary Mathematics, Vol. 330, AMS, 2003, pp. 43-53.
[36] N. Choly, G. Lu, W. E and E. Kaxiras, Multiscale simulations in simple metals: A density-functional based methodology, Phys. Rev. B, 71 (2005), 094101.
[37] A. J. Chorin, Conditional expectations and renormalization, SIAM J. Multiscale Model. Simul., 1 (2003), 105-118.
[38] A. J. Chorin, Vorticity and Turbulence, Applied Mathematical Sciences, vol. 103, Springer-Verlag, 1998.
[39] A. J. Chorin, Computational Fluid Mechanics: Selected Papers, Academic Press, New York, 1989.
[40] A. J. Chorin, Numerical solution of the Navier-Stokes equations, Math. Comput., 22 (1968), 745-762.
[41] A. J. Chorin, O. Hald and R. Kupferman, Optimal prediction with memory, Physica D, 166(3-4) (2002), 239-257.
[42] A. J. Chorin, A. P. Kast and R. Kupferman, Optimal prediction of underresolved dynamics, Proc. Natl. Acad. Sci. USA, 95(8) (1998), 4094-4098.
[43] J. Cormier, J. M. Rickman and T. J. Delph, Stress calculation in atomistic simulations of perfect and imperfect solids, J. Appl. Phys., 89 (2001), 99-104.

[44] J. Z. Cui and L. Q. Cao, The two-scale analysis method for woven composite materials, in: Z. H. Zhong (Ed.), Engineering Computation and Computer Simulation I, Hunan University Press, 1995, pp. 203-212.
[45] S. Curtarolo and G. Ceder, Dynamics of an inhomogeneously coarse grained multiscale system, Phys. Rev. Lett., 88 (2002), 255504.
[46] W. A. Curtin and R. E. Miller, Atomistic/continuum coupling in computational material science, Model. Simul. Mater. Sci. Engrg., 11 (2003), R33-R68.
[47] I. Daubechies, Ten Lectures on Wavelets, CBMS-NSF Regional Conference Series in Applied Mathematics, SIAM Publications, 1992.
[48] C. Denniston and M. O. Robbins, Molecular and continuum boundary conditions for a miscible binary fluid, Phys. Rev. Lett., 87(17) (2001), 178302.
[49] S. M. Deshpande, Kinetic Flux Splitting Schemes, Computational Fluid Dynamics Review, John Wiley & Sons, Chichester, 1995.
[50] M. Doi and S. F. Edwards, The Theory of Polymer Dynamics, Oxford Science Publications, 1986.
[51] L. J. Durlofsky, Numerical calculation of equivalent grid block permeability tensors for heterogeneous poros-media, Water. Resour. Res., 27 (1991), 699-708.
[52] E. B. Dussan, On the spreading of liquids on solid surfaces: Static and dynamic contact lines, Annu. Rev. Fluid Mech., 11 (1979), 371-400.
[53] W. E, Analysis of the heterogeneous multiscale method for ordinary differential equations, Commun. Math. Sci., 1(3) (2003), 423-436.
[54] W. E, Homogenization of linear and nonlinear transport equations, Commun. Pur. Appl. Math., 45 (1992), 301-326.
[55] W. E and B. Engquist, The heterogeneous multi-scale method for homogenization problems, preprint.
[56] W. E and B. Engquist, The heterogeneous multi-scale methods, Commun. Math. Sci., 1 (2003), 87-133.
[57] W. E and B. Engquist, Multiscale modeling and computation, Notices of the AMS, 50(9) (2003), 1062-1070.
[58] W. E, B. Engquist and Z. Huang, Heterogeneous multiscale method: a general methodology for multiscale modeling, Phys. Rev. B, 67(9) (2003), 092101.
[59] W. E and Z. Huang, Matching conditions in atomistic-continuum modeling of materials, Phys. Rev. Lett., 87(13) (2001), 135501.
[60] W. E and Z. Huang, A dynamic atomistic-continuum method for the simulation of crystalline materials, J. Comput. Phys., 182 (2002), 234-261.
[61] W. E and X. Li, Analysis of the heterogeneous multiscale method for gas dynamics, Method. Appl. Anal., 11(4) (2004), 557-572.
[62] W. E, X. Li and E. Vanden-Eijnden, Some recent progress in multiscale modeling, in: S. Attinger and P. Koumoutsakos (Eds.), Multiscale Modeling and Simulation, Lecture Notes in Computational Science and Engineering, vol. 39, Springer-Verlag, 2004, pp. 3-22.
[63] W. E, D. Liu and E. Vanden-Eijnden, Analysis of multiscale methods for stochastic differential equations, Commun. Pur. Appl. Math., 58(11) (2005), 1544-1585.
[64] W. E and P. B. Ming, Analysis of multiscale methods, J. Comp. Math., 22 (2004), 210-219.
[65] W. E, P. B. Ming and P. W. Zhang, Analysis of the heterogeneous multiscale method for elliptic homogenization problems, J. Am. Math. Soc., 18(1) (2005), 121-156.
[66] W. E and X. Y. Yue, Heterogeneous multiscale method for locally self-similar problems, Commun. Math. Sci., 2 (2004), 137-144.

[67] B. Engquist, Computation of oscillatory solutions to hyperbolic differential equations, in: Lecture Notes in Math., vol. 1270, Springer-Verlag, 1987, pp. 10-22.
[68] B. Engquist and O. Runborg, Wavelet-based numerical homogenization with applications, in: T. J. Barth, et.al (Eds.), Multiscale and Multiresolution Methods: Theory and Applications, Yosemite Educational Symposium Conf. Proc., 2000, Lecture Notes in Comp. Sci. and Engrg., vol. 20, Springer-Verlag, 2002, pp. 97-148.
[69] B. Engquist and Y. H. Tsai, Heterogeneous multiscale methods for stiff ordinary differential equations, Math. Comput., 74 (2005), 1707-1742.
[70] F. Ercolessi and J. B. Adams, Interatomic potentials from first-principles calculations: The force-matching method, Europhys. Lett., 26 (1993), 583.
[71] K. Ericksson, C. Johnson and A. Logg, Explicit time-stepping for stiff ODEs, SIAM J. Sci. Comput., 25(4) (2003), 1142-1157.
[72] I. Fatkullin and E. Vanden-Eijnden, A computational strategy for multiscale systems with applications to Lorenz 96 model, J. Comput. Phys., 200(2) (2004), 605-638.
[73] E. G. Flekkøy, G. Wagner and J. Feder, Hybrid model for combined particle and continuum dynamics, Europhys. Lett., 52(3) (2000), 271-276.
[74] M. I. Freidlin and A. D. Wentzell, Random Perturbations of Dynamical Systems, 2nd ed., Springer-Verlag, 1998.
[75] D. Frenkel and B. Smit, Understanding Molecular Simulation: From Algorithms to Applications, 2nd ed., Academic Press, 2001.
[76] A. L. Garcia, J. B. Bell, W. Y. Crutchfield and B. J. Alder, Adaptive mesh and algorithm refinement using direct simulation Monte Carlo, J. Comput. Phys., 154 (1999), 134-155.
[77] C. W. Gear and I. G. Kevrekidis, Projective methods for stiff differential equations: Problems with gaps in their eigenvalue spectrum, SIAM J. Sci. Comput., 24(4) (2003), 1091-1106.
[78] C. W. Gear, J. Li and I. G. Kevrekidis, The gap-tooth scheme for particle simulations, Phys. Lett. A, 316 (2003), 190-195.
[79] J. Glimm, O. McBryan, R. Menikoff and D. H. Sharp, Front tracking applied to Rayleigh-Taylor instability, SIAM J. Sci. Stat. Comput., 7 (1986), 230-251.
[80] E. Godlewski and P. A. Raviart, Numerical Approximation of Hyperbolic Systems of Conservation Laws, Springer-Verlag, New York, 1996.
[81] G. H. Golub and C. F. Van Loan, Matrix Computations, The Johns Hopkins University Press, Baltimore, Maryland, 1983.
[82] L. Greengard and V. Rokhlin, A fast algorithm for particle simulations, J. Comput. Phys., 73 (1987), 325-348.
[83] W. Guo, T. P. Schulze and W. E, Simulation of impurity diffusion in a strained nanowire using off-lattice KMC, Commun. Comput. Phys., 2 (2007), 164-176.
[84] N. G. Hadjiconstantinou, Hybrid atomistic-continuum formulations and the moving contact-line problem, J. Comput. Phys., 154(2) (1999), 245-265.
[85] N. G. Hadjiconstantinou and A. T. Patera, Heterogeneous atomistic-continuum representation for dense fluid systems, Int. J. Mod. Phys. C, 8(4) (1997), 967-976.
[86] E. Hairer and G. Wanner, Solving Ordinary Differential Equations II, Stiff and Differential-Algebraic Problems, Springer-Verlag, 1991.
[87] J. Helmsen, E. Puckett, P. Colella and M. Dorr, Two new methods for simulating photolithography development in 3D, in: SPIE 1996 Symposium Proc., Intl. Symposium on Microlithography, Santa Clara, CA, vol. 2726, 1996, pp. 253-261.
[88] T. Y. Hou and X. H. Wu, A multiscale finite element method for elliptic problems in composite materials and porous media, J. Comput. Phys., 134 (1997), 169-189.

[89] B. D. Hughes, Random Walks and Random Environments, Vol. 2, Random Environments, Oxford University Press, 1996.
[90] J. H. Irving and J. G. Kirkwood, The statistical mechanical theory of transport processes IV, J. Chem. Phys., 18 (1950), 817-829.
[91] H. Kadowaki and W. K. Liu, Bridging multiscale method for localization problems, Comput. Method. Appl. Mech. Engrg., 193 (2004), 3267-3302.
[92] E. G. Karpov, G. J. Wagner and W. K. Liu, A Green's function approach to deriving non-reflecting boundary conditions in molecular dynamics simulations, Int. J. Numer. Meth. Engrg., 62(9) (2005), 1250-1262.
[93] E. G. Karpov, H. Yu, H. S. Park, W. K. Liu and J. Wang, Multiscale boundary conditions in crystalline solids: Theory and application to nanoindentation, Phys. Rev. B, submitted.
[94] M. Katsoulakis, A. J. Majda and D. G. Vlachos, Coarse-grained stochastic processes for lattice systems, Proc. Natl. Acad. Sci. USA, 100 (2003), 782-787.
[95] I. G. Kevrekidis, C. W. Gear, J. M. Hyman, P. G. Kevrekidis, O. Runborg and C. Theodoropoulos, Equation-free, coarse-grained multiscale computation: Enabling microscopic simulators to perform system-level analysis, Commun. Math. Sci., 1(4) (2003), 715-762.
[96] P. E. Kloeden and E. Platen, Numerical Solutions of Stochastic Differential Equations, Applications of Mathematics, vol. 23, Springer-Verlag, 1992.
[97] J. Koplik and J. R. Banavar, Continuum deductions from molecular hydrodynamics, Annu. Rev. Fluid Mech., 27 (1995), 257-292.
[98] T. G. Kurtz, A limit theorem for perturbed operator semigroups with applications to random evolutions, J. Funct. Anal., 12 (1973), 55-67.
[99] L. Landau and E. M. Lifshitz, Statistical Physics, Part 1, 3rd ed., Pergamon Press, 1980.
[100] L. Landau and E. M. Lifshitz, Theory of Elasticity, Pergamon Press, 1980.
[101] V. I. Lebedev, Explicit difference schemes for solving stiff problems with a complex or separable spectrum, Zh. Vychisl. Mat. Mat. Fiz., 40(12) (2000), 1801-1812 (in Russian); Comput. Math. Math. Phys., 40(12) (2000), 1729-1740 (English Translation).
[102] V. I. Lebedev and S. I. Finogenov, Explicit methods of second order for the solution of stiff systems of ordinary differential equations, Zh. Vychisl. Mat. Mat. Fiz., 16(4) (1976), 895-910.
[103] A. W. Lees and S. F. Edwards, The computer study of transport processes under extreme conditions, J. Phys. C, 5(15) (1972), 1921-1929.
[104] P. Le Tallec and J. P. Perlat, Coupling kinetic models with Navier-Stokes equations, CFD Review, 2 (1998), 833-855.
[105] R. LeVeque, Numerical Methods for Conservation Laws, Birkhauser, 1990.
[106] J. Li, D. Liao and S. Yip, Nearly exact solution for coupled continuum/MD fluid simulation, J. Comput. Aid. Mater. Des., 6(2-3) (1999), 95-102.
[107] T. Li, E. Vanden-Eijnden, P. Zhang and W. E, Stochastic models of polymeric fluids at small Deborah number, J. Non-Newton. Fluid Mech., 121(2-3) (2004), 117-125.
[108] X. Li and W. E, Multiscale modeling of the dynamics of solids at finite temperature, J. Mech. Phys. Solids, 53 (2005), 1650-1685.
[109] X. Li and W. E, Variational boundary conditions for molecular dynamics simulation of solids at low temperature, Commun. Comput. Phys., 1(1) (2006), 135-175.
[110] X. Li and W. E, Variational boundary conditions for molecular dynamics simulation of solids at finite temperature, preprint.
[111] P. L. Lions, G. Papanicolaou and S. R. S. Varadhan, Homogenization of Hamilton-Jacobi equations, unpublished.
[112] W. K. Liu, Y. F. Zhang and M. R. Ramirez, Multiple scale finite element methods, Int. J.

Numer. Meth. Engrg., 32 (1991), 969-990.
[113] W. K. Liu, E. G. Karpov, S. Zhang and H. S. Park, An introduction to computational nano mechanics and materials, Comput. Method. Appl. Mech. Engrg., 193 (2004), 1529-1578.
[114] G. Lu and E. Kaxiras, An overview of multiscale simulation of materials, preprint, 2003.
[115] A. J. Majda, I. Timofeyev and E. Vanden-Eijnden, A mathematical framework for stochastic climate models, Commun. Pur. Appl. Math., 54(8) (2001), 891-974.
[116] R. Miller and E. B. Tadmor, The quasicontinuum method: Overview, applications and current directions, preprint, 2004.
[117] R. Miller, E. B. Tadmor, R. Phillips and M. Ortiz, Quasicontinuum simulation of fracture at the atomic scale, Model. Simul. Mater. Sci. Engrg., 6(5) (1998), 607-638.
[118] G. W. Milton, The Theory of Composites, Cambridge University Press, 2002.
[119] P. B. Ming and X. Y. Yue, Numerical methods for multiscale elliptic problems, preprint, 2003.
[120] P. B. Ming and P. W. Zhang, Analysis of the heterogeneous multiscale method for parabolic homogenization problems, Math. Comput., submitted.
[121] F. Murat and L. Tartar, H-Convergence, Cours Peccot, 1977. Reprinted in: A. Cherkaev and R. Kohn (Eds.), Topics in the Mathematical Modeling of Composite Materials, Birkhauser, Boston, 1997, pp. 21-43.
[122] H. Nessyahu and E. Tadmor, Nonoscillatory central differencing for hyperbolic conservation laws, J. Comput. Phys., 87 (1990), 408-463.
[123] X. Nie, S. Chen, W. E and M. O. Robbins, A continuum and molecular dynamics hybrid method for micro- and nano-fluid flow, J. Fluid Mech., 500 (2004), 55-64.
[124] X. Nie, S. Chen, W. E and M. O. Robbins, Hybrid continuum-atomistic simulation of singular corner flow, Phys. Fluids, 16 (2004), 3579.
[125] S. T. O'Connell and P. A. Thompson, Molecular dynamics-continuum hybrid computations: A tool for studying complex fluid flows, Phys. Rev. E, 52(6) (1995), R5792-R5795.
[126] J. T. Oden and K. S. Vemaganti, Estimation of local modeling error and goal-oriented adaptive modeling of heterogeneous materials. I. Error estimates and adaptive algorithms, J. Comput. Phys., 164 (2000), 22-47.
[127] S. Osher and J. A. Sethian, Fronts propagating with curvature-dependent speed: Algorithms based on Hamilton-Jacobi formulations, J. Comput. Phys., 79 (1988), 12-49.
[128] G. C. Papanicolaou, Introduction to the asymptotic analysis of stochastic equations, in: R. C. Diprima (Ed.), Modern Modeling of Continuum Phenomena (Ninth Summer Sem. Appl. Math., Troy, N.Y., 1975), Lectures in Appl. Math., Amer. Math. Soc., vol. 16, 1977, pp. 109-147.
[129] G. C. Papanicolaou and S. R. S. Varadhan, Boundary value problems with rapidly oscillating random coefficients, in: J. Fritz, et. al (Eds.), Random Fields, North-Holland, Amsterdam, vol. 27, 1981, pp. 835-873.
[130] H. S. Park, E. G. Karpov, W. K. Liu and P. A. Klein, The bridging scale for two-dimensional atomistic/continuum coupling, Philos. Mag., 85(1) (2005), 79-113.
[131] R. G. Parr and W. Yang, Density Functional Theory of Atoms and Molecules, Oxford University Press, 1989.
[132] B. Perthame, Boltzmann-type schemes for gas dynamics and entropy property, SIAM J. Numer. Anal., 27 (1991), 1405-1421.
[133] B. Perthame, Second order Boltzmann-type schemes for compressible Euler equations in one and two space dimensions, SIAM J. Numer. Anal., 29 (1992), 1-19.
[134] C. S. Peskin, Numerical analysis of blood flow in the heart, J. Comput. Phys., 25(3) (1977), 220-252.

[135] C. S. Peskin and D. M. McQueen, Computational biofluid dynamics, Contemp. Math., 141 (1993), 161-186.
[136] R. Phillips, Crystals, Defects and Microstructures, Cambridge University Press, 2001.
[137] N. V. Priezjev and S. M. Troian, Molecular origin and dynamic behavior of slip in sheared polymer films, Phys. Rev. Lett., 92 (2004), 018302.
[138] D. I. Pullin, Direct simulation methods for compressible inviscid ideal gas flow, J. Comput. Phys., 34 (1980), 231-244.
[139] D. Qian, G. J. Wagner and W. K. Liu, A multiscale projection method for the analysis of carbon nanotubes, Comput. Method. Appl. Mech. Engrg., 193 (2004), 1603-1632.
[140] T. Z. Qian and X. P. Wang, Sinusoidal fluid-solid interactions: from molecular simulations to hydrodynamic modeling, preprint.
[141] T. Z. Qian, X. P. Wang and P. Sheng, Molecular scale contact line hydrodynamics of immiscible flows, Phys. Rev. E, 68 (2003), 016306.
[142] T. Qian, X. P. Wang and P. Sheng, Molecular hydrodynamics of the moving contact line in two-phase immiscible flows, Commun. Comput. Phys., 1 (2006), 1-52.
[143] A. Quarteroni and A. Valli, Domain Decomposition Methods for Partial Differential Equations, Oxford Science Publications, 1999.
[144] W. Ren, Multiscale modeling of polymeric fluids, in preparation.
[145] W. Ren, Accessment of the errors in multiscale methods for complex fluids, in preparation.
[146] W. Ren and W. E, Heterogeneous multiscale method for the modeling of complex fluids and microfluidics, J. Comput. Phys., 204(1) (2005), 1-26.
[147] W. Ren, X. Zhou and W. E, Constant rate of strain molecular dynamics, in preparation.
[148] M. O. Robbins and M. H. Müser, Computer simulations of friction, lubrication and wear, in: B. Bhushan (Ed.), Modern Tribology Handbook, CRC Press, 2001.
[149] R. E. Rudd and J. Q. Broughton, Atomistic simulation of MEMS resonators through the coupling of length scales, J. Model. Simul. Microsyst., 1 (1999), 29-38.
[150] R. E. Rudd and J. Q. Broughton, Coarse-grained molecular dynamics and the atomic limit of finite elements, Phys. Rev. B, 58(10) (1998), R5893–R5896.
[151] O. Runborg, C. Theodoropoulos and I. G. Kevrekidis, Effective bifurcation analysis: Time-stepper based approach, Nonlinearity, 15(2) (2002), 491-511.
[152] M. Sahimi, Flow and Transport in Porous Media and Fractured Rock, John Wiley, 1995.
[153] R. H. Sanders and K. H. Prendergast, On the origin of the 3-kiloparsec arm, Astrophys. J., 188 (1974), 489-500.
[154] S. Succi, O. Filippova, G. Mith and E. Kaxiras, Applying the lattice Boltzmann equation to multiscale fluid problems, Comput. Sci. Engrg., 3 (2001), 26.
[155] H. Schmidt and R. Klein, A generalized level-set/in-cell-reconstruction approach for accelerating turbulent premixed flames, Combust. Theor. Model., 7 (2003), 243-267.
[156] T. Schulze, P. Smereka and W. E, Coupling kinetic Monte-Carlo and continuum models with application to epitaxial growth, J. Comput. Phys., 189 (2003), 197-211.
[157] C. Schwab and A. M. Matache, Generalized FEM for homogenization problems, in: T. J. Barth, et.al (Eds.), Multiscale and Multiresolution Methods: Theory and Applications, Yosemite Educational Symposium Conf. Proc., 2000, Lecture Notes in Comp. Sci. and Engrg., vol. 20, Springer-Verlag, 2002, pp. 197-237.
[158] C. Schwab and A. M. Matache, Two-scale FEM for homogenization problems, in: I. Babuška, et. al (Eds.), Mathematical Modelling and Numerical Simulation in Continuum Mechanics Conf. Proc., Yamaguchi, Japan, 2000, Lecture Notes in Comp. Sci. and Engrg., Springer-Verlag, 2002.

[159] J. A. Sethian, Fast marching level set methods for three dimensional photolithography development, in: SPIE 1996 Symposium Proc., Intl. Symposium on Microlithography, Santa Clara, CA, vol. 2726, 1996, pp. 261-272.
[160] R. Sharp. Y. H. Tsai and B. Engquist, Multiple time scale methods for the inverted pendulum problem, in: Proceedings of Conference on Multiscale Methods in Science and Engineering, Lecture Notes in Computational Science and Engineering, Springer Verlag, vol. 44, 2005, pp. 233-244.
[161] V. B. Shenoy, R. Miller, E. B. Tadmor, R. Phillips and M. Ortiz, Quasicontinuum models of interfacial structure and deformation, Phys. Rev. Lett., 80(4) (1998), 742-745.
[162] V. B. Shenoy, R. Miller, E. B. Tadmor, D. Rodney, R. Phillips and M. Ortiz, An adaptive finite element approach to atomic-scale mechanics – the quasicontinuum method, J. Mech. Phys. Solids, 47(3) (1999), 611-642.
[163] L. E. Shilkrot, W. A. Curtin and R. E. Miller, A coupled atomistic/continuum model of defects in solids, J. Mech. Phys. Solids, 50 (2002), 2085-2106.
[164] L. E. Shilkrot, R. E. Miller and W. A. Curtin, Multiscale plasticity modeling: coupled atomistics and discrete dislocation mechanics, J. Mech. Phys. Solids, 52 (2004), 755-787.
[165] G. S. Smith, E. B. Tadmor and E. Kaxiras, Multiscale simulation of loading and electrical resistance in silicon nanoindentation, Phys. Rev. Lett., 84(6) (2000), 1260-1263.
[166] H. Spohn, Large Scale Dynamics of Interacting Particles, Springer-Verlag, 1991.
[167] Y. Sun, thesis, Princeton University, 2006.
[168] Y. Sun and B. Engquist, Heterogeneous multiscale methods for interface tracking of combustion fronts, SIAM Multiscale Model. Simul., 5 (2006), 532-563.
[169] E. B. Tadmor, M. Ortiz and R. Phillips, Quasicontinuum analysis of defects in crystals, Philos. Mag., A73 (1996), 1529-1563.
[170] L. Tartar, Solutions oscillantes des équations de Carleman, Goulaouic-Meyer-Schwartz Seminar, 1980-1981, Exp. No. XII, 15 pp., cole Polytech., Palaiseau, 1981.
[171] P. A. Thompson and M. O. Robbins, Simulations of contact-line motion: slip and the dynamic contact angle, Phys. Rev. Lett., 63(7) (1989), 766-769.
[172] P. A. Thompson and S. M. Troian, A general boundary condition for liquid flow at solid surfaces, Nature, 389 (1997), 360-362.
[173] A. K. Tornberg and B. Engquist, Interface tracking in two-phase flows, in: Multifield Problems, State of the Art, Springer-Verlag, 2000, pp. 58-66.
[174] S. Torquato, Random Heterogeneous Materials: Microstructure and Macroscopic Properties, Springer-Verlag, 2002.
[175] E. Vanden-Eijnden, Numerical techniques for multiscale dynamical systems with stochastic effects, Commun. Math. Sci., 1(2) (2003), 385-391.
[176] A. F. Voter and S. P. Chen, Accurate interatomic potentials for Ni, Al and Ni3Al, Mater. Res. Soc. Proc., 82 (1987), 175-180.
[177] A. F. Voter, F. Montalenti and T. C. Germann, Extending the time scale in atomistic simulation of materials, Annu. Rev. Mater. Res., 32 (2002), 321-346.
[178] G. J. Wagner and W. K. Liu, Coupling of atomistic and continuum simulations using a bridging scale decomposition, J. Comput. Phys., 190 (2003), 249-274.
[179] A. Warshel and M. Levitt, Theoretical studies of enzymic reactions, J. Mol. Biol., 103 (1976), 227-249.
[180] T. Werder, J. H. Walther, J. Asikainen and P. Koumoutsakos, Continuum-particle hybrid methods for dense fluids, in: S. Attinger and P. Koumoutsakos (Eds.), Multiscale Modeling and Simulation, Lecture Notes in Computational Science and Engineering, Springer, vol. 39,

2004, pp. 35-68.
[181] S. P. Xiao and T. Belytschko, A bridging domain method for coupling continua with molecular dynamics, Comput. Method. Appl. Mech. Engrg., 193 (2004), 1645-1669.
[182] J. Xu, Two-grid discretization techniques for linear and nonlinear PDEs, SIAM J. Numer. Anal., 33(5) (1996), 1759-1777.
[183] K. Xu and K. H. Prendergast, Numerical Navier-Stokes solutions from gas kinetic theory, J. Comput. Phys., 114 (1994), 9-17.
[184] J. Z. Yang and X. Li, Comparative study of boundary conditions for molecular dynamics simulations of solids at low temperature, Phys. Rev. B, 73 (2006), 224111.
[185] H. T. Yau, Asymptotic solutions to dynamics of many-body systems and classical continuum equations, in: Current Development in Mathematics, International Press, 2000.
[186] X. Y. Yue, The heterogeneous multi-scale method for modeling functionally graded materials, in preparation.
[187] X. Y. Yue and W. E, Numerical methods for multiscale transport equations and application to two phase porous media flow, J. Comput. Phys., to appear.
[188] X. Y. Yue and W. E, The local microscale problem in the multiscale modelling of strongly heterogeneous media: Effect of boundary conditions and cell size, J. Comput. Phys., to appear.
[189] V. V. Yurinskii, Averaging of symmetric diffusion in random media, Sibirsk. Mat. Zh., 23(2) (1982), 176-188; Siberian Math. J., 27 (1986), 603-613 (English Translation).